NORTHWESTERN UNIVERSITY

From Regularity to Chaos: Studies on Semiconductor Microdisks and Deformed Microdisk Lasers

A DISSERTATION

SUBMITTED TO THE GRADUATE SCHOOL

IN PARTIAL FULFILLMENT OF THE

REQUIREMENTS

for the degree

DOCTOR OF PHILOSOPHY

Field of Physics and Astronomy

By

WEI FANG

EVANSTON, ILLINOIS

December 2006

ABSTRACT

Semiconductor microcavities are building blocks for integrated photonic systems. Microdisk cavities have based on whispering gallery modes have small mode volume and very high quality factor. Hence, the quantum effect is significant in such structures. We have studied the enhancement of spontaneous emission rates for InAs quantum dots embedded in GaAs microdisks in the time-resolved photoluminescence experiment. Using the non-negative least squares algorithm, we recover the distribution of spontaneous emission rates for an ensemble of QDs. The maximum enhancement factor of spontaneous emission rate exceeds 10.

Boundary roughness is inevitable during fabrication process. We have demonstrated the lasing action from a dynamically localized mode in a microdisk resonator with rough boundary. Although substantial boundary roughness and surface defects in our devices imply strong light scattering and destroy the regular whispering gallery modes, the destructive interference of the scattered light leads to the dynamical Anderson localization in the phase space of the system and the formation of a different type of high-Q modes.

We have presented numerical and experimental studies of the high-quality modes in two-dimensional semiconductor stadium microcavities. Although the classical ray mechanics is fully chaotic in a stadium billiard, all of the high-quality modes show strong "scar" around unstable periodic orbits. For a high-quality mode associated with multiple

unstable periodic orbits, its quality factor changes non-monotonically with the deformation, so that there exists an optimal deformation for each mode at which its quality factor reaches a local maximum. Experimentally we optimized the lasing threshold of a semiconductor microstadium by controlling its shape.

Finally, we demonstrate hybrid UV microdisk laser on a silicon substrate, and their applications for chemical sensing.

TABLE OF CONTENTS

LIST OF FIGURES

CHAPTER 1

INTRODUCTION

Semiconductor microcavities are essential components of integrated photonic circuits with their size on the order of wavelength. There are several types of microcavities. Vertical-cavity surface-emitting lasers (VCSEL) [1] have quasi 1-dimensional ($1D$) cavities. Light propagates in such cavity is confined by two distributed bragg reflectors. Photonic crystal cavities [2] are mode by 2-dimensional ($2D$) bragg scattering. Light is localized in the structure as a defect mode. Microdisks [3], however, have the highest cavity quality factor (Q) by utilizing total internal reflection (Fig. 1.1). Therefore microdisks have great advantage for many applications (e.g., low threshold lasers, fast response light sources), and have attracted continuate interests for more than one decay.

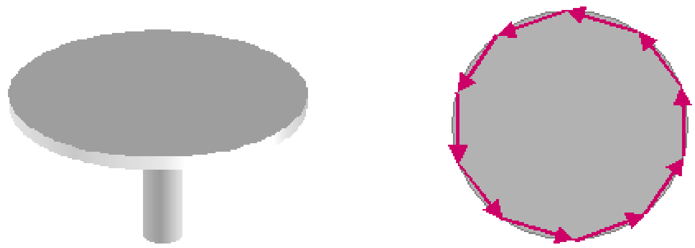

Figure 1.1: side view of a microdisk (left) and top view (right). The semiconductor disk has larger refractive index than surrounding media (air), so once the angle of incidence is larger than critical angle, a ray will always experience total internal reflection.

With circular shape, microdisk has the highest symmetry in two-dimensional ($2D$) system. The classical ray trajectories in the cavity show regular patterns. Due to the rotational symmetry of the structure, a ray trajectory has conserved angular momentum (respect to the origin of circle), and thus constant incident angles. In a dielectric microdisk with refractive index greater than one, once the light has incident angle greater than the critical angle where total internal reflection (TIR) happens, it will always be trapped in the disk classically. The energy can only escape from the cavity by tunneling. Therefor the corresponding optical modes have very high quality factor. With their sizes comparable with optical wavelength, microdisks show significant quantum effects. Semiconductor microdisk incorporate with quantum dots provides a great tool to study the cavity quantum electrodynamics in solid state.

On the other hand, when boundary deformation is introduced into a circular disk, the angular momentum conservation law no longer stands. The classical ray dynamics may even become chaotic with sufficient deformations. We mainly focus on two types of deformations, which drive the ray dynamics into fully chaotic in the systems. The first one is the uncontrolled deformation - surface roughness on the boundary, which is introduced during the fabrication process. Another type is smoothly deformed cavity, such as stadium cavity, which shows completely chaotic ray dynamics in the cavity. In these cavities, a ray having initial incident angle greater than critical angle will quickly escape from the cavity refractively due to it's chaotic behavior. It would be interesting to exam whether there exits high-Q modes in such cavities, and what's the mechanism to form such high-Q modes.

In the following part of this chapter, we give brief introductions of optical modes in microdisks, the properties of semiconductor quantum dots, some basic concepts and methods used in chaotic system, and finally the powerful numerical simulation method: finite-difference time-domain (FDTD) method.

1.1 Microdisk cavity

In this section, we give a brief description of the general wave function solutions of microdisk structure, namely the *whispering gallery* modes (WGMs).

Waveguide solutions The thickness of a typical microdisk usually is much smaller than the size of the disk. In this case, we can approximate the disk layer an infinite large layer (compare to the thickness). Consider a more general case, we have three infinitely large dielectric layer structure as shown in Fig. 1.2, with refractive index n

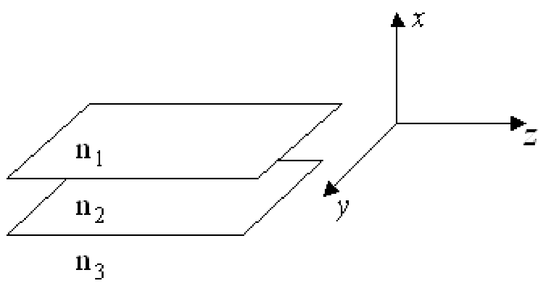

Figure 1.2: Waveguide structure of three dielectric layers.

$$n = \begin{cases} n_1 & x > h \\ n_2 & 0 < x < h \\ n_3 & x < 0 \end{cases} \tag{1.1}$$

and $n_2 > n_3 \geq n_1$. The solution of electromagnetic (EM) wave propagate in such structure can be solved by Maxwell equation (in dielectric media)

$$\begin{aligned} \boldsymbol{\nabla} \cdot \boldsymbol{D} = 0 \qquad \boldsymbol{\nabla} \times \boldsymbol{E} = -\frac{\partial \boldsymbol{B}}{\partial t} \\ \boldsymbol{\nabla} \cdot \boldsymbol{B} = 0 \qquad \boldsymbol{\nabla} \times \boldsymbol{H} = \frac{\partial \boldsymbol{D}}{\partial t} \end{aligned} \tag{1.2}$$

Assuming the solutions have harmonic time dependence $e^{-i\omega t}$ and propagate in $\{x, z\}$ plan, EM field can be expressed by separating variables

$$\begin{aligned} \boldsymbol{E}(x, z, t) = \boldsymbol{E}(x) \exp\left[i(\beta z - \omega t)\right] \\ \boldsymbol{H}(x, z, t) = \boldsymbol{H}(x) \exp\left[i(\beta z - \omega t)\right] \end{aligned} \tag{1.3}$$

where β is the wave vector along z direction.

With Eq. 1.3 and 1.2, we can separate Maxwell equations into two parts (noting that $\partial/\partial y = 0$

$$\begin{cases} \beta E_y = \omega\mu H_x \\ \frac{\partial E_y}{\partial x} = i\omega\mu H_z \\ i\beta H_x - \frac{\partial H_z}{\partial x} = -i\omega\epsilon E_y \end{cases} \tag{1.4}$$

$$\begin{cases} \beta H_y = -\omega\epsilon E_x \\ \frac{\partial H_y}{\partial x} = -i\omega\epsilon E_z \\ i\beta E_x - \frac{\partial E_z}{\partial x} = i\omega\mu H_y \end{cases} \tag{1.5}$$

where ϵ is the electric permitivity, and μ is the magnetic permeability. Eq. 1.4 has $\boldsymbol{E}$ field parallel to the interface of layers, and called *transverse electric* (TE) wave. While Eq. 1.5 has $\boldsymbol{H}$ field parallel to the interface, called *transverse magnetic* (TM) wave. By eliminating H_x and H_z (E_x and E_z) from Eq. 1.4 (1.5), we can get scalar Helmholtz equation:

$$\frac{\partial^2 E_y}{\partial x^2} + (k_0^2 n_j^2 - \beta^2)E_y = 0 \tag{1.6}$$

$$\frac{\partial^2 H_y}{\partial x^2} + (k_0^2 n_j^2 - \beta^2)H_y = 0 \tag{1.7}$$

where k_0 is the wave vector in vacuum, and $j = 1, 2, 3$.

When the condition $k_0 n_{1(3)} < \beta < k_0 n_2$ is satisfied, we can see the solutions have main energy confined in layer 2 with exponential decay into the top and bottom layer along x direction, due to total internal reflection. But not any β satisfying such condition will exist because of the boundary condition. So we are interested in these eigen modes in the waveguide, who has no energy leakage when propagates along the layer with high refractive index. Let take TE wave for instance.

Let's assume the eigen mode can be express in such form

$$E_y(x) = \begin{cases} A\ \exp\left[-q(x-h)\right] & x > h \\ B\ \cos(\kappa x) + C\ \sin(\kappa x) & 0 < x < h \\ D\ \exp(px) & x < 0 \end{cases} \tag{1.8}$$

By submitting Eq. 1.8 into Eq. 1.6, we get

$$\begin{cases} \kappa = \sqrt{k_0^2 n_2^2 - \beta^2} \\ q = \sqrt{\beta^2 - k_0^2 n_1^2} \\ p = \sqrt{\beta^2 - k_0^2 n_3^2} \end{cases} \tag{1.9}$$

Because of the continuity of $E_y(x)$ and $\partial E_y(x)/\partial x$ at $x = 0, h$, we can get

$$\begin{cases} A = B\ \cos(\kappa h) + C\ \sin(\kappa h) \\ D = B \\ -Aq = -B\kappa\ \sin(\kappa h) + C\kappa\ \cos(\kappa h) \\ Dp = C\kappa \end{cases} \tag{1.10}$$

Finally, with Eq. 1.10 and 1.9, we get the characteristic equation

$$\tan(\kappa h) = \frac{\kappa(p+q)}{\kappa^2 - pq} = \frac{\kappa\left[\sqrt{k_0^2(n_2^2 - n_1^2) - \kappa^2} + \sqrt{k_0^2(n_2^2 - n_3^2) - \kappa^2}\right]}{\kappa^2 - \sqrt{k_0^2(n_2^2 - n_1^2) - \kappa^2}\sqrt{k_0^2(n_2^2 - n_3^2) - \kappa^2}} \tag{1.11}$$

For symmetric structure, where $n_1 = n_3$, it can be simplified as:

$$\tan(\kappa h/2) = \frac{\sqrt{k_0^2(n_2^2 - n_1^2) - \kappa^2}}{\kappa} \tag{1.12}$$

Once the κ is get, we can calculate the eigen modes of waveguide by Eq. 1.3 and 1.8. We are not going to detail of the waveguide mode solutions. But it's worth to check the a couple of things. Assuming

$$\phi_{21} = \arctan(\frac{p}{\kappa}) \tag{1.13}$$

$$\phi_{23} = \arctan(\frac{q}{\kappa}) \tag{1.14}$$

then from Eq. 1.11 we can get

$$\kappa h = l\pi + \phi_{21} + \phi_{23} \qquad (l = 0, 1, 2 \cdots) \tag{1.15}$$

This is the phase quantization condition for waveguide mode. We can see here κ is the wave vector along x direction, l is the order of waveguide mode, and $\phi_{21(3)}$ is the phase change when wave experiences total internal reflection on the interfaces. The smaller h is, the less number of modes the waveguide can support. $\beta = \sqrt{k_0^2 n_2^2 - \kappa^2}$ is the wave vector component parallel to interface. We can introduce the parameter $n_{eff} \equiv k_0/\beta = \sqrt{n_2^2 - \kappa^2/k_0^2}$, which is only a function of h and l. For an arbitrary shape thin planner cavity, we have the scalar wave equation (TE polarization)

$$(\nabla^2_{x,y,z} + k_0^2 n_j^2)E = 0 \tag{1.16}$$

By separating variable $E(x, y, z) = \psi(y, z)X(x)$, where $X(x)$ satisfy the solutions of Eq. 1.8, in layer 2 we have

$$(\nabla^2_{x,y,z} + k_0^2 n_2^2)\psi X = (\nabla^2_{y,z} + k_0^2 n_2^2 - \kappa^2)\psi X = (\nabla^2_{y,z} + k_0^2 n_{eff}^2)\psi X = 0 \tag{1.17}$$

In this way, we simplify the $3D$ wave equation to a $2D$ Helmholtz equation:

$$(\nabla^2 + k_0^2 n_{eff}^2)\psi = 0 \tag{1.18}$$

for general thin planner cavity problem. Note that Schröndinger equation has the same form in $2D$ system.

Whispering gallery modes For circular disk, it's more convenient to solve the Helmholtz equation (Eq. 1.18) in cylindrical coordinates.

$$\frac{\partial^2 \psi}{\partial r^2} + \frac{1}{r}\frac{\partial \psi}{\partial r} + \frac{1}{r^2}\frac{\partial^2 \psi}{\partial \phi^2} + k_0^2 n_{eff}^2\, \psi = 0 \tag{1.19}$$

By separating variables $\psi(r,\phi) = R(r)\Phi(\phi)$, we can get

$$r^2\frac{d^2R}{dr^2} + r\frac{dR}{dr} + (k_0^2 n_{eff}^2 - u)R = 0 \tag{1.20}$$

$$\frac{d^2\Phi}{d\phi^2} - u\Phi = 0 \tag{1.21}$$

The exact solutions with dielectric boundary conditions are complicate [4]. For high-Q modes in microdisks with total internal reflection on the boundary, we can take approximation $\psi(r = R_0, \phi) = 0$, where R_0 is the radius of disk. With periodic boundary condition for ϕ, we get $\Phi(\phi) = e^{im\phi}$ with $u \equiv m^2, m = 0, \pm 1, \pm 2, \cdots$. So the solutions for Eq. 1.20 inside the cavity can be write as

$$\psi_{in}(r,\phi) = J_m(2\pi r n_{eff}/\lambda_{m,n})e^{im\phi} \tag{1.22}$$

where $J_m(r)$ is Bessel function of m order, and the resonant wavelength $\lambda_{m,n}$ can be quantized by $\chi_{m,n}$:

$$\lambda_{m,n} = 2\pi n_{eff} R_0/\chi_{m,n} \tag{1.23}$$

where $\chi_{m,n}$ is the nth zero of $J_m(r)$. Such eigen modes are called whispering gallery modes [5]. Figure 1.3 shows the intensity distribution of a $\mathrm{WGM}_{12,1}$.

The wave of WGM propagating outward from the disk into the surrounding low index region is evanescent, and the energy can only leak form the cavity to free space by

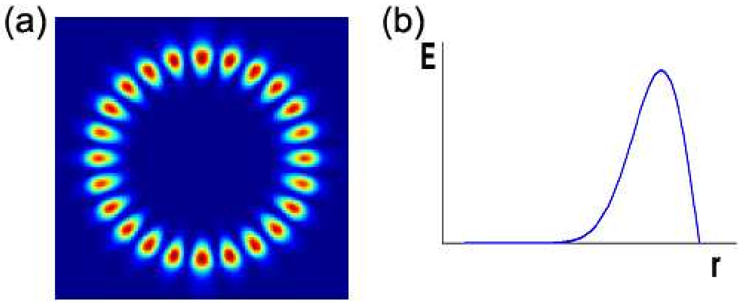

Figure 1.3: (a) Intensity distribution of a WGM with $m = 12, n = 1$. (b) E-field distribution along radius.

quantum tunneling. So usually WGM has very high-Q, which can be roughly estimated as $Q \approx \exp(2m\eta)$, where $\eta = \tanh\left[(1 - 1/n_{eff}^2)^{1/2}\right] - (1 - 1/n_{eff}^2)^{1/2}$ [3].

1.2 Quantum dots

Quantum dots (QDs) refer to nano-scale solid state structures, in which electrons are confined in all directions. Similar to electrons orbiting an atom with certain quantized energy levels, all the available states in a quantum dot exist only at discrete energies. Thus quantum dots can be regarded as artificial atoms [6]. Because most quantum dots have their lateral dimensions much larger than vertical extension, they can be treated as large $2D$ atoms. Figure 1.4 shows a shematic comparison of a real $3D$ atom and a dis-shaped quantum dot [7].

Compare to real atom, quantum dots have much larger size, and the quantization energy is of the same order of magnitude as the electron-electron Coulomb interaction. One would expect in quantum dots an interplay between quantization and Coulomb interaction-induced effects for multiple charges.

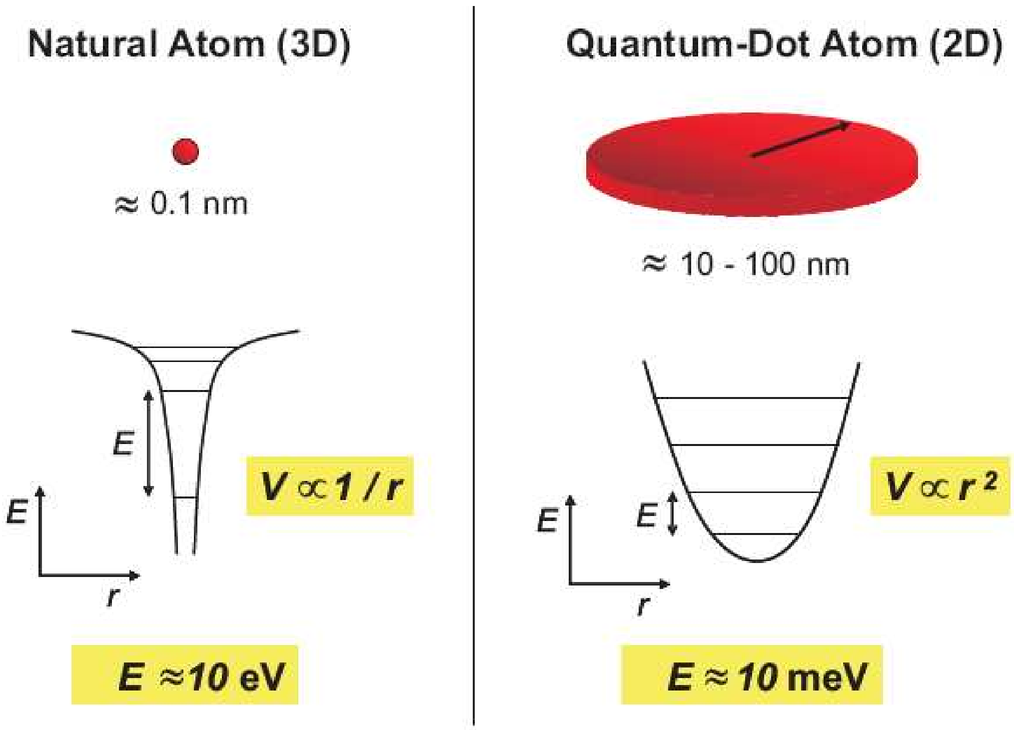

Figure 1.4: Schematic comparison of a real atom (left) and a quantum dot "atom" (right) represented by a dis-shaped quantum dot

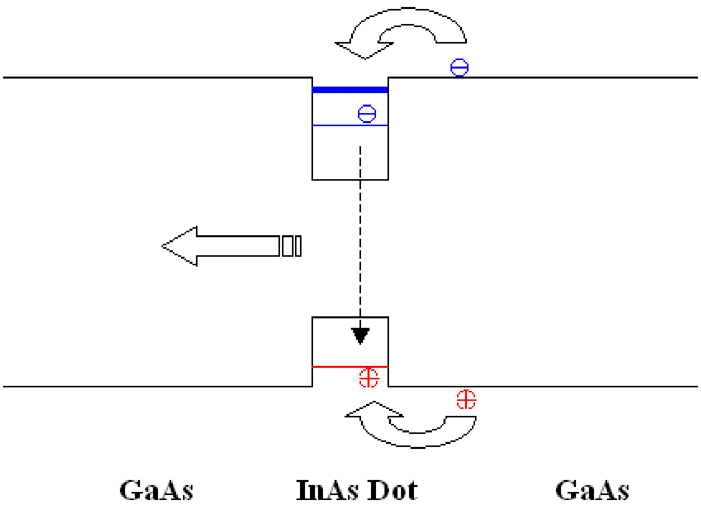

Figure 1.5: Schematic energy-band diagram

Semiconductor quantum dots can be formed by microstructuring of a quantum well in 2-dimensions [8]. A better controlled method is self-organized epitaxial growth due to lattice mismatch. Typical structure is InAs grown on a GaAs surface. Because of the lattice mismatch between these two materials, the minimization of strain energy leads to the formation of small InAs islands. Dimension of the quantum dots grown in this way is 2.8 nm in height and 24 nm for base dimension for 1.8 monolayer (ML) InAs deposit on GaAs substrate.

Figure 1.5 shows a schematic energy-band diagram of InAs quantum dots sample. InAs has smaller band gap compare to GaAs. Carrier generated in the GaAs layer will diffuse and be trapped by InAs quantum dots. The radiative transitions between electron and hole confined states show narrow peaks in the photoluminescence (PL) spectra due to their discrete energy levels. Despite of narrow emission spectrum linewidth of an individual quantum dot, the self-organized quantum dot sample usually shows a broad PL spectrum due to inhomogeneous broadening, which is result from the Gauss statistics of quantum dots size distribution.

1.3 Classical and quantum phase space representation

The phase space representation is a very useful tool to study the chaotic system. With proper mapping method, phase space representation usually shows more clear physical picture. In this section, we first give an brief description of phase space representation and several important concepts in $2D$ classical dynamical system, then followed by the corresponding quantum system representation.

Classical billiard

$2D$ billiard is a classical system of a point particle moving freely in the region of the plane bounded by a closed curve $\mathscr{B}$ (the "billiard") and being reflected elastically at impacts with $\mathscr{B}$, according to the law: "the angle of reflection equals the angle of incidence". Since the ray dynamics is basically a billiard problem, this simple system provides a good model to study the classical optics in $2D$ system.

Poincaré Surface of Section The phase space of a $2D$ Hamiltonian system has four canonically conjugate variables: $\{p_x, p_y; x, y\}$, where $p_{x(y)}$ is momentum and $x(y)$ is position coordinate. Since the energy is conserved in billiard problem, p_x and p_y are restrained by $p_x^2 + p_y^2 = const$, thus one of the dimension is reduced. Yet the phase space diagram still has $3D$ structure, which is difficult to visualize. Further investigation into the billiard system, one can find that the particle moves in straight lines between impacts with boundary $\mathscr{B}$, and an trajectory may be completely specified by giving the sequence of its positions and directions immediately after each impact. Thus, a $2D$ surface of section (SOS) can be chosen in the $3D$ phase space, by only taking into account the intersections of the orbit with the boundary [10]. Such technique is called Poincaré SOS method, namely a reduction of a N-dimensional continuous time system to an $(N-1)$-dimensional discrete time map.

For illustration, we choose a simple system of circular billiard, as shown in Fig.1.6. The two conjugate variables we used for the SOS map are $\{s, p\}$, where s denotes the arc length of the position the orbit impact with boundary, and p is the tangential momentum at position s. s usually is normalized to 1, and p can be expressed by the angle of incidence χ as: $p = sin(\chi)$ for a unit mass particle. As we can see in the figure, because of the rotational symmetry, the tangential momentum is conserved. So the blue spots representing the trajectory in phase space lay on a horizontal line.

An orbit in phase space consists of consequent number pairs (dots in $2D$ map) $\{s_n, p_n\}$, corresponding to the nth bounce. This discrete dynamics can be expressed as a *mapping* M symbolically:

$$\begin{pmatrix} s_{n+1} \\ p_{n+1} \end{pmatrix} = M \begin{pmatrix} s_n \\ p_n \end{pmatrix} \tag{1.24}$$

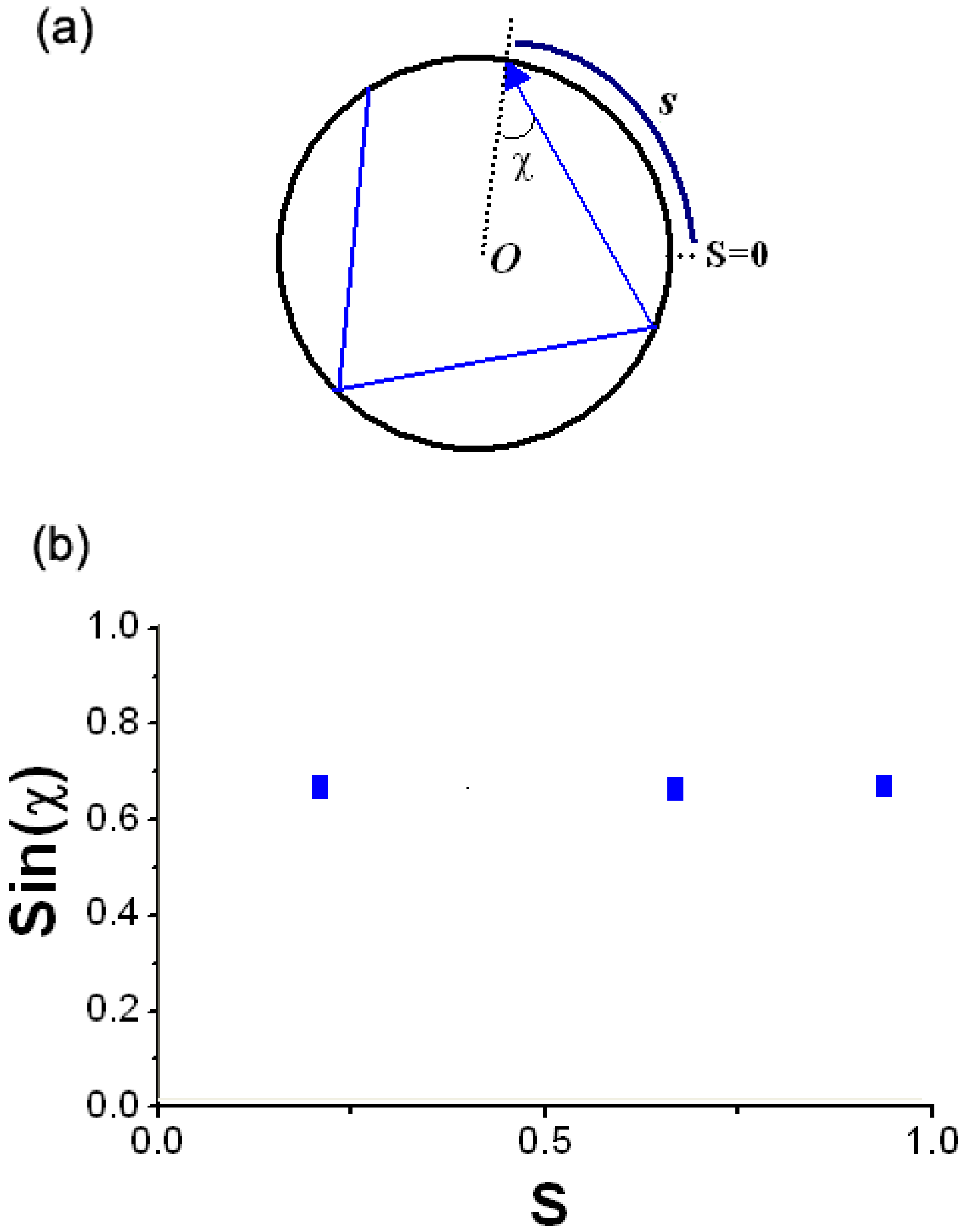

Figure 1.6: (a) Ray trajectory in circular billiard, and (b) corresponding SOS map.

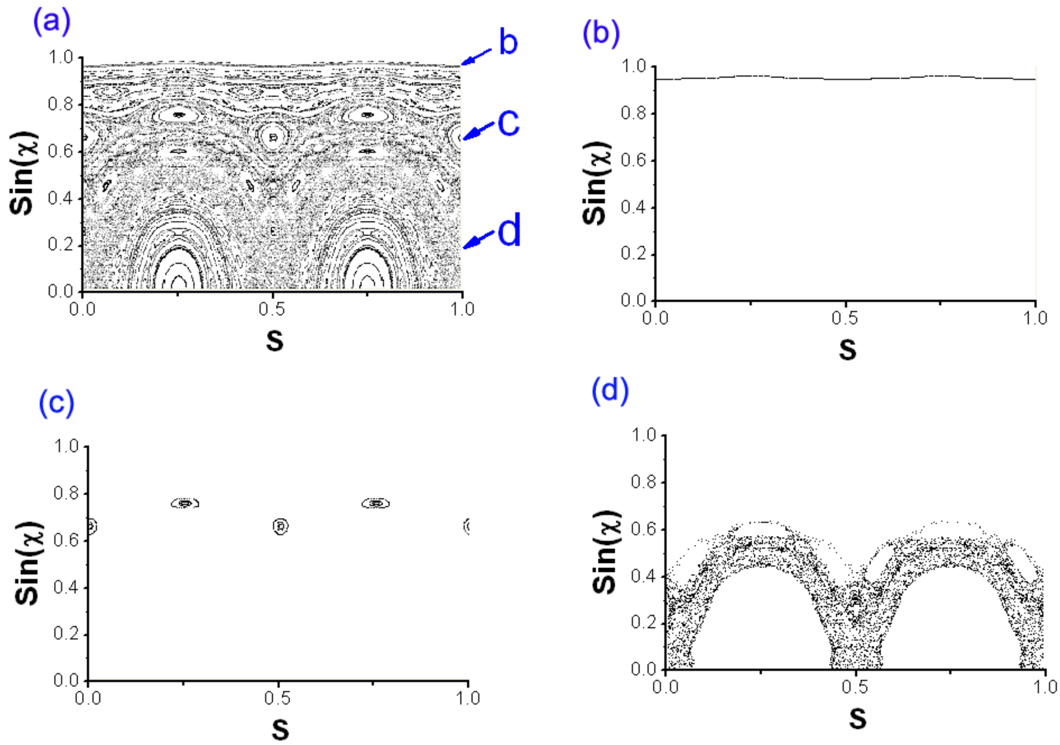

Figure 1.7: (a) Poincaré SOS map of quadruple billiard $r(\theta) = r_0[1 + \epsilon cos(2\theta)]$, $\epsilon = 0.07$. (b) Invariant curve. (c) Stable periodic orbit, with island structures in vicinity. (d) Chaotic orbit

Types of orbits There are three ways in which the orbit generated by infinitely iterations of M can be explored in phase space (as shown in Fig.1.7).

(i) Periodic orbit A finite set of N points $\{s_1, p_1\}$, $\{s_2, p_2\}$, ..., $\{s_N, p_N\}$ may be encountered repeatedly (Fig.1.7(c)). Symbolically such closed orbit satisfies

$$\begin{pmatrix} s_{n+N} \\ p_{n+N} \end{pmatrix} = M^N \begin{pmatrix} s_n \\ p_n \end{pmatrix} = \begin{pmatrix} s_n \\ p_n \end{pmatrix} \tag{1.25}$$

so that each of its N points is a *fixed point* of the mapping M^N.

(ii) Invariant curve The iterates of $\{s_1, p_1\}$ may fill a smooth curve, which maps onto itself under M, although its individual points do not map onto themselves (Fig.1.7(b)).

(iii) Chaotic orbit The iterates of $\{s_1, p_1\}$ may fill an area in phase space (Fig.1.7(d)). this happens when the orbit, unrestricted by the existence of any conserved quantity, evolves in a *chaotic* manner whose detail is sensitively dependent on the values of s_1 and p_1.

Stability of periodic orbit The closed periodic orbits may be stable or unstable in the sense that an orbit starting at $\{s_1 + \delta s_1, p_1 + \delta p_1\}$, where δs_1 and δp_1 is small, may after many bounces remain near the closed orbit or may deviate increasingly from it. For an N periodic orbit, the deviation after N iterations will be:

$$\begin{pmatrix} \delta s_{n+1} \\ \delta p_{n+1} \end{pmatrix} = \mathscr{M}_N \begin{pmatrix} \delta s_1 \\ \delta p_1 \end{pmatrix} \tag{1.26}$$

where $\mathscr{M}_N$ is a 2×2 monodromy matrix. The orbital stability depends on the eigenvalues of the $\mathscr{M}_N$, given in terms of the trace by:

$$\lambda_{\pm} = \frac{1}{2} \left\{ Tr\mathscr{M}_N \pm [(Tr\mathscr{M}_N)^2 - 4]^{1/2} \right\} \tag{1.27}$$

After Nj iterations (i.e. j traversals of the closed orbit), the deviations $\left\{\delta s_{Nj}, \delta p_{Nj}\right\}$

can be written as a linear combination:

$$\begin{pmatrix} \delta s_{Nj} \\ \delta p_{Nj} \end{pmatrix} = A\lambda_+^j \begin{pmatrix} \delta s_+ \\ \delta p_+ \end{pmatrix} + B\lambda_-^j \begin{pmatrix} \delta s_- \\ \delta p_- \end{pmatrix} \tag{1.28}$$

There are three possibilities.

(i) Unstable periodic orbit (UPO) If $|Tr\mathscr{M}_N| > 2$, $\lambda\pm$ are real, so that

$$\lambda\pm^j = c^{\pm j\gamma} \tag{1.29}$$

The positive exponent guarantees that almost all the deviations grow exponentially so that orbit is unstable. γ here is called *Lyapunov exponent*, which is an index of instability of the orbit.

The dynamics in a stadium billiard with non-zero straight section is ergodic [11], i.e., all the orbits are unstable. The Lyapunov exponent of a UPO in stadium billiard can be derived from the monodromy matrix $\mathscr{M}_N = \prod_{i=1}^N m_i$, where m_i takes the form [12]:

$$m_i^s = \begin{pmatrix} 1 & 0 \\ -l_{i-1} & 1 \end{pmatrix} \tag{1.30}$$

for a point on a straight section, and

$$m_i^c = \begin{pmatrix} (2\alpha_i l_{i-1}/R) - 1 & 2\alpha_i/R \\ -l_i & -1 \end{pmatrix} \tag{1.31}$$

for a point on a semicircle. Here l_i is the path length form $(i-1)$th collision to ith collision, $\alpha_i = 1/sin\chi_i$, R is the radius of semicircle.

(ii) Stable periodic orbit If $|Tr\mathscr{M}_N| > 2$, it follows

$$\lambda\pm^j = c^{\pm i\, 2\pi\, j\, \beta} \tag{1.32}$$

In this case, the deviations oscillate about zero as j increases, and remain bounded. In phase space this shows island structures (Fig.1.7(c)). Here β is the winding number. It describes the number of turns of neighboring trajectories around the reference orbit in phase space [13].

(iii) Neutral periodic orbit For the case $|Tr\mathscr{M}_N| = 2$, the deviations increase linearly as j increase. A typical example is an orbit in circular billiard.

Stable and unstable manifolds The *stable manifold* of a periodic orbit is the set of points $\mathbf{x}$ such that the forward orbit starting from $\mathbf{x}$ approaches the fixed point. Similarly, the *unstable manifold* of a periodic orbit is the set of points $\mathbf{x}$ such that the orbit going backward in time starting from $\mathbf{x}$ approaches the fixed point [14]. Unstable manifold of an UPO can be acquired by Eq. 1.28, and Eq. 1.29 of the positive exponent term. While the stable manifold can also be acquired by the same manner of unstable manifold, but reverse the time (i.e., the orbit moves in the opposite direction).

Quantum Poincaré section: Husimi distribution

To study the classical correspondence of an eigenstate ψ of a quantum system, Husimi function is introduced by projection of the eigenstate onto a coherent state [15]:

$$H_\psi(\boldsymbol{q}_0, \boldsymbol{p}_0) = |\langle \boldsymbol{q}_0, \boldsymbol{p}_0 | \psi \rangle|^2 \tag{1.33}$$

Here $|\boldsymbol{q}_0, \boldsymbol{p}_0\rangle$ is a coherent state centered around $\boldsymbol{q}_0$ in configuration space and around $\boldsymbol{p}_0$ in momentum space. The coherent state can be expressed in position representation as:

$$\langle \boldsymbol{q} | \boldsymbol{q}_0, \boldsymbol{p}_0 \rangle = (\frac{1}{\pi\sigma^2})^{1/4}\, exp\left[-\frac{(\boldsymbol{q}-\boldsymbol{q}_0)^2}{2\sigma^2} + i\,\boldsymbol{p}_0 \cdot (\boldsymbol{q}-\boldsymbol{q}_0)/\hbar\right], \tag{1.34}$$

where $\sigma/\sqrt{2}$ is the dispersion in position, and $1/(\sigma\sqrt{2})$ is the dispersion in momentum space. So the Husimi function can be written as:

$$H_\psi(\boldsymbol{q}_0, \boldsymbol{p}_0) = (\frac{1}{\pi\sigma^2})^{1/2} \left| \int d^2\boldsymbol{q}\, exp\left[-\frac{(\boldsymbol{q}-\boldsymbol{q}_0)^2}{2\sigma^2} + i\,\boldsymbol{p}_0 \cdot (\boldsymbol{q}-\boldsymbol{q}_0)/\hbar\right] \psi(\boldsymbol{q}) \right|^2 \tag{1.35}$$

There're several cases Husimi distribution can be simplified.

Circular cavity Comparing with the classical Poincaré SOS, we are interested in the Husimi distribution at the boundary. So we can take simplifications: $\boldsymbol{q} \rightarrow s$, and $\boldsymbol{p}_0 \cdot (\boldsymbol{q} - \boldsymbol{q}_0)/\hbar \rightarrow k\, sin(\chi)\,(s - s_0)$, where k is the wave number. And due to the periodicity of s, Eq. 1.34 becomes:

$$\begin{aligned}\langle s|s_0, k_s\rangle_{per} &= \sum_{n=-\infty}^{\infty} \langle s-n|s_0, k_s\rangle \\ &= (\frac{1}{\pi\sigma^2})^{1/4} \sum_{n=-\infty}^{\infty} exp\left[-\frac{(s-n-s_0)^2}{2\sigma^2} + i\,k\,sin(\chi)\,(s-n-s_0)\right]\end{aligned} \tag{1.36}$$

with $s, s_0 \subset [0, 1)$. Here $k_s = k\, sin(\chi)$, is the tangential component of $\boldsymbol{k}$ at the position s_0. So the Husimi distribution can be calculated from:

$$H_\psi(s, k_s) = \left| \int_0^1 ds' \, \left\langle s, k_s|s'\right\rangle_{per} \, \psi(s') \right|^2 \tag{1.37}$$

Closed cavity For a cavity with arbitrary boundary shape, we can't perform the separation of variables to make it a $1D$ integral. Yet in a closed cavity, the wave function ψ at the boundary is zero. So ψ closed to the boundary $\mathscr{B}$ is approximated as [15]:

$$\psi(r, s) \approx S(s) \equiv \left.\frac{\partial\psi(r, s)}{\partial r}\right|_{\mathscr{B}} = \boldsymbol{\nabla}\psi \cdot \boldsymbol{r}|_{\mathscr{B}} \tag{1.38}$$

So Husimi function can be approximately:

$$H_\psi(s, k_s) \approx \left| \int_0^1 ds' \, \left\langle s, k_s|s'\right\rangle_{per} \, S(s') \right|^2 \tag{1.39}$$

Husimi function at dielectric interface When dealing with optical system, mostly the cavity is made of dielectric material without metal coating on the boundary. So the boundary condition is more complicated. And light can not always be confined within the cavity, but may escape from the cavity at certain incident angle. A modification of Husimi distribution of Eq. 1.35 is introduced by using four Husimi representations $H_j^{inc,em}$ for incident (inc) and emerging (em) rays inside ($j = 1$) and outside ($j = 0$) the interface [16]:

$$H_j^{inc(em)}(\boldsymbol{q}_0, \boldsymbol{p}_0) \sim \frac{k_j}{2\pi} \left| (-1)^j \mathcal{F}_j \, h_j(\boldsymbol{q}_0, \boldsymbol{p}_0) + (-) \frac{i}{k_0 \, \mathcal{F}_j} h'_j(\boldsymbol{q}_0, \boldsymbol{p}_0) \right|^2 \tag{1.40}$$

with the angular-momentum-dependent weighting factor $\mathcal{F}_j = \sqrt{n_j \, cos(\chi_j)}$, n_j is the refractive index inside ($j = 1$) and outside ($j = 0$) the cavity. The functions

$$h_j(\boldsymbol{q}_0, \boldsymbol{p}_0) = \int d^2\boldsymbol{q} \, exp \left[-\frac{(\boldsymbol{q} - \boldsymbol{q}_0)^2}{2\sigma^2} + i \, \boldsymbol{p}_0 \cdot (\boldsymbol{q} - \boldsymbol{q}_0)/\hbar \right] \psi_j(\boldsymbol{q}) \tag{1.41}$$

$$h'_j(\boldsymbol{q}_0, \boldsymbol{p}_0) = \int d^2\boldsymbol{q} \, exp \left[-\frac{(\boldsymbol{q} - \boldsymbol{q}_0)^2}{2\sigma^2} + i \, \boldsymbol{p}_0 \cdot (\boldsymbol{q} - \boldsymbol{q}_0)/\hbar \right] \psi'_j(\boldsymbol{q}) \tag{1.42}$$

are the overlaps of the wave function ψ and its normal (radial) derivative ψ', taken on the respective side j of the interface, with the coherent state. For a circular cavity, we can do further simplifications, and the integral (Eq. 1.41, 1.42) will be reduced to $1D$ problem as mentioned above, which shows the results of reference [16].

1.4 Finite-difference time-domain method

Finite-difference time-domain (FDTD) method is a powerful computational electrodynamics modeling technique. First introduced by Yee in 1966 [17], this method has been developed for decays and become more and more popular with the advance of computer power. The basic ideal of this method is central difference approximation for Maxwell's curl equations, both in space and time. FDTD enables the accurate characterization of complex inhomogeneous structures for which analytical methods are ill-suited.

Yee's algorithm Maxwell's curl equations in an isotropic medium are

$$\frac{\partial \boldsymbol{B}}{\partial t} + \boldsymbol{\nabla} \times \boldsymbol{E} = 0 \tag{1.43}$$

$$\frac{\partial \boldsymbol{D}}{\partial t} - \boldsymbol{\nabla} \times \boldsymbol{H} = \boldsymbol{J} \tag{1.44}$$

with

$$\boldsymbol{D} = \epsilon \boldsymbol{E}; \qquad \boldsymbol{B} = \mu \boldsymbol{H}; \qquad \boldsymbol{J} = \sigma \boldsymbol{E} \tag{1.45}$$

where ϵ is the electrical permittivity, μ is the magnetic permeability, and σ is electric conductivity. Equations 1.43 and 1.44 can rewrite as

$$\frac{\partial \boldsymbol{H}}{\partial t} = -\frac{1}{\mu} \boldsymbol{\nabla} \times \boldsymbol{E} \tag{1.46}$$

$$\frac{\partial \boldsymbol{E}}{\partial t} = \frac{1}{\epsilon} \boldsymbol{\nabla} \times \boldsymbol{H} - \frac{1}{\epsilon} \sigma \boldsymbol{E} \tag{1.47}$$

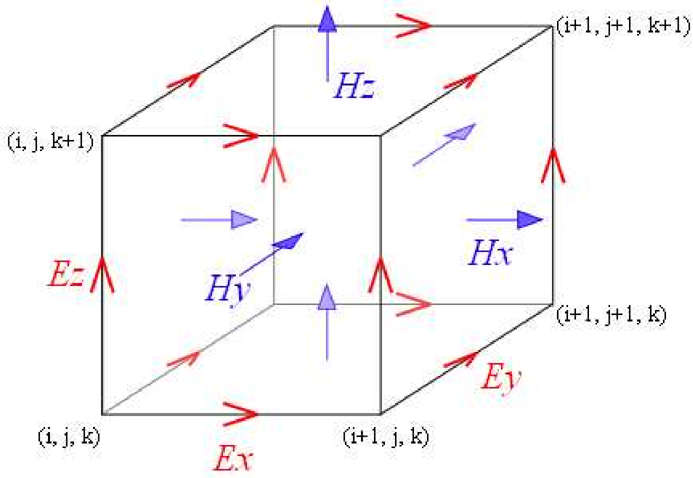

Figure 1.8: Illustration of a standard Yee lattice used for FDTD, in which different field components use different locations in a single unit cell.

In Cartesian coordinates, this yields six coupled scalar equations

$$\begin{aligned}
\frac{\partial H_x}{\partial t} &= \frac{1}{\mu}\left(\frac{\partial E_y}{\partial z} - \frac{\partial E_z}{\partial y}\right) \\
\frac{\partial H_y}{\partial t} &= \frac{1}{\mu}\left(\frac{\partial E_z}{\partial x} - \frac{\partial E_x}{\partial z}\right) \\
\frac{\partial H_z}{\partial t} &= \frac{1}{\mu}\left(\frac{\partial E_x}{\partial y} - \frac{\partial E_y}{\partial x}\right) \\
\frac{\partial E_x}{\partial t} &= \frac{1}{\epsilon}\left(\frac{\partial H_z}{\partial y} - \frac{\partial H_y}{\partial z} - \sigma E_x\right) \\
\frac{\partial E_y}{\partial t} &= \frac{1}{\epsilon}\left(\frac{\partial H_x}{\partial z} - \frac{\partial H_z}{\partial x} - \sigma E_y\right) \\
\frac{\partial E_z}{\partial t} &= \frac{1}{\epsilon}\left(\frac{\partial H_y}{\partial x} - \frac{\partial H_x}{\partial y} - \sigma E_z\right)
\end{aligned} \tag{1.48}$$

In Yee's algorithm, we denote a space point in a uniform, rectangular lattice as

$$(i, j, k) = (i\Delta x, j\Delta y, k\Delta z) \tag{1.49}$$

Here, $\Delta x, \Delta y, \Delta z$ are, respectively, the lattice space increments in the x, y, and z coordinate directions, and i, j, and k are integers. Further, we denote any function F of space and time evaluated at a discrete point in the grid and at a discrete point of time as

$$F^n(i,j,k) = F(i\Delta x, j\Delta y, k\Delta z, n\Delta t) \tag{1.50}$$

Using central finite difference approximations, the spatial and temporal derivative of F are written as

$$\frac{\partial F^n(i,j,k)}{\partial x} = \frac{F^n(i+1/2,j,k) - F^n(i-1/2,j,k)}{\Delta x} \tag{1.51}$$

$$\frac{\partial F^n(i,j,k)}{\partial t} = \frac{F^{n+1/2}(i,j,k) - F^{n-1/2}(i,j,k)}{\Delta t} \tag{1.52}$$

By applying Eq. 1.51 and 1.52 into the scalar equation 1.48, we get six explicit finite difference equations

$$\begin{aligned} E_x\big|^{n+1}_{i+1/2,j,k} &= \left(\frac{1 - \frac{\sigma_{i+1/2,j,k}\Delta t}{2\epsilon_{i+1/2,j,k}}}{1 + \frac{\sigma_{i+1/2,j,k}\Delta t}{2\epsilon_{i+1/2,j,k}}} \right) E_x\big|^{n}_{i+1/2,j,k} \\ &+ \left(\frac{\frac{\Delta t}{\epsilon_{i+1/2,j,k}}}{1 + \frac{\sigma_{i+1/2,j,k}\Delta t}{2\epsilon_{i+1/2,j,k}}} \right) \left[\frac{H_z\big|^{n+1/2}_{i+1/2,j+1/2,k} - H_z\big|^{n+1/2}_{i+1/2,j-1/2,k}}{\Delta y} \right. \\ &\qquad \left. - \frac{H_y\big|^{n+1/2}_{i+1/2,j,k+1/2} - H_y\big|^{n+1/2}_{i+1/2,j,k-1/2}}{\Delta z} \right] \end{aligned} \tag{1.53}$$

$$E_y\Big|_{i,j+1/2,k}^{n+1} = \left(\frac{1 - \frac{\sigma_{i,j+1/2,k}\Delta t}{2\epsilon_{i,j+1/2,k}}}{1 + \frac{\sigma_{i,j+1/2,k}\Delta t}{2\epsilon_{i,j+1/2,k}}} \right) E_x\Big|_{i,j+1/2,k}^{n} + \left(\frac{\frac{\Delta t}{\epsilon_{i,j+1/2,k}}}{1 + \frac{\sigma_{i,j+1/2,k}\Delta t}{2\epsilon_{i,j+1/2,k}}} \right) \left[\frac{H_x\Big|_{i,j+1/2,k+1/2}^{n+1/2} - H_x\Big|_{i,j+1/2,k-1/2}^{n+1/2}}{\Delta z} - \frac{H_z\Big|_{i+1/2,j+1/2,k}^{n+1/2} - H_z\Big|_{i-1/2,j+1/2,k}^{n+1/2}}{\Delta x} \right] \tag{1.54}$$

$$E_z\Big|_{i,j,k+1/2}^{n+1} = \left(\frac{1 - \frac{\sigma_{i,j,k+1/2}\Delta t}{2\epsilon_{i,j,k+1/2}}}{1 + \frac{\sigma_{i,j,k+1/2}\Delta t}{2\epsilon_{i,j,k+1/2}}} \right) E_x\Big|_{i,j,k+1/2}^{n} + \left(\frac{\frac{\Delta t}{\epsilon_{i,j,k+1/2}}}{1 + \frac{\sigma_{i,j,k+1/2}\Delta t}{2\epsilon_{i+1/2,j,k}}} \right) \left[\frac{H_y\Big|_{i+1/2,j,k+1/2}^{n+1/2} - H_y\Big|_{i-1/2,j,k+1/2}^{n+1/2}}{\Delta x} - \frac{H_x\Big|_{i,j+1/2,k+1/2}^{n+1/2} - H_x\Big|_{i,j-1/2,k+1/2}^{n+1/2}}{\Delta y} \right] \tag{1.55}$$

$$H_x\Big|_{i,j+1/2,k+1/2}^{n+1/2} = H_x\Big|_{i,j+1/2,k+1/2}^{n-1/2} + \left(\frac{\frac{\Delta t}{\mu_{i,j+1/2,k+1/2}}}{1+\frac{\Delta t}{2\mu_{i,j+1/2,k+1/2}}}\right)\left[\frac{E_y\big|_{i,j+1/2,k+1}^{n} - E_y\big|_{i,j+1/2,k}^{n}}{\Delta z} - \frac{E_z\big|_{i,j+1,k+1/2}^{n} - E_z\big|_{i,j,k+1/2}^{n}}{\Delta y}\right] \quad (1.56)$$

$$H_y\Big|_{i+1/2,j,k+1/2}^{n+1/2} = H_y\Big|_{i+1/2,j,k+1/2}^{n-1/2} + \left(\frac{\frac{\Delta t}{\mu_{i+1/2,j,k+1/2}}}{1+\frac{\Delta t}{2\mu_{i+1/2,j,k+1/2}}}\right)\left[\frac{E_z\big|_{i+1,j,k+1/2}^{n} - E_z\big|_{i,j,k+1/2}^{n}}{\Delta x} - \frac{E_x\big|_{i+1/2,j,k+1}^{n} - E_x\big|_{i+1/2,j,k}^{n}}{\Delta z}\right] \quad (1.57)$$

$$H_z\Big|_{i+1/2,j+1/2,k}^{n+1/2} = H_z\Big|_{i+1/2,j+1/2,k}^{n-1/2} + \left(\frac{\frac{\Delta t}{\mu_{i+1/2,j+1/2,k}}}{1+\frac{\Delta t}{2\mu_{i+1/2,j+1/2,k}}}\right)\left[\frac{E_x\big|_{i+1/2,j+1,k}^{n} - E_x\big|_{i+1/2,j,k}^{n}}{\Delta y} - \frac{E_y\big|_{i+1,j+1/2,k}^{n} - E_y\big|_{i,j+1/2,k}^{n}}{\Delta x}\right] \quad (1.58)$$

The location of each component in a single unit cell is shown in Fig. 1.8. $\boldsymbol{E}$ and $\boldsymbol{H}$ are evaluated at alternate half time steps, such that all field components are calculated in each time step Δt.

Since FDTD simulations calculate the $\boldsymbol{E}$ and $\boldsymbol{H}$ fields at all points of computational domain, in many cases an artificial boundary is needed due to finite computing power. Such boundary must be constructed so that the solution region appears to extend infinitely in all directions. *Perfectly matched layer* (PML) formulations [18] is one of many commonly used grid truncation techniques. The basic idea is to construct artificial layers, within which the transmitted wave propagates with the same speed and direction as the impinging wave while simultaneously undergoing exponential decay along the axis normal to the interface. In this way, the scattering from the boundary layers can be very small so that it will not affect the accuracy of the simulation.

FDTD simulation with rate equations To simulate nonlinear process such as lasing behavior in microcavities, we propose an extended FTDT scheme incorporating rate equations [19]. The rate equations describe the time evolution of the atomic energy level populations under the influence of applied signals. The system considered here is a simplified yet realistic four-level atomic system (Fig. 1.9) with energy levels $\epsilon_0, \epsilon_1, \epsilon_2, \epsilon_3$, and populations N_0, N_1, N_2, and N_3, respectively. W_p is the external pumping rate that transfers atoms from the ground ϵ_0 state to the level ϵ_3. $1/\tau_{ij}$ is the decay rate of an atom from energy level ϵ_i to level ϵ_j.

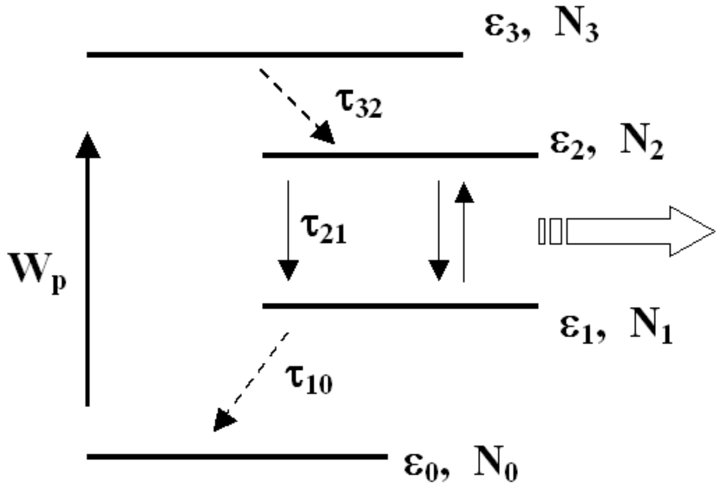

Figure 1.9: Population in four-level atomic system

The populations of each energy level can be modeled by the following rate equations

$$\frac{dN_3(t)}{dt} = W_p(t)N_0(t) - \frac{N_3(t)}{\tau_{32}} \tag{1.59}$$

$$\frac{dN_2(t)}{dt} = \frac{N_3(t)}{\tau_{32}} + \frac{1}{\hbar\omega_a}\boldsymbol{E}(t) \cdot \frac{d\boldsymbol{P}(t)}{dt} - \frac{N_2(t)}{\tau_{21}} \tag{1.60}$$

$$\frac{dN_1(t)}{dt} = \frac{N_2(t)}{\tau_{21}} - \frac{1}{\hbar\omega_a}\boldsymbol{E}(t) \cdot \frac{d\boldsymbol{P}(t)}{dt} - \frac{N_1(t)}{\tau_{10}} \tag{1.61}$$

$$\frac{dN_3(t)}{dt} = \frac{N_1(t)}{\tau_{10}} - W_p(t)N_0(t) \tag{1.62}$$

where $\hbar\omega_a = \epsilon_2 - \epsilon_1$ is the emission energy, $\boldsymbol{P}(t)$ macroscopic polarization, $\boldsymbol{E}(t)$ is the electric field. The term $\frac{1}{\hbar\omega_a}\boldsymbol{E}(t)\cdot\frac{d\boldsymbol{P}(t)}{dt}$ is the classical expression for instantaneous energy transfer divided by the energy per photon, and is equivalent to stimulated transition probabilities more commonly used in the rate equation.

Accordingly, Maxwell's equation in Eq. 1.46 and 1.47 can be rewritten as

$$\boldsymbol{\nabla} \times \boldsymbol{E} = -\mu \frac{\partial \boldsymbol{H}}{\partial t} \tag{1.63}$$

$$\boldsymbol{\nabla} \times \boldsymbol{H} = \epsilon_0 \frac{\partial \boldsymbol{E}}{\partial t} + \frac{\partial \boldsymbol{P}}{\partial t} + \sigma \boldsymbol{E} \tag{1.64}$$

where ϵ_0 is the vacuum electrical permittivity. The relation between $\boldsymbol{P}$ and $\boldsymbol{E}$ for an isotropic dielectric medium can be described by the following equation

$$\frac{d^2\boldsymbol{p}(t)}{dt^2} + \Delta\omega_a \frac{d\boldsymbol{p}(t)}{dt} + \omega_a^2 \boldsymbol{p}(t) = \frac{\gamma_r}{\gamma_c}\left(\frac{e^2}{m}\right)(N_1(t) - N_2(t))\,\boldsymbol{E}(t) \tag{1.65}$$

Here $\Delta\omega_a$ is the actual linewidth (gain spectrum width) of the transition centered at angular frequency ω_a. e and m are single electron charge and mass, correspondingly. γ_r is the real atomic transition rate, and γ_c is the classical electron oscillator decay rate, given by

$$\gamma_c = \left(\frac{e^2}{m}\right)\frac{\omega_a^2}{6\pi\epsilon_0 c^3} \tag{1.66}$$

c is the speed of light in vacuum.

Thus by applying N_0, N_1, N_2, N_3 and $\boldsymbol{p}$ to each unit cell in Yee's lattice, we calculate the evolution of population at each energy level for each time step with the changes of field components, and followed by updating the macroscopic polarization $\boldsymbol{p}$ with Eq. 1.65

and centered difference approximation

$$\begin{aligned}\frac{\partial^2 F^n(i,j,k)}{\partial t^2} &= \left(\frac{F^{n+1}(i,j,k)-F^n(i,j,k)}{\Delta t} - \frac{F^n(i,j,k)-F^{n-1}(i,j,k)}{\Delta t}\right)/\Delta t \\ &= \frac{F^{n+1}(i,j,k)-2F^n(i,j,k)+F^{n-1}(i,j,k)}{\Delta t^2}\end{aligned} \tag{1.67}$$

The following chapters are organized as below. Due to it small size and high-Q, microdisk shows prominent quantum effects. Semiconductor microdisks have been used as a tool to study cavity quantum electrodynamics (QED). In Chapter 2, we demonstrate our experimental observations of spontaneous emission rate enhancement from quantum dots in microdisk. In reality, defects are inevitable during the fabrication process. The roughness on the boundary of microdisk will strongly affect the WGMs, and eventually spoil the Q factor. In Chapter 3, we show our studies on microdisk lasers with rough boundaries that dynamical localization will suppress the classical diffusion in angular momentum space and result in high-Q mode. Contrast to small scale deformation on the boundary profile, in Chapter 4, we present our numerical and experimental studies of large scale deformation - stadium cavities. And finally, we demonstrate some applications of semiconductor microdisk laser in Chapter 5.

CHAPTER 2

ENHANCEMENT OF SPONTANEOUS EMISSION OF QUANTUM DOTS IN MICRODISK

2.1 Purcell factor

The emission of a photon from an excited atom is a result of the interaction between the atom and quantized vacuum field. Therefor the spontaneous emission (SE) is affected by the nature of quantized vacuum field around the atom. Just like classical electromagnetic field can be modified by optical cavities to form different cavity modes, so can be quantized vacuum field. Therefore a properly designed microcavity can strongly modified the spontaneous emission of an emitter inside it.

Control of spontaneous emission in a microcavity has many applications, e.g. improvement of the efficiency of light emitting devices, generation of non-classical states of light [20, 21]. A microcavity reduces the number of allowed optical modes, but increases the vacuum field intensity in these resonant modes. The spontaneous emission outside the cavity resonance is suppressed, while the spontaneous emission within the cavity resonance is enhanced. For an emitter that has negligible linewidth and is ideally spatially and spectrally coupled to a cavity mode, its spontaneous emission rate is enhanced by the Purcell factor

$$F_p = \frac{3Q(\lambda/n)^3}{4\pi^2 V_{eff}}, \tag{2.1}$$

where Q is the cavity quality factor, V_{eff} is the effective mode volume, λ is the emission wavelength, and n is the index of refraction [22]. Initial experiments of spontaneous emission control are performed on atoms [23–26]. Recently, semiconductor quantum dots (QDs), sometimes called "artificial atoms", attract much interest for spontaneous emission control [27–33]. Using the self-organized growth technique possible with highly-strained systems, InGaAs quantum dots are formed and exhibit three-dimensional confinement of electrons. Owing to their discrete density of electronic states, self-assembled InGaAs QDs have extremely narrow homogeneous linewidth.

QDs embedded in microdisks are ideal systems for spontaneous emission control [34–36]. The whispering gallery (WG) modes of microdisks have low volume and high quality factor [38]. The homogeneous linewidth of InAs quantum dots is smaller than the spectral width of WG modes. Thus, a large enhancement of the spontaneous emission rates should be expected for QDs coupled to WG modes. However, inhomogeneous broadening of QD energy levels and random spatial distribution of QDs in microdisks lead to complications. The coupling of a QD to a WG mode depends both on the spectral matching of the QD emission line with the WG mode frequency and on the spatial overlap of the QD with the WG mode. Hence, the QDs, with different emission frequencies and spatial locations, undergo different spontaneous emission rate enhancement. The average enhancement factor is much less than the Purcell factor [35]. Recently, the Purcell effect of a single

InAs QD in a GaAs microdisk is studied [36]. Although the frequency of the QD can be tuned into resonance with a WG mode, its location in the microdisk cannot be controlled. The spatial mismatch between the single QD and the WG mode reduces the spontaneous emission enhancement factor.

In this Chapter, we demonstrate our directly measure the lifetime of radiative decay of InAs QDs coupled to WG modes of GaAs microdisks [37]. Using the non-negative least squares algorithm, we recover the distribution of spontaneous emission rates for an ensemble of QDs. The maximum enhancement factor of spontaneous emission rate exceeds 10.

2.2 Sample fabrication and optical measurement

The quantum dot sample is grown by molecular beam epitaxy. The structure consists of a GaAs buffer layer, 500 nm $Al_{0.7}Ga_{0.3}As$, 45 nm GaAs, 2 monolayer (ML) InAs quantum dots, 45 nm GaAs (Fig. 2.1 (a)). The areal density of InAs QDs is $\sim 10^{11}$ cm^{-2}. The photoluminescence (PL) spectrum of quantum dots at 5 K is centered around 970 nm with a full width at half maximum (FWHM) of 20 nm.

The microdisks are fabricated by electron beam lithography and two-steps of wet etching process [39]. As shown in Fig. 2.2, 100 nm silicon dioxide (SiO_2) is deposited on the wafer and used as the etch mask. Disk patterns are defined by electron beam lithography with negative resist. Then the pattern is transferred from the *e*-beam resist to the SiO_2 etch mask by reactive ion etch (RIE). It is followed by two steps of wet

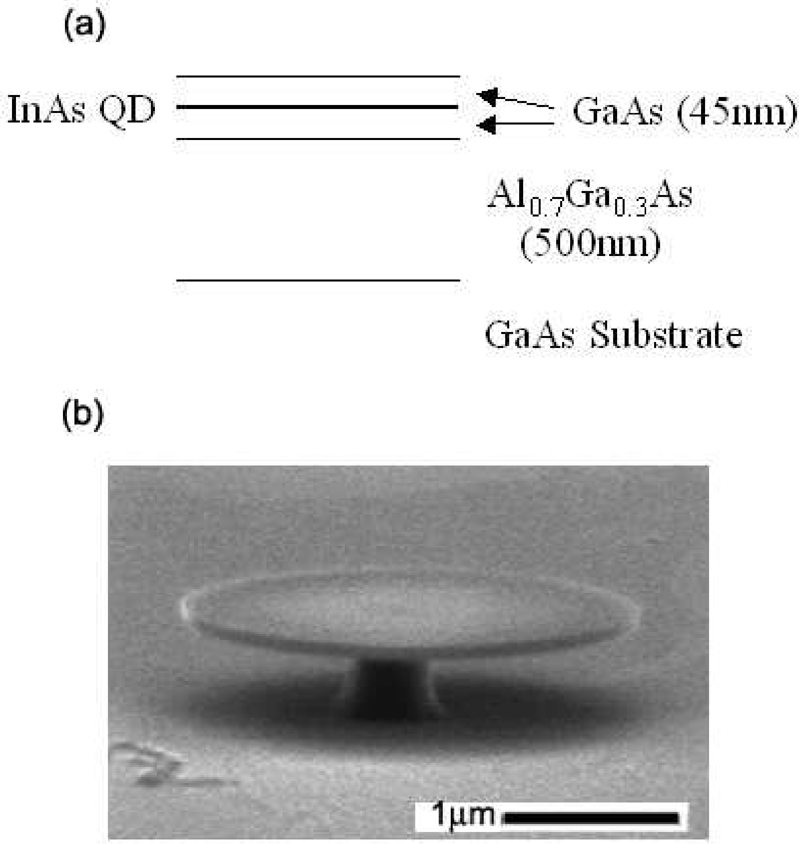

Figure 2.1: (a) Layer structure of quantum dot wafer. (b) Scanning electronic microscope (SEM) image of a microdisk

etch. The first step is a non-selective etch, i.e., the sample is unselectively etched down to the GaAs buffer layer in a dilute water solution of phosphoric acid (H_3PO_4) and hydrodioxide (H_2O_2). The etch rate is low enough to allow a good control of etch depth. The second step is a selective etch. A dilute solution of hydrofluoric acid (HF) is used to etch the $Al_{0.7}Ga_{0.3}$ layer without attacking GaAs layers and InAs quantum dots. With careful control of the etch time, microdisk structures are formed on top of the pedestals. diameter of the disks is $\sim 3\ \mu$m. Each disk is supported by a 500-nm long $Al_{0.7}Ga_{0.3}$ as pedestal. The thickness of the disk is designed to be 90 nm so that it only supports the lowest order transverse electric (TE) mode in the direction perpendicular to the disk plane.

The sample is mounted in a liquid helium cryostat, as shown in Fig. 2.3. The sample temperature is set at 5 K. The microdisks are optically excited by 200 fs pulses from a mode-locked Ti:Sapphire laser with the repetition rate of 76 MHz. The excitation wavelength is fixed at 780 nm (1.59 eV). A microscope objective lens focuses the pump beam onto a single microdisk at normal incidence. The emission is collected from the side of the microdisk with a short achromatic lens. A beam splitter splits the collected emission into two. One half is dispersed by a 0.3 meter monochromator with 600 grooves/mm grating, and then goes into a Hamamatsu streak camera for lifetime measurement. The temporal resolution is 17 ps. The other half is directed to a 0.5 meter spectrometer with 1800 grooves/mm grating, and detected by liquid nitrogen cooled CCD array detector for simultaneous spectral measurement. The spectral resolution is about 0.06 nm. Bandpass

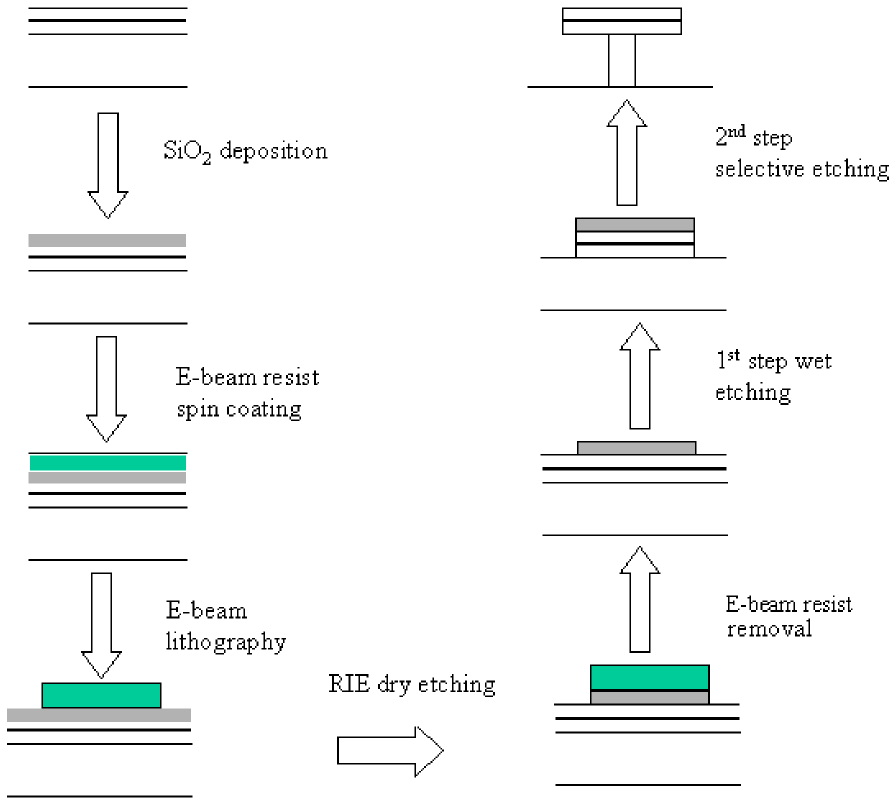

Figure 2.2: Fabrication process of microdisks.

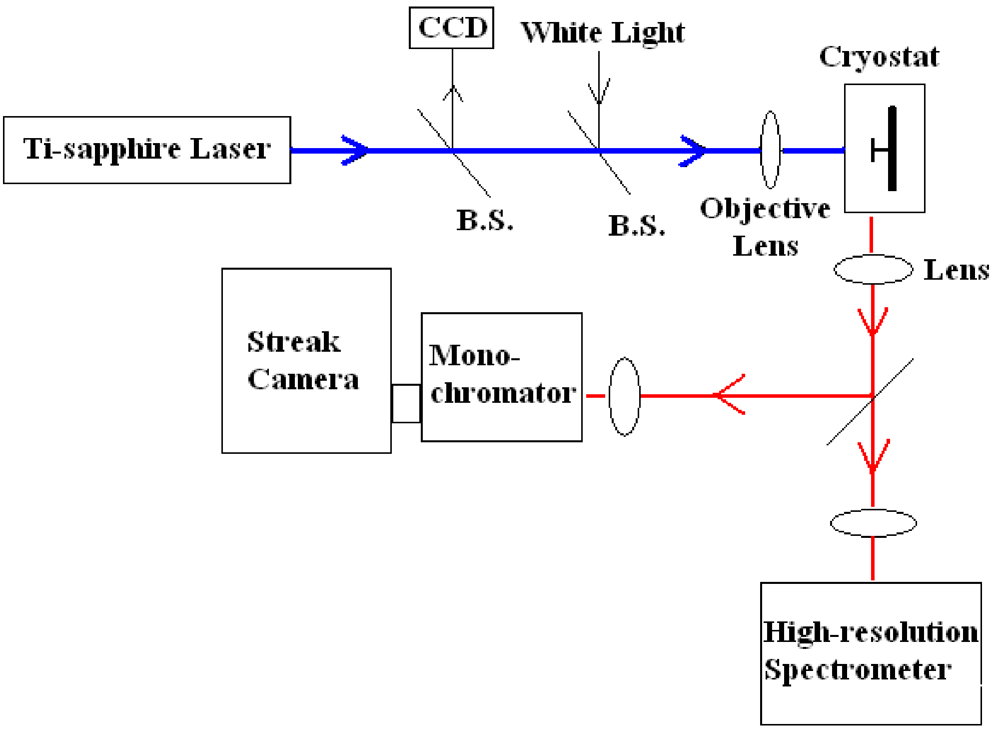

Figure 2.3: Optical measurement setup.

filters are used to attenuate the scattered pump light.

Figure 2.4 (a) shows a two dimensional ($2D$) image taken by the monochromator-streak camera. The incident pump intensity is 4.2×10^2 W/cm^2. The horizontal axis is wavelength, the vertical axis is time. Figure 2.4 (b) is the time-integrated spectra obtained from Fig. 2.4 (a). The spectral peaks at 965.6 nm and 973.5 nm correspond to the WG modes $TE_{17,1}$ and $TE_{13,2}$, respectively. The background emission, with nearly constant intensity over the measured wavelength range, comes from the spontaneous emission of QDs that are not coupled to the cavity modes. From Fig. 2.4 (a), we extract the time traces of PL at various frequencies. For wavelengths both shorter and longer than the cavity resonances, the PL curves exhibit mono-exponential decay. The decay time, obtained from mono-exponential curve fitting, is ~ 570 ps (Fig. 2.5). This value is close to the measured decay time of InAs QDs in the unprocessed sample.

Figure 2.5 also plots the PL curve at the wavelength of $TE_{13,2}$ mode. From the spectral linewidth of $TE_{13,2}$ mode measured by the 0.5-meter spectrometer with 1800 grooves/mm grating, we find its Q value is around 3600. The InAs QDs, located near the center of the microdisk, have little spatial overlap with the $TE_{13,2}$ mode. Thus their coupling to $TE_{13,2}$ mode is very weak, even if their emission frequency is in resonance with the $TE_{13,2}$ mode. In anther word, the collected PL at the wavelength of $TE_{13,2}$ mode consists of a resonant part and a nonresonant part. The resonant part represents the emission of QDs into the $TE_{13,2}$ mode, while the nonresonant part comes from the emission of uncoupled QDs. We curve fit the temporal decay of PL with a double-exponential function $I(t) = I_1 \exp[-(t - t_0)/t_1] + I_2 \exp[-(t - t_0)/t_2] + I_0$. The first term corresponds to the resonant part, the second term is the nonresonant part, the third term is the background noise. t_1 represents the decay time averaged over all coupled QDs. t_2 is the off-resonant spontaneous emission decay time. According to the curve fit of PL decay at off-resonance wavelength, the value of t_2 is set at 570 ps. t_0 represents the starting point of the curve fit. In our case, the curve fit starts after the emission pulse reaches its intensity maximum. I_1, I_2, and I_0 are fitting parameters. The fitted curve is plotted in Fig. 2.5. The fitting result gives $t_1 = 150$ ps. Thus, the average enhancement factor for spontaneous emission rates of coupled QDs is 3.8.

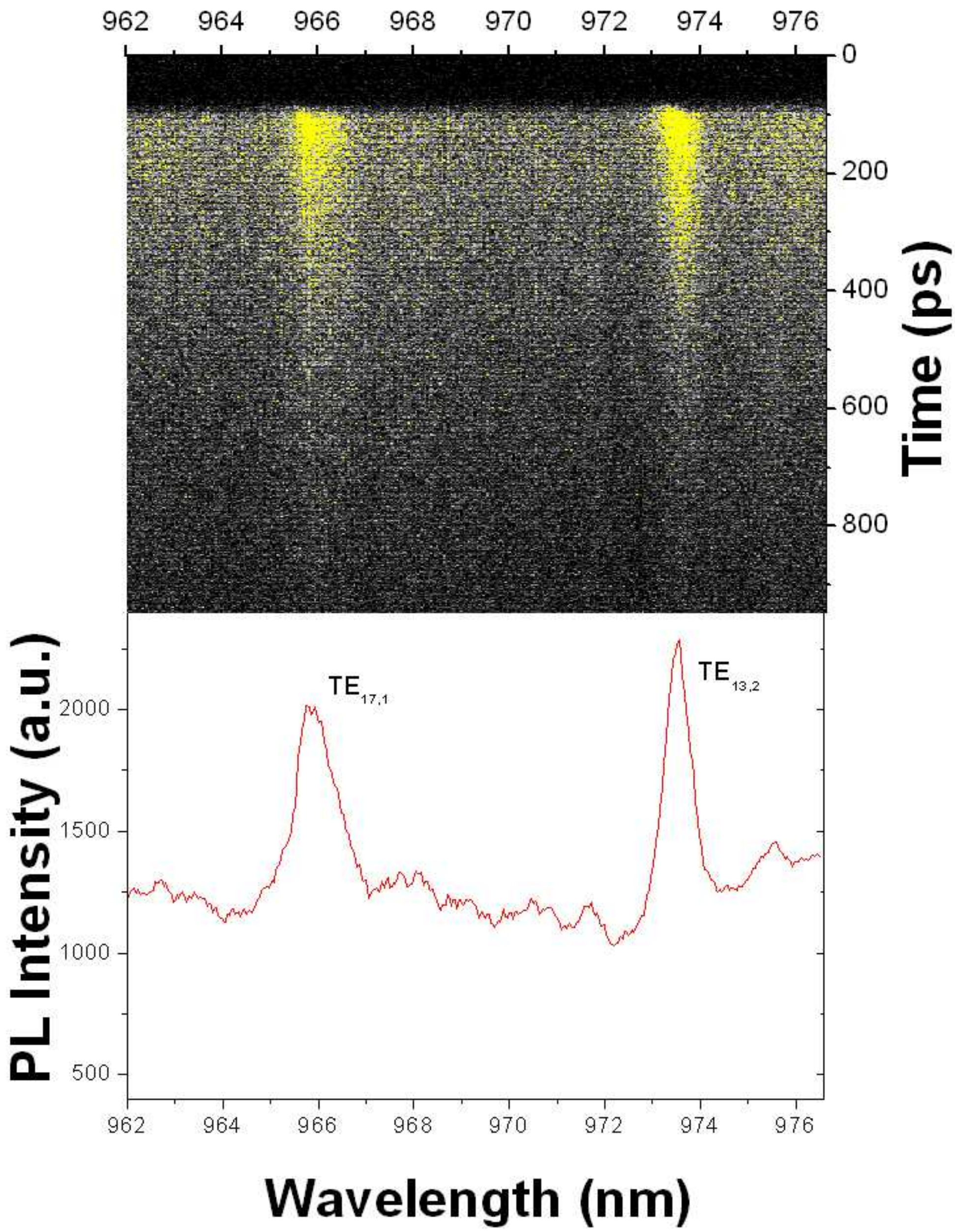

Figure 2.4: a) A 2D image of InAs QD emission from a 3 μm disk taken by the monochromater-streak camera. The incident pump intensity is $4.2{\times}10^2$ W/cm^2. (b) The time-integrated spectrum obtained from (a).

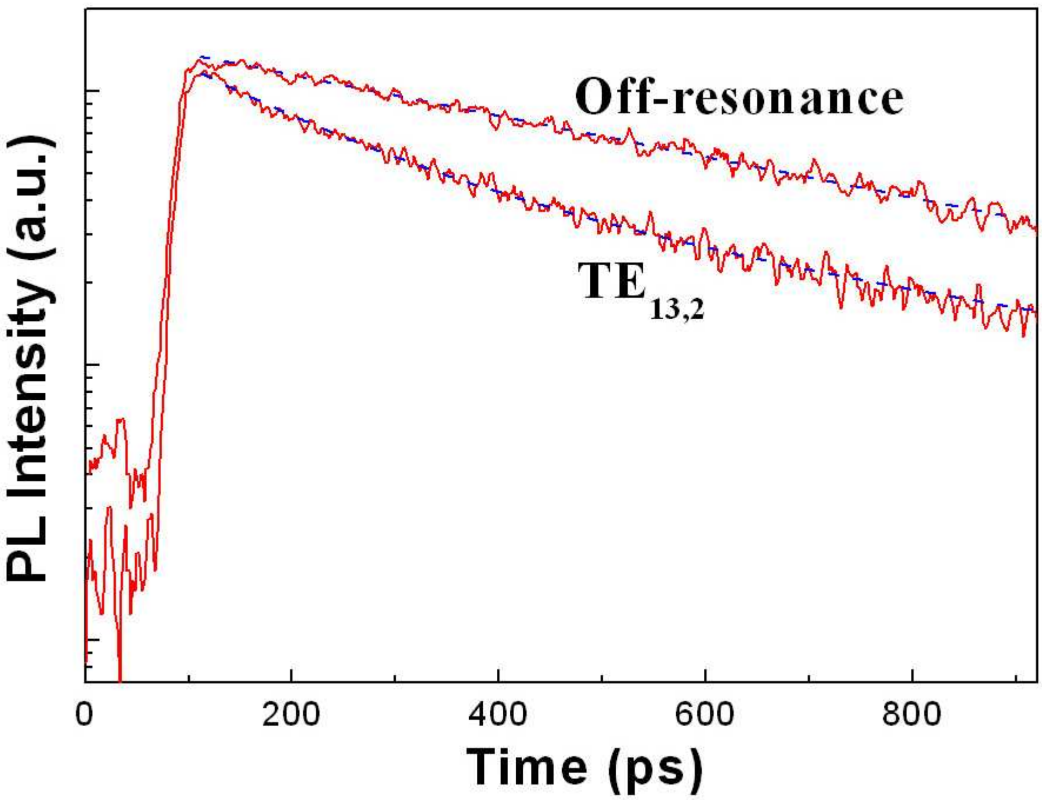

Figure 2.5: Time-resolved PL curves extracted from Fig. 2.4 (a) at the wavelengths 977.7 nm (curve A), and 973.5 nm (curve B). The dotted line represents a mono-exponential fit for curve A. The dashed line represents a double-exponential fit for curve B.

2.3 Distribution of spontaneous emission rates

First, we briefly derive the expression of Purcell factor. Consider a radiating dipole weakly coupled to the field in a cavity, if the emission line is much narrower spectrally than the cavity resonance, we can calculate its spontaneous emission rate through the *Fermi Golden Rule* [40]

$$\gamma = \frac{2\pi}{\hbar^2}\rho(\omega_e)\left\langle |\langle \boldsymbol{d}\cdot\hat{\boldsymbol{\epsilon}}(\boldsymbol{r_e})\rangle|^2 \right\rangle \tag{2.2}$$

where $\rho(\omega_e)$ is the density of photon modes at the emitter's angular frequency ω_e, $\hat{\boldsymbol{\epsilon}}$ is the electric field operator, $\boldsymbol{r_e}$ is the location of the emitter, and the averaging of the squared dipolar matrix element is performed over the various modes "seen" by the emitter. Field quantization leads to the following expression for the electric field operator for the cavity mode

$$\hat{\boldsymbol{E}}(\boldsymbol{r},t) = i\,\epsilon_{max}\boldsymbol{f}\hat{a}(t) + h.c. \tag{2.3}$$

where $h.c.$ is Hermitian conjugate, and $\hat{a}$ is the photon creation operator. $\boldsymbol{f}$ is a complex vector of the mode spatial function which describes the local field polarization and relative field amplitude. It's normalized so that its norm is unity at the antinode of the electric field. ϵ_{max} can be estimated by expressing of vacuum-field energy $\hbar\omega/2$

$$\epsilon_{max} = \sqrt{\frac{\hbar\omega}{2\epsilon_0 n^2 V_{eff}}} \tag{2.4}$$

$$V_{eff} = \frac{1}{n^2} \int n(\boldsymbol{r})^2 \, |\boldsymbol{f}(\boldsymbol{r})| \, d^3\boldsymbol{r} \tag{2.5}$$

n is the refractive index at the field maximum and V_{eff} is the effective cavity volume, which describes how efficiently the cavity concentrates the EM field in a restricted space.

For a cavity supporting a single-mode (angular frequency ω_c, linewidth $\Delta\omega_c$, and quality factor $Q = \omega_c/\Delta\omega_c$), the mode density seen by the emitter is given by a normalized Lorentzian

$$\rho_{cav}(\omega) = \frac{2}{\pi\Delta\omega_c} \cdot \frac{\Delta\omega_c^2}{4(\omega - \omega_c)^2 + \Delta\omega_c^2} \tag{2.6}$$

whereas the "free-space" mode density can be written as

$$\rho_0(\omega) = \frac{\omega^2 V n^3}{\pi^2 c^3} \tag{2.7}$$

V here is nomalized volume.

Therefore, from Eq. (2.2, 2.3, 2.4, 2.6, 2.7), we can estimate the enhancement of a QD's spontaneous emission rate γ by a WG mode as

$$\frac{\gamma}{\gamma_0} = \frac{3Q(\lambda_c/n)^3}{4\pi^2 V_{eff}} \, \frac{\Delta\omega_c^2}{4(\omega - \omega_c)^2 + \Delta\omega_c^2} \, \frac{|E(\boldsymbol{r})|^2}{|E_{\max}|^2} \, 2\,\eta^2 \tag{2.8}$$

γ_0 is the spontaneous emission rate of the QD in free space (without a cavity). ω is the QD emission wavelength. The first term in Eq. 2.8 is the Purcell factor F_p. The second and third terms describe the spectral and spatial matching between the QD and the WG mode. The factor of 2 comes from the two-fold degeneracy of the WG mode. $\eta = \boldsymbol{d} \cdot \boldsymbol{\epsilon}(\boldsymbol{r}) / |\boldsymbol{d}| \cdot |\boldsymbol{\epsilon}(\boldsymbol{r})|$ describes the orientation matching between the dipole of the QD and the polarization of the WG mode.

The Purcell factor F_p is only related to cavity properties (Q, V_{eff}). It indicates the maximum Purcell effect for an *ideal* emitter. This ideal emitter should be: 1) perfectly matched spectrally with the cavity mode $(\omega = \omega_c)$, 2) located at the maximum of the electric field, and 3) with its dipole aligned with the local electric filed. Note that F_p is for one of the resonant cavity modes alone. Despite a possibly large value of the Purcell factor, the spectral, spatial and orientation mismatches lead to significant reduction of the enhancement factor. Assuming uniform distribution of QDs in space and in spectrum, we estimate the average enhancement factor:

$$\left\langle \frac{\gamma}{\gamma_0} \right\rangle = F_p \left(\frac{1}{2\lambda_w} \int_{-\lambda_w}^{\lambda_w} \frac{\Delta\lambda_c^2}{4(\lambda - \lambda_c)^2 + \Delta\lambda_c^2} d\lambda \right) \left(\frac{1}{V} \int |\boldsymbol{f}(\boldsymbol{r})|^2 \, d^3\boldsymbol{r} \right) 2 \, \frac{1}{3} \tag{2.9}$$

λ_w is the full width at half maximum (FWHM) of the WG mode. For the experimental $TE_{13,2}$ mode, $F_p \sim 25$, and the average enhancement factor is estimated to be 3.4. It is close to the experimental value.

Since the spontaneous emission enhancement factor depends on the spectral and spatial overlap of the QD with the WG mode, each QD in the microdisk undergoes a specific spontaneous emission rate enhancement. Some QDs, with better spectral and spatial coupling with the WG mode, experience large enhancement of their spontaneous emission rates. Hence, the spontaneous emission rates for the coupled QDs have a distribution.

Compared to the average enhancement factor, a more accurate way of describing the spontaneous emission enhancement is to introduce a distribution function $P(\gamma)$ for the spontaneous emission rates γ. The temporal evolution of emission intensity $I(t)$ at the frequency of a WG mode can be written as:

$$I(t) = \int_0^\infty P(\gamma)\, e^{-\gamma t}\, d\gamma \tag{2.10}$$

where $P(\gamma)$ is normalized: $\int_0^\infty P(\gamma) d\gamma = 1$. We numerically solve the above integral equation 2.10 to retrieve $P(\gamma)$ from the measured $I(t)$. We use the truncated singular value decomposition to find the distribution with minimal L_2 normal $\int_0^\infty [P(\Gamma)]^2\, d\Gamma = 1$ [41–43]. The nonnegative constraint, $P(\Gamma) > 0$, is applied to the search for $P(\Gamma)$. The numerical solutions of $P(\gamma)$ are achieved with help of commercial program DYNALS.

Figure 2.6 shows the distributions of the spontaneous emission rates $P(\gamma)$ recovered from on-resonance and off-resonance PL decay curves $I(t)$. Curves A and B represent $P(\gamma)$ at the off-resonance wavelength of 978 nm under the incident pump intensities of 4.2×10^2 and 1.3×10^3 W/cm^2, respectively. Curves C, D, and E represent $P(\gamma)$ at the wavelength of $\mathrm{TE}_{13,2}$ mode under the incident pump intensities of 2.8×10^2, 4.2×10^2 and 1.3×10^3 W/cm^2, respectively. At the off-resonance wavelength, the distribution function is a narrow peak centered at ~ 2 GHz. The central decay rate corresponds to a decay time of ~ 500 ps. This value is close to the decay time obtained from the mono-exponential curve fitting of the non-resonance PL curves. At the wavelength of $\mathrm{TE}_{13,2}$ mode, $P(\gamma)$ has a long tail at the higher decay rate. This indicates the decay rates for some QDs are

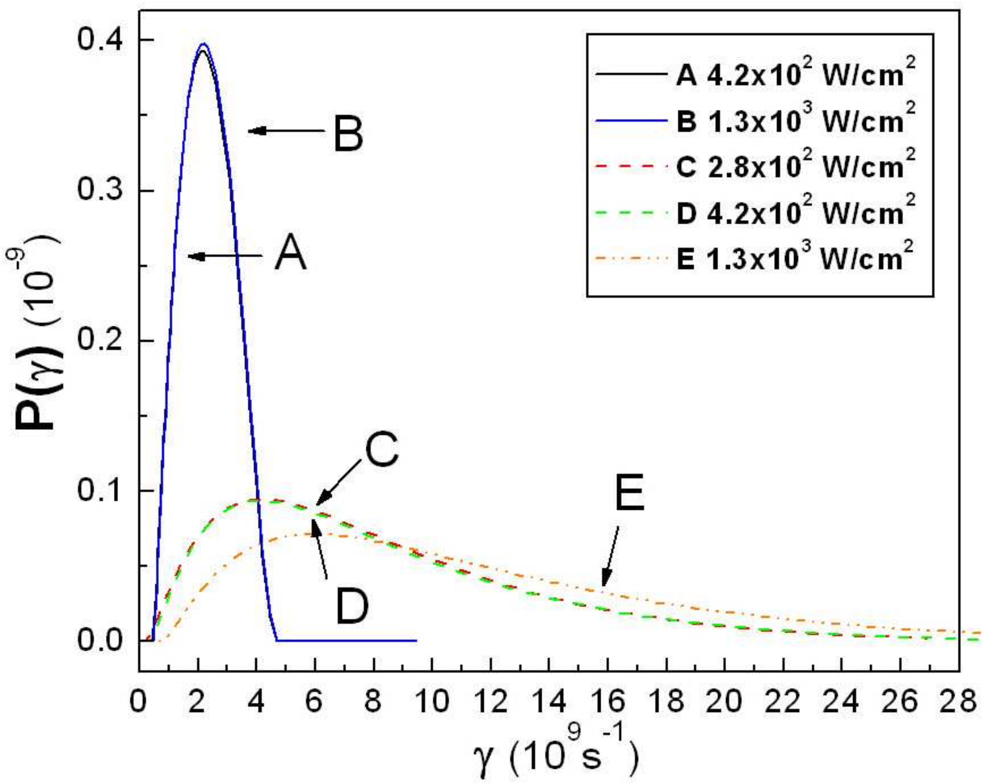

Figure 2.6: Distributions $P(\gamma)$ of decay rates γ extracted from the PL curves at the wavelengths 978 nm (A,B), and 973.5 nm (C,D,E). The incident pump intensities are (A) $4.2{\times}10^2$, (B) $1.3{\times}10^3$, (C) $2.8{\times}10^2$, (D) $4.2{\times}10^2$, and (E) $1.3{\times}10^3$ W/cm^2.

enhanced. The higher decay rates can result from the spontaneous emission enhancement or the stimulated emission. In the absence of stimulated emission, the decay rate distribution $P(\gamma)$ should be independent of the pump intensity. As shown in Fig. 3, the on-resonance decay rate distribution at the pump intensity of 4.2×10^2 W/cm^2 (curve D) is almost identical to that at 2.8×10^2 W/cm^2 (curve C). This confirms that curves C and D represent the distribution of spontaneous emission rates. In another word, the pump intensity of 4.2×10^2 W/cm^2 is low enough that the stimulated emission into $TE_{13,2}$ mode is negligible. According to curves C and D, the spontaneous emission rates for some QDs exceed 20 GHz. The corresponding decay time is less than 50 ps. Therefore, the spontaneous emission enhancement factor for some QDs exceed 10. When the pump intensity is increased to 1.3×10^3 W/cm^2, the on-resonance decay rate distribution changes. $P(\gamma)$ is extended further to higher decay rates. The change of $P(\gamma)$ illustrates the emergence of stimulated emission into $TE_{13,2}$ mode. Note that at the same pump intensity of 1.3×10^3 W/cm^2, the off-resonance decay rate distribution (curve B) remains identical to that at 4.2×10^2 W/cm^2 (curve A). This means stimulated emission does not exist in the off-resonance PL. Therefore, at the cavity resonant frequency stimulated emission emerges at much lower pump intensity, owing to the high Q of the WG mode.

An important issue in the measurement of the spontaneous emission enhancement by a microcavity is the elimination of stimulated emission. Some QDs have stronger coupling to the cavity mode, and stimulated emission could occur in them at a lower pumping intensity, where most QDs still spontaneously emit photons. Thus, it is difficult to estimate the pumping intensity when stimulated emission can be neglected for all the QDs. From the dependence of the decay rate distribution on the pumping intensity, we can identify the onset of stimulated emission for all the QDs, which thus eliminates the possibility of having stimulated emission in any QDs.

In summary, we have studied the enhancement of spontaneous emission rates for InAs QDs embedded in GaAs microdisks in a time-resolved PL experiment. Inhomogeneous broadening of the QD energy levels and random spatial distribution of the QDs in a microdisk lead to a broad distribution of the spontaneous emission rates. Using an efficient regularized method based on the truncated singular value decomposition and the non-negative constraints, we extract the distribution of spontaneous emission rates from the temporal decay of emission intensity. The maximum spontaneous emission enhancement factor exceeds 10.

CHAPTER 3

DYNAMICAL LOCALIZATION IN MICRODISK LASERS WITH ROUGH BOUNDARY

3.1 Ray dynamics in microdisks with rough boundaries

Due to their compact dimensions, long mode lifetime, and high versatility, semiconductor microdisk resonators are among the most suitable components for microlasers, microsensors, and micro-detectors [40, 44, 45]. The scientific and engineering aspects of these devices have therefore recently gained considerable attention [46, 47].

The mode structure of these *circular* microdisk resonators is usually associated with stable quasi-periodic whispering-gallery (WG) ray trajectories (Fig. 3.1(a)). Each such trajectory corresponds to a particular value of angular momentum, characterized by the (conserved) angle of incidence χ. This can be seen more clearly in Poincaré surface of section (SOS) phase space. Here we represent trajectory in terms of arc length of the position s and sine of angle of incidence χ, which is proportional to the angular momentum. As shown in Fig. 3.1(c), ray trajectory in a circular disk is a straight line in SOS. The corresponding resonant mode in the microdisk is called WG mode (Fig. 3.1(b), (d) is the corresponding phase space - Husimi distribution) as discussed in Chapter I. In the quasi-classic case – when the radius of the cavity R_0 is much larger

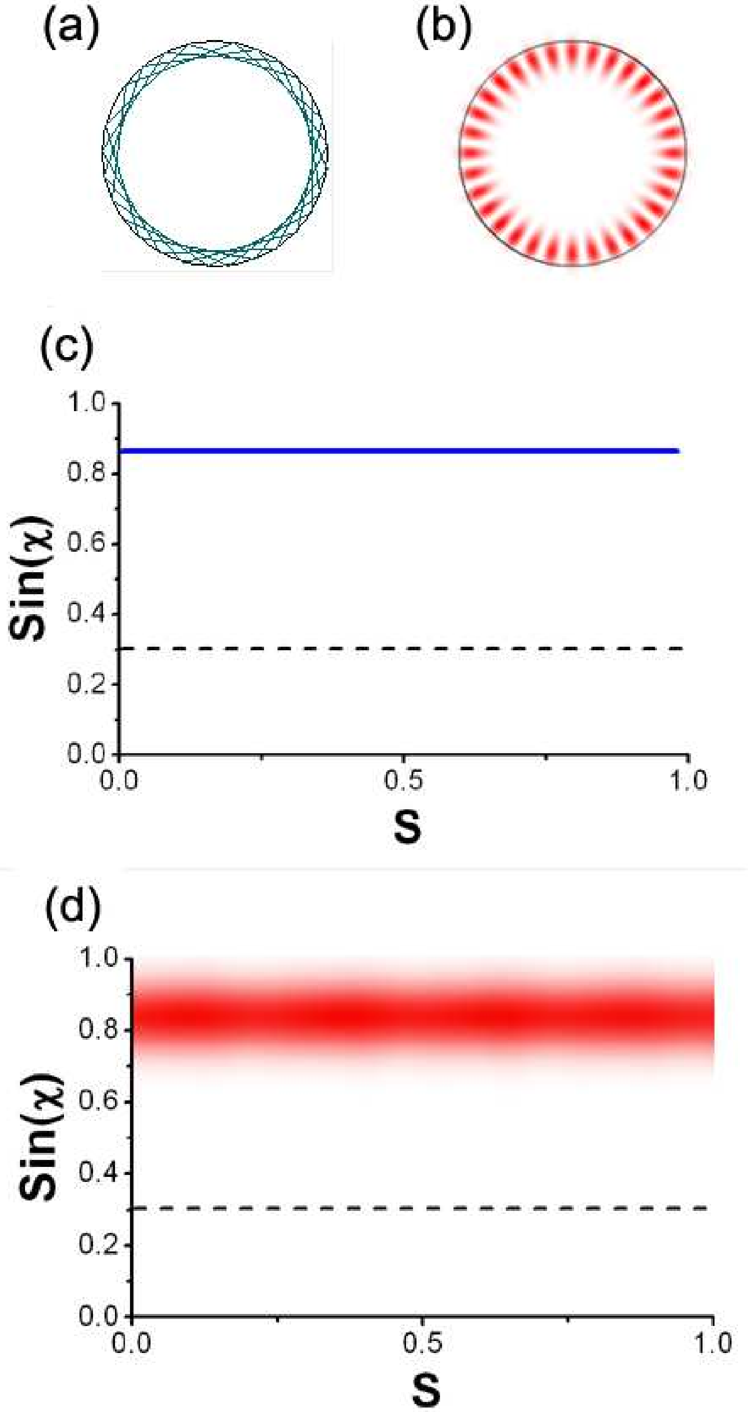

Figure 3.1: Classical ray trajectory in real space (a) and Poincaré SOS phase space (blue line in c) of a circular disk. (b) shows the corresponding resonant mode in real space, and (d) is the Husimi distribution of this mode. Black dash lines in (c) and (d) indicate the position of critical angle in phase space $sin(\chi) = 1/n$.

than the "internal" wavelength $\lambda = \lambda_0/n$ (n being the refraction index of the disk) – the modes of the system can be deduced from the regular trajectories via Einstein-Brillouin-Keller quantization scheme [48–50]. Since the trajectories with $sin(\chi) > 1/n$ are classically trapped inside the cavity, the finite lifetime of the corresponding modes of the optical resonator is attributed to diffraction loss through the curved boundary known as evanescent escape. Since such an escape corresponds to violation of classical (ray) dynamics, it is exponentially suppressed (as any tunneling process in wave-mechanical system), giving rise to the Q-factors up to 10^5 [38].

However, the above semiclassical ray-to-wave correspondence is based on the fact that the conserved angular momentum of the ray trajectory can be used as a "good mode number" for the wave-optical system, and thus is valid only for an ideal circular geometry. Any deviations from this ideal case – due to e.g. boundary roughness and surface defects, leading to light scattering (and correspondingly to change of the angular momentum of the trajectory), will inevitably break this idealized picture.

In particular, the symmetry of the resonator boundary is generally broken by the surface roughness, which is inevitable in the device fabrication. For example, the surface roughness may be transfered from mask, or introduced during lithography and etching process. Quantitatively, for a disk with short-range deformed boundary:

$$R(\phi) = R_0 + \sum_{l=1}^{M} \frac{1}{l} \left[a_l \, cos(l\phi) + b_l \, sin(l\phi) \right] \tag{3.1}$$

where $R_0 = \langle R(\phi) \rangle$ is the average of the radius and $M \gg 1$, the degree of roughness can be characterized by the parameter κ:

$$\kappa = \left\langle \left(\frac{dR}{d\phi} \right)^2 \right\rangle^{1/2} = \sqrt{M \frac{\langle a^2 \rangle + \langle b^2 \rangle}{2}} \tag{3.2}$$

Below the critical value of κ_c corresponding to the classical transition from integrability to chaos (whose value is not universal and depend on the functional form of the deformation $\delta R(\phi) \equiv R(\phi) - R_0$), the ray trajectories inside the cavity remain quasi-regular (Fig. 3.2 (b)) and are still trapped inside by the total internal reflection. In this case, the mode patterns and lifetimes can be obtained using adiabatic approach [48, 51] assuming that the high-Q modes of the asymmetric resonator adiabatically evolve from the original WG modes of the circular resonator.

In contrast to this behavior, for $\kappa > \kappa_c$ the ray dynamics inside the cavity becomes completely chaotic, and no classical orbits are trapped inside the cavity (Fig. 3.2(c)).

Nevertheless, when we go back to the wave optics problem, the high-Q modes can exist in the cavity even in the case $\kappa > \kappa_c$. The physical reasons behind this seeming inconsistency strongly depend on the relation between the size of the cavity and the wavelength of light inside the system. Namely, when the deviations from the idealized geometry are substantially smaller than the wavelength, they only lead to a small change in the mode patterns and lifetimes which can be calculated using perturbation theory. In this regime the high-Q modes preserve their "whispering-gallery nature", regardless of the nature of the resulting ray dynamics in the "rough" resonator. Quantitatively [52],

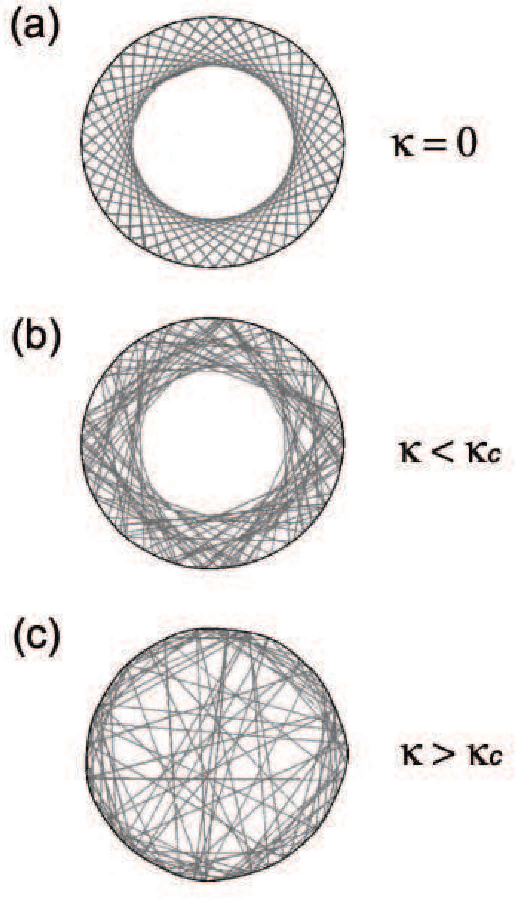

Figure 3.2: The typical ray trajectory in circular (a) and rough (b, c) resonators. The resonator geometry in (b) corresponds to the adiabatic regime ($\kappa \approx 0.06$), the geometry in (c) corresponds to the device studied in our experiments ($\kappa \approx 0.2$).

in rough resonators, the perturbative regime is observed when

$$\kappa \ll \lambda/R_0 \tag{3.3}$$

Many earlier experiments, including the pioneering work of McCall *et al* [3], probed this regime.

In contrast to this behavior, when the requirement (3.3) is violated and $\kappa \geq \lambda/R_0$, the (chaotic) nature of the underlying ray dynamics does strongly affect the modes of the resonator. The famous "Berry's conjecture" [53] then implies that the modes follow the random patterns formed by chaotic ray trajectories, and behave essentially similar to random superpositions of plane waves. As Berry's conjecture has been extensively tested for various geometries [54], one may be strongly tempted to conclude that high-Q modes in microdisk resonators can only be found for small roughness when $\kappa < \max\left[\lambda/R_0, \kappa_c\right]$ – which implies severe limitations on the fabrication tolerance of the final device performance.

However, in the mechanism known as dynamical Anderson localization (DL) [55–59], the destructive interference of the scattered light may lead to suppression of the chaotic scattering and to the formation of the modes strongly localized in the phase space. In particular, it was shown that in "rough billiards" dynamical localization may lead to exponential localization of modes in the angular momentum space [52, 60].

Although the refractive and evanescent escape from the dielectric microdisk resonator make it a different dynamical system from a point particle in a billiard with ideal reflective

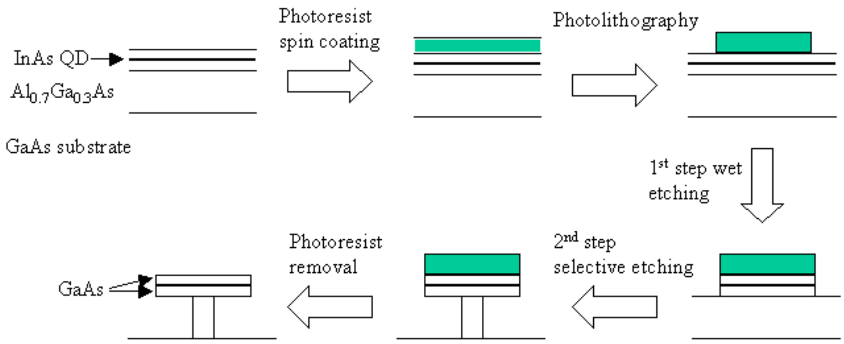

Figure 3.3: The microdisks are fabricated by photolithography and two-step wet etching.

walls, the quasi-stationary states of the electromagnetic field in a rough optical resonator retain the dynamical localized nature which shows up in the log-normal distribution of their lifetimes [61]. By virtue of its "heavy tail" for large lifetimes, the log-normal distribution implies the existence of high-Q modes even in a microdisk resonator with strong boundary roughness. Lasing in one of these modes would therefore be a direct evidence of dynamical localization.

Below, we present our study of lasing behavior from high-Q modes of semiconductor microdisks with rough boundary. In section 2, we describe the details of our experimental setup and measurement results. And section 3 is is devoted to theoretical simulations. We calculate the quasi-stationary states in our microdisk devices, and directly show the exponential localization of lasing modes in the angular momentum. By comparing the theoretical mode patterns with the experimental data obtained by direct optical imaging, we identify the lasing mode and confirm its dynamically localized structure.

3.2 Lasing in rough microdisks

Our dielectric microlaser is made of 200 nm thick GaAs layer with a thin InAs quantum well in the middle. The microdisks (with the typical diameter close to 5μm) are fabricated by photolithography and two-step wet etching as shown in Fig. 3.3 (see Chapter 2 for more detail). To isolate the disks from the GaAs substrate, each disk is supported by a 500nm-long AlGaAs pedestal. As the etching process is not exactly isotropic, the shapes of the disk deviate from an ideal circle. Figure 3.4 shows the scanning electron microscope (SEM) images of a typical disk – note the roughness at the disk boundary revealed in the magnified image (left panel).

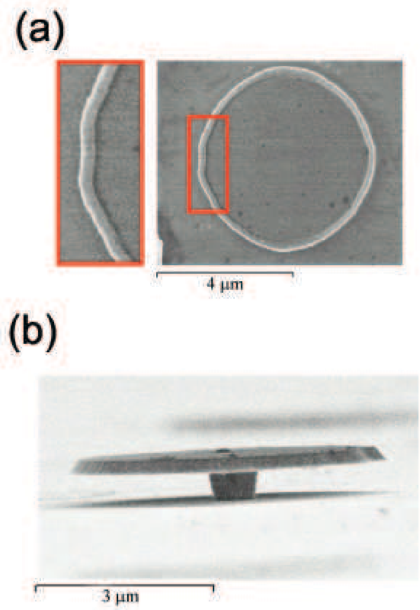

Figure 3.4: Top (a) and side (b) view SEM images of a GaAs microdisk on an $Al_{0.7}Ga_{0.3}$ pedestal.

The lasing experiment is performed on individual disks. Experimental setup is shown in Fig. 3.5. The microdisks are mounted in a low temperature cryostat, and cooled down to 10K. The InAs quantum well is optically excited by a mode locked Ti-sapphire laser at 790 nm. The pump beam is focused by an objective lens onto a single disk. The emission from the disk is collected by the same lens, and sent to a 0.5-meter spectrometer with a liquid nitrogen cooled charge coupled device (CCD) array detector. Figures 3.6 - 3.9 are the data of the measurement of the disk in Fig. 3.4. As shown in Fig. 3.6(a), the emission spectrum features a broadband amplified spontaneous emission (ASE) and several distinct peaks that correspond to the cavity modes. Figure 3.6(b) is a plot of the intensity and linewidth of one mode at λ_0=855.5nm as a function of the incident pump power. When the pump power exceeds a threshold, the emission intensity exhibits a sudden increase accompanied by a simultaneous decrease of the mode linewidth. This threshold behavior corresponds to the onset of lasing oscillation in this mode. At high pumping levels, lasing may occur in several cavity modes.

To find out the spatial profile of the lasing mode, we use a bandpass filter of 1nm width to single out the mode at 855.5nm (Fig. 3.5). The filtered spectrum obtained in this measurement, is shown in Fig. 3.7 as the blue solid curve. The spatial distribution of the mode intensity on the disk surface is projected onto a digital CCD camera by the objective lens. As shown in the inset I of Fig. 3.7, the near-field image of the lasing mode reveals its intensity is concentrated near the disk edge. Thus, the lasing mode is similar to a whispering-gallery mode, despite of the boundary roughness. We extract the spatial intensity distribution $I(r, \phi)$ from the digital image, and calculate the radial distribution

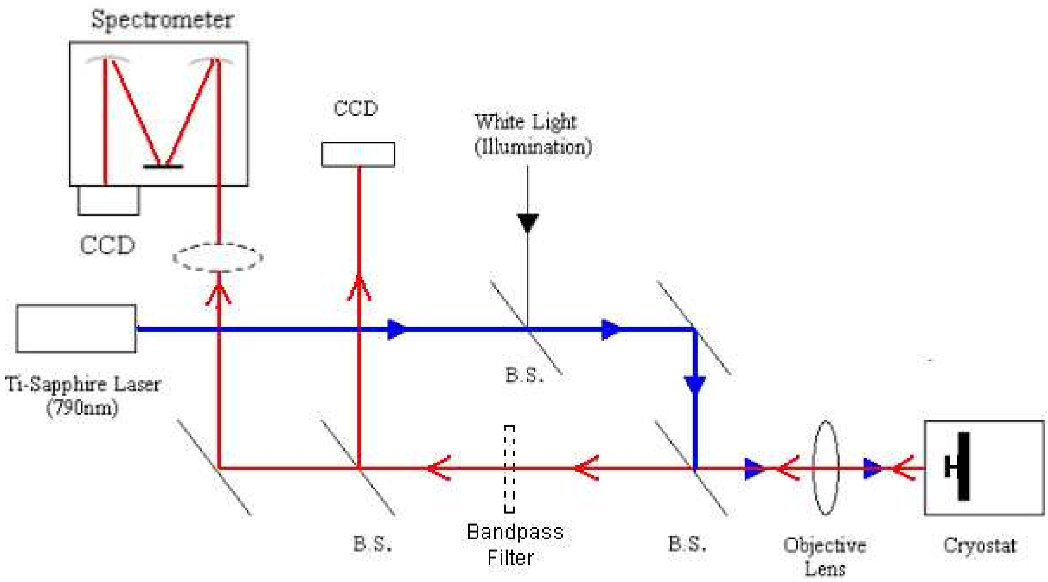

Figure 3.5: Optical measurement setup

by integrating over the angle:

$$I_r(r) = \frac{1}{2\pi} \int_0^{2\pi} I(r, \phi) d\phi \tag{3.4}$$

The data for $I_r(r)$ at several pump powers are shown in Fig. 3.8(a). Well below the lasing threshold, $I_r(r)$ represents the radial distribution of spontaneous emission, which is nearly constant across the disk. When the pump power approaches the lasing threshold, the contribution of the lasing mode gradually dominates the radial intensity distribution. The intensity near the disk boundary grows much faster than that in the disk center. This change in the intensity profile coincides with the rapid increase of the lasing mode intensity in the emission spectrum. An intensity maximum is developed close to the disk boundary. To confirm that the intensity maximum comes from the lasing mode, we

(a)

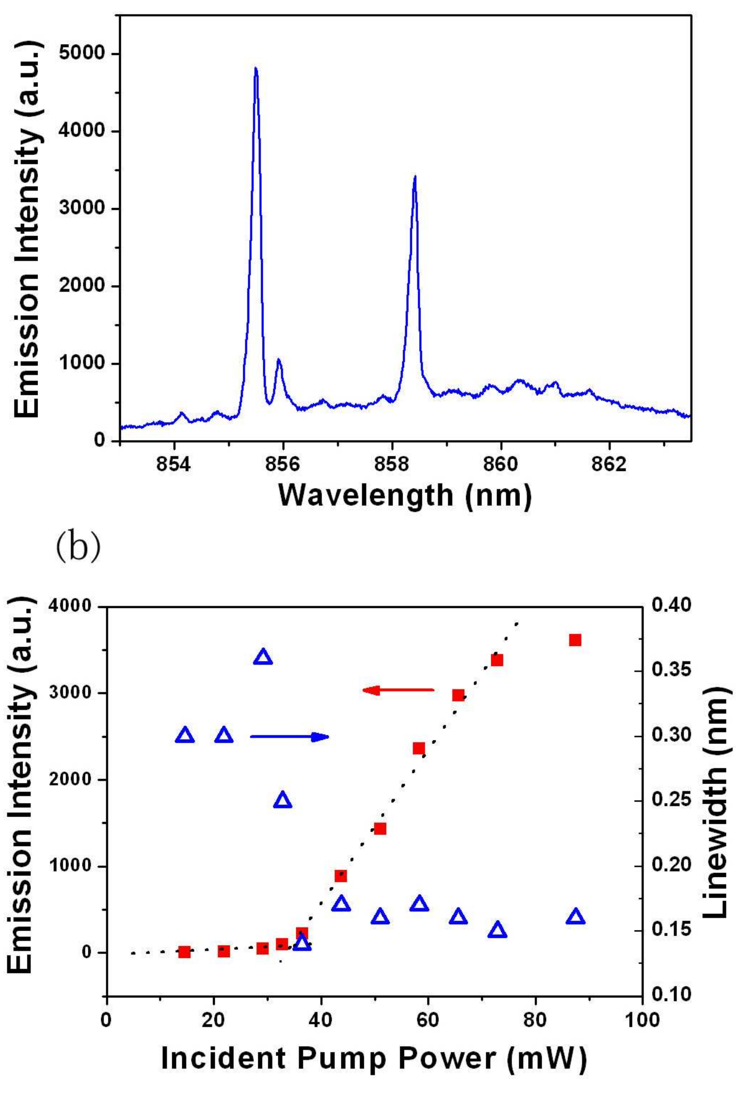

Figure 3.6: (a) Spectrum of emission from the GaAs microdisk shown in Fig. 3.4. The incident pump power is 44μW. (b) The emission intensity and linewidth of the mode at 855.5nm as a function of the incident pump power.

measure the spatial distribution of the amplified spontaneous emission at the same pump power – which is obtained when the frequency of the bandpass filter is tuned away from any cavity resonance. The dashed curve in Fig. 3.7 shows the filtered spectrum of the ASE alone. The inset II of Fig. 3.7 is the corresponding near-field image. It reveals a virtually uniform distribution of the amplified spontaneous emission across the disk. The radial distribution of ASE intensity, plotted as the dashed line in Fig. 3.8(b), is nearly independent of r. The dramatic difference in the spatial distribution of the laser emission and the ASE indicates that the lasing mode is localized near the disk boundary.

We also measure the spectra of emission from different parts of a microdisk. We use an lens (as shown in Fig. 3.5, the lens is added in front of spectrometer) to project a magnified image of the microdisk onto the entrance slit of an imaging spectrometer. The magnification is about 400 times, thus the disk image is about 2mm in diameter. We first fully open the entrance slit and rotate the grating to the position of the zeroth order diffraction (i.e., reflection). The spectrometer projects the image at the plane of the entrance slit onto the two-dimensional ($2D$) CCD array detector mounted at the exit port. After aligning the disk image to the center of the entrance slit, we reduce the width of the entrance slit to 0.1 mm. Now only the emission from a narrow strip along the vertical diameter of the disk can enter the spectrometer. The grating is rotated back to the position of the first-order diffraction, so that the light at different wavelength is dispersed in the horizontal direction. The CCD array detector, located at the image plane of the entrance slit, captures a 2D spatial-spectral image of the microdisk emission.

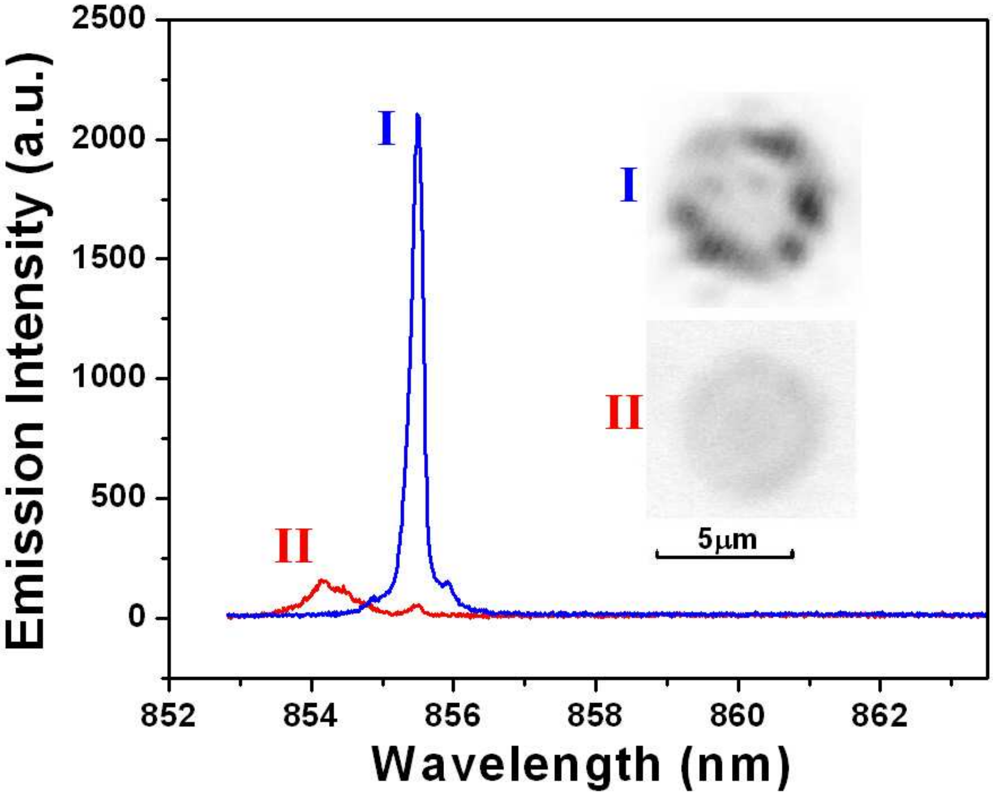

Figure 3.7: The blue curve I and the inset I are the spectrum and near-field image taken when the bandpass filter is tuned to the mode at 855.5nm. The red curve II and the inset II are the spectrum and image taken when the bandpass filter is tuned away from any cavity resonance. The incident pump power is 44μW.

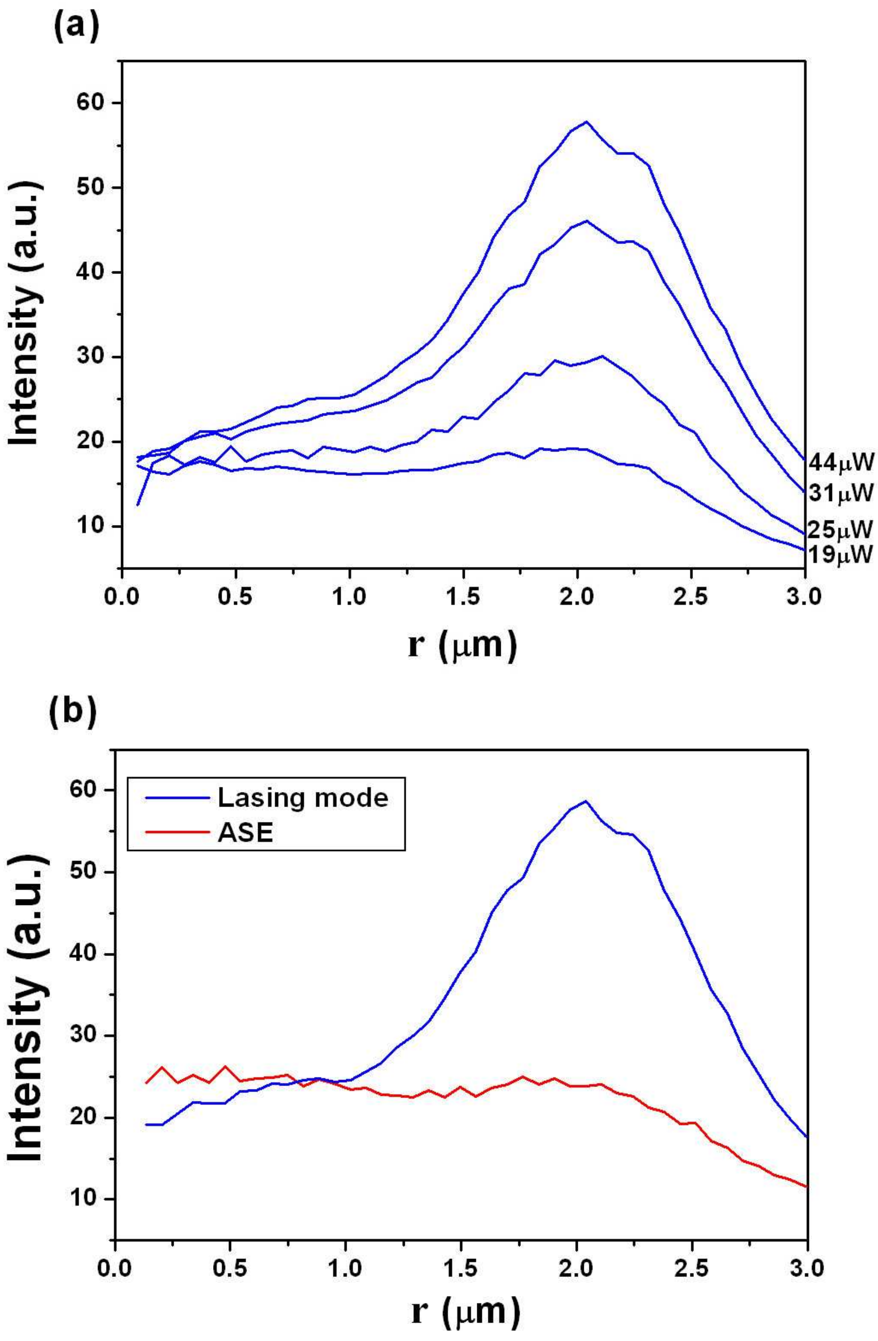

Figure 3.8: (a) Radial distribution of the emission intensity when the bandpass filter is tuned to the mode at 855.5nm. The incident pump powers are marked next to the curves. (b) The blue (red) curve represents the radial distribution of the laser emission (or amplified spontaneous emission) intensity obtained from the inset I (II) in Fig. 3.7.

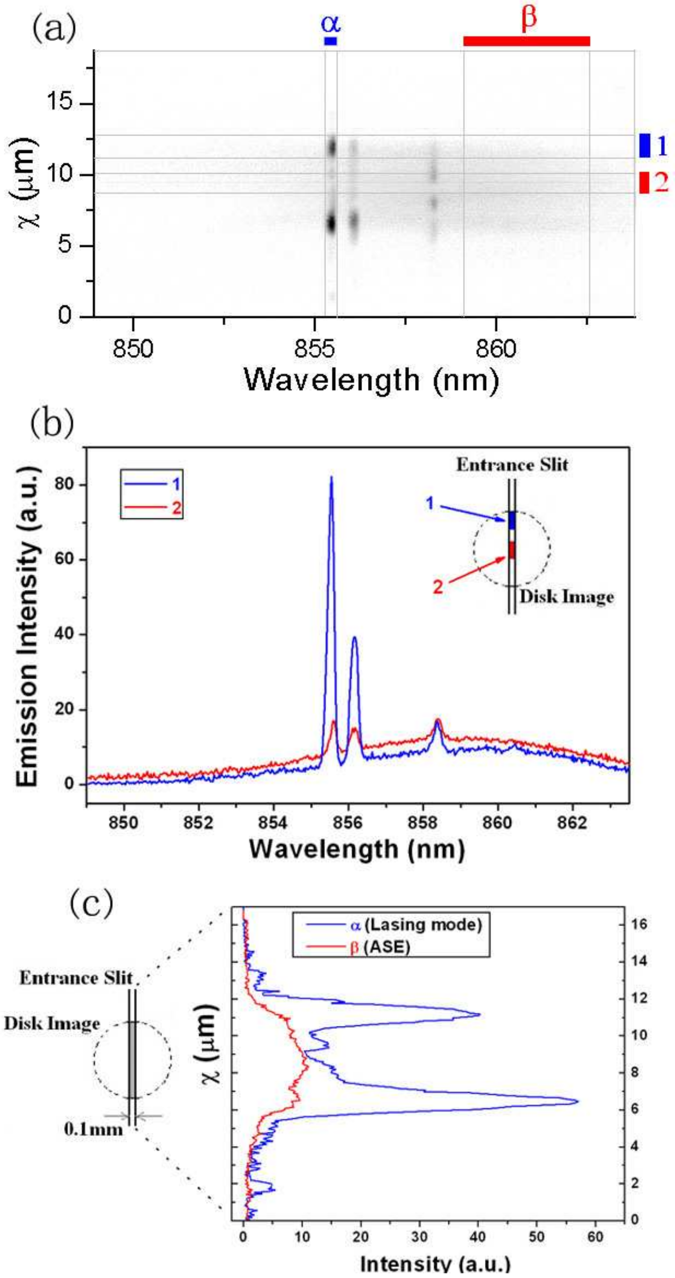

Figure 3.9: (a) Two-dimensional spatial-spectral image of the emission from the microdisk in Fig. 3.4. The incident pump power is 44μW. (b) Blue (red) curve is the spectrum of emission collected from the edge (center) part of the disk, corresponding to the horizontal strip marked by 1 (2) in (a). (c) Blue (red) line represents the emission intensity distribution across the disk diameter inside the vertical strip marked by α (β) in (a).

The resulting "local" spectral data are presented in Fig. 3.9. In the panel (a), each dark vertical line in the 2D image corresponds to a cavity mode. Because the vertical coordinate in Fig. 3.9(a) represents the spatial location on the disk, we can obtain the emission spectra from different parts of the disk by dividing the 2D image into many horizontal strips. In particular, the horizontal strip marked by 1 corresponds to the disk edge, while the strip marked by 2 is close to the disk center. The emission spectra, obtained by integrating over the spatial coordinate inside the strips 1 and 2, are shown in Fig. 3.9(b). In the spectrum of emission collected from the disk edge, the lasing peak at 855.5nm is much higher than the ASE background. But in the spectrum of emission taken from the disk center, the peak at 855.5nm is much weaker, although the ASE is a little stronger. Similarly, by dividing the 2D images into vertical strips and integrating over the spectral coordinate inside the strips, we can obtain the spatial distribution of emission intensity in any frequency range. For example, the vertical strip marked by α is centered at 855.5nm and has a width of 0.5 nm. It gives the spatial variation of the lasing mode intensity across the vertical diameter of the disk [Fig. 3.9(c)]. The lasing mode is peaked near the two ends of the disk. The vertical strip marked by β covers a frequency range that has only ASE. It gives the spatial distribution of the ASE intensity which is nearly constant across the disk diameter.

The above experimental data clearly show that in this 5 μm disk with rough boundary, the lasing mode at 855.5nm has WG-like structure – its intensity near the disk boundary is much stronger than that at the disk center. We have repeated the above measurements with many lasing modes in different microdisks, and similar results are obtained.

3.3 Dynamical localization of a lasing mode

To understand the dynamics inside the micro-resonator, it is necessary to consider the system behavior in the phase (coordinate – momentum) space. We depict the classical dynamics of the system via Poincaré surface of section (SOS).

If the system has circular symmetry, the angular momentum $m\hbar$ of any trajectory is conserved, where $m = 2\pi nR/\lambda_0$ [49]. Correspondingly, each trajectory follows a $1D$ horizontal line in SOS (Fig. 3.1). The line $sin(\chi) = 1/n$ effectively separates the SOS into two parts. The trajectories which fall below this line can refractively escape from the system. The ones above the "critical line" are classically trapped inside by the total internal reflection. The corresponding modes of wave-dynamical system are allowed to escape the cavity only through exponentially suppressed evanescent leakage, thus have extremely high Q-factors [62].

Introduction of the boundary roughness dramatically changes the ray dynamics inside the system. Thus the stability of all WG trajectories inside the experimental device described in the previous section (corresponding to $\kappa \approx 0.2$) is completely destroyed (see Fig. 3.10). Furthermore, in the absence of circular symmetry, the angular momentum is no longer a conserved quantity, and the system becomes classically chaotic. As the ray propagates through such a cavity, its angular momentum undergoes the diffusive motion.

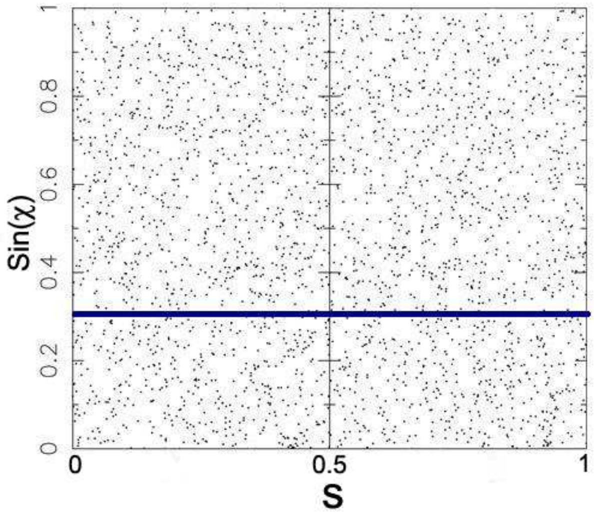

Figure 3.10: Poincaré surface of section (SOS) in the microdisk of rough boundary shown in Fig. 3.4. Note the chaotic dynamics in the fabricated microcavity.

No ray is now trapped above the "critical line", which seemingly leads to the absence of high-Q modes.

However, the classical angular-momentum diffusion of the initially close ray trajectories may be suppressed by a destructive interference in wave-dynamical system. Such an effect is known as dynamical localization, which in some sense similar to Anderson localization of electrons in disordered potential; however, while the later takes place in the real (coordinate) space, the former takes place in the phase (momentum) space and is thus related to the system "propagation" (dynamics). The dynamical localization, initially introduced for a quantum analog of classically chaotic kicked-rotator [55], was later mapped onto the dynamics of quantum billiards [52] and semiclassical optical microcavities [61].

To confirm that the experimental lasing mode is in fact dynamically localized, we use the SEM image of the microdisk (Fig. 3.4) to digitize its shape and numerically analyze its behavior. To numerically simulate the electromagnetic field distribution, we use a generalization to open systems of the *scattering quantization approach* to quantum billiard [66], originally introduced in ref. [65], and adopted for optical resonators in Ref. [61]. This approach is based on the observation that every quantum billiard interior problem can be viewed as a scattering problem. In the case of closed systems, the internal scattering problem can be mapped rigorously to an external scattering problem, and resulting scattering matrix is unitary. For the dielectric resonator problem with radiation boundary conditions, we will see that the corresponding scattering operator is inherently non-unitary, reflecting the physical fact of energy leakage.

In $2D$ system, Maxwell's equations can be reduced to Helmholtz equation for the scalarfield ψ with continuity conditions on the boundary ∂D:

$$(\nabla^2 + n_i^2 k^2)\psi_i(x, y) = 0 \tag{3.5}$$

$$\psi_1|_{\partial D} = \psi_2|_{\partial D},\ \frac{\partial \psi_1}{\partial v}|_{\partial D} = \frac{\partial \psi_2}{\partial v}|_{\partial D} \tag{3.6}$$

where $\frac{\partial}{\partial v}$ is normal derivative.

We assume the boundary $R(\phi)$ is some smooth deformation such that there exists only one point of the boundary for each angle ϕ. We decompose the internal and external fields into cylindrical harmonics

$$\psi_1(r,\phi) = \sum_{m=-\infty}^{\infty} (\alpha_m H_m^+(nkr) + \beta_m H_m^-(nkr))e^{im\phi} \qquad r < R(\phi) \tag{3.7}$$

$$\psi_2(r,\phi) = \sum_{m=-\infty}^{\infty} (\gamma_m H_m^+(kr) + \delta_m H_m^-(kr))e^{im\phi} \qquad r > R(\phi) \tag{3.8}$$

Here $H^{\pm}$ are the Hankel functions of the first and second kind. For a quasi-bound mode, it is safe to assume that there is no incoming waves in the external field, so that $\delta_m = 0$. The continuity conditions Eq. 3.6 give us further relations among the remaining coefficients:

$$\psi_1(\phi, R(\phi)) = \psi_2(\phi, R(\phi)) \tag{3.9}$$

$$\frac{\partial \psi_1}{\partial r}|_{\phi,R(\phi)} = \frac{\partial \psi_2}{\partial r}|_{\phi,R(\phi)} \tag{3.10}$$

These conditions can be written out as

$$\sum_{m=-\infty}^{\infty} (\alpha_m H_m^+(nkR(\phi)) + \beta_m H_m^-(nkR(\phi)))e^{im\phi} = \sum_{m=-\infty}^{\infty} \gamma_m H_m^+(kR(\phi))e^{im\phi} \tag{3.11}$$

$$n\sum_{m=-\infty}^{\infty} (\alpha_m H_m^{+'}(nkR(\phi)) + \beta_m H_m^{-'}(nkR(\phi)))e^{im\phi} = \sum_{m=-\infty}^{\infty} \gamma_m H_m^{+'}(kR(\phi))e^{im\phi} \tag{3.12}$$

By multiplying both sides by $e^{-in\phi}$ and integrating with respect to ϕ, we get a matrix equation for the coefficient vectors $|\alpha\rangle$, $|\beta\rangle$ and $|\gamma\rangle$

$$\mathcal{H}_1^+ |\alpha\rangle + \mathcal{H}_1^- |\beta\rangle = \mathcal{H}_2^+ |\gamma\rangle \tag{3.13}$$

$$\mathcal{DH}_1^+ |\alpha\rangle + \mathcal{DH}_1^- |\beta\rangle = \frac{1}{n}\mathcal{DH}_2^+ |\gamma\rangle \tag{3.14}$$

and the matrices are defined by

$$\left[\mathcal{H}_j^\pm\right]_{lm} = \int_0^{2\pi} d\phi\, H_m^\pm(n_j kR(\phi))e^{i(m-l)\phi} \tag{3.15}$$

$$\left[\mathcal{DH}_j^\pm\right]_{lm} = \int_0^{2\pi} d\phi\, H_m^{\pm\prime}(n_j kR(\phi))e^{i(m-l)\phi} \tag{3.16}$$

Eliminating $|\gamma\rangle$, we obtain

$$\mathcal{S}(k)\,|\alpha\rangle = |\beta\rangle \tag{3.17}$$

where the matrix $\mathcal{S}(k)$ is given by

$$\mathcal{S}(k) = \left[n(\mathcal{DH}_2^+)^{-1}\mathcal{DH}_1^- - (\mathcal{H}_2^+)^{-1}\mathcal{H}_1^-\right]^{-1}\left[(\mathcal{H}_2^+)^{-1}\mathcal{H}_1^+ - n(\mathcal{DH}_2^+)^{-1}\mathcal{DH}_1^+\right] \tag{3.18}$$

In the interior expansion Eq. 3.7, the regularity of the solution at the origin requires that $|\alpha\rangle = |\beta\rangle$. This provides us the quantization condition, considering the eigenvalue problem of $\mathcal{S}(k)$

$$\mathcal{S}(k)\,|\alpha\rangle = e^{i\varphi}\,|\alpha\rangle \tag{3.19}$$

where φ is a function of complex k_q, and satisfies $\varphi(k_q) = q\cdot 2\pi,\ q = 0, \pm1, \pm2, \cdots$.

The real part of k_q gives us the resonant frequency, while the imaginary part of k_q gives resonance width, which is related to resonant mode quality. By solving the quantization condition, we can get the quantized eigenvalues and eigenvectors $\left\{k_q, \left|\alpha^{(q)}\right\rangle\right\}$, so that we can construct the resonant solutions of the interior and exterior problem. Details can be found in Ref. [66].

With the boundary profile of the rough disk and S-matrix method, we are able to calculate the resonant modes in such cavity and identify the lasing mode in experiment, as shown in Fig. 3.11 (a). A direct comparison of the simulated and experimental measurement is not possible due to the finite spatial resolution of the optical imaging setup. Instead we compare the angle-averaged intensity distribution without any fitting parameters. Figure 3.11 (c) shows that our numerical simulations well reproduce the experimental data. The constant ASE background is subtracted from the measured intensity distribution at the lasing frequency.

It reveals that the real space structure of the simulated mode in Fig. 3.11 (a) somewhat resembles the WG mode of regular (circular) resonator. Thus, similarly to the standard WG modes most of the mode intensity is localized in an annular region along the boundary. However, as opposed to the standard WG patterns (Fig. 3.1(b)), inside the annulus the mode of the rough resonator shows strong and irregular intensity fluctuations. Furthermore, while any WG wavefunction corresponds to some definite value of the angular momentum, this mode shows the exponential distribution of different angular

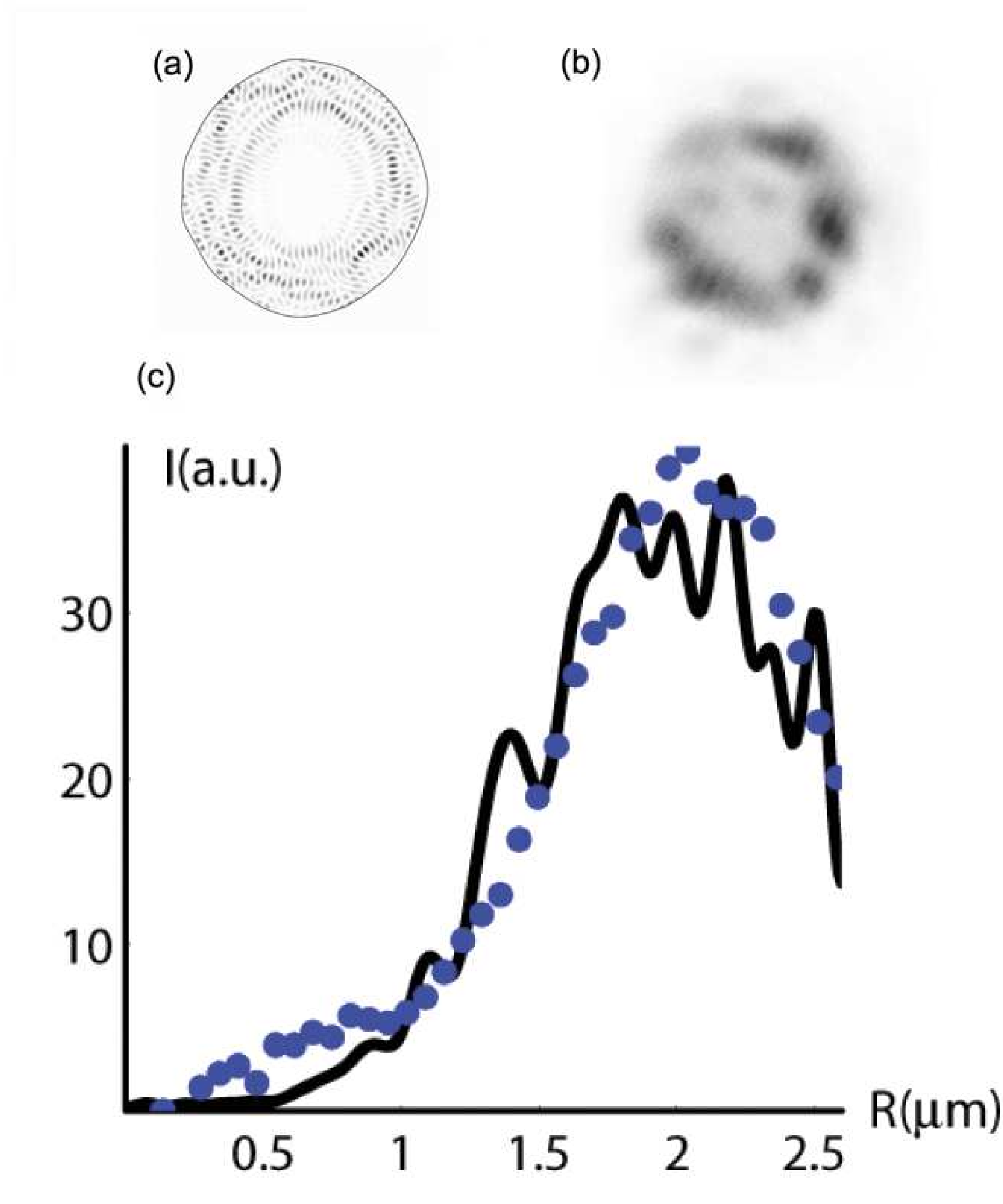

Figure 3.11: (a) Mode pattern of numerical simulation, and (b) experimental image. (c) Radial intensity distribution of simulated mode shown in (a) (black curve), and intensity of the experimental lasing in (b) with subtracted constant amplified spontaneous emission background (blue dots).

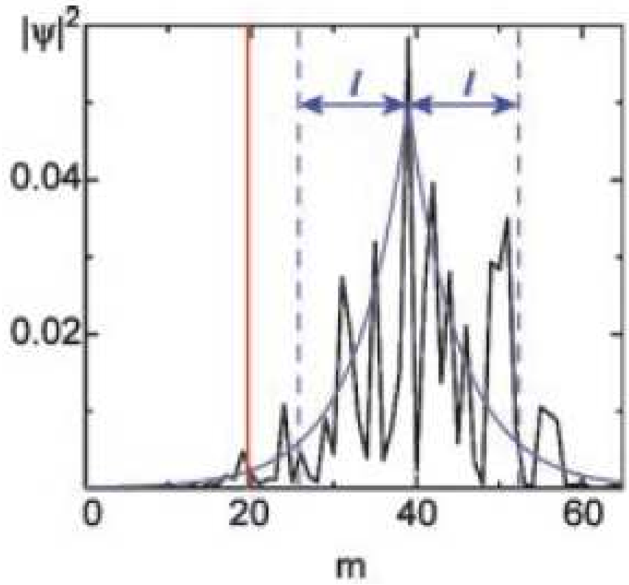

Figure 3.12: The angular-momentum distribution of the lasing mode obtained from our numerical simulations. $l \approx 12.4$ is the localization length. The red solid line corresponding to critical angle $sin(\chi_c) = 1/n$.

momentum components ψ_m, localized near some central angular momentum value m_0:

$$\psi_m \propto \exp\left(-\frac{|m - m_0|}{l}\right), \tag{3.20}$$

where the parameter l, which defines the localization length (in the unit of angular momentum/$\hbar$) is related to roughness parameter κ. Specifically, beyond the perturbative regime, i.e. when the condition in Eq. (3.3) is violated, $l \propto (nkR_0\kappa)^2$ with $k = 2\pi/\lambda_0$ [52]. As shown in Fig. 3.12, $l \approx 12.4$ is obtained for the lasing mode in our simulation, which indicates a clear evidence of the dynamical localization. Note that since DL as any statistical process is often accompanied by strong fluctuations [52, 63, 64], the Eq. (3.20) describes the envelope of the mode in the angular momentum representation.

Since the escape from the resonator is dominated by a portion of the mode having angular momenta below the critical value $m_c = nkR_0 sin(\chi_c)$, the quality parameter of the mode can be approximated using $Q \approx 1/\psi_{m_c}^2 \propto \exp\left[2(m_0 - kR_0)/l\right]$ [61]. Therefore, the dynamically localized mode with m_0 sufficiently above the critical line and small (in comparison with kR_0) localization length, may have relatively long lifetime, and can be used in all resonance-based systems (lasers, sensors, etc.). In our case, the theoretical value of the Q-factor for the lasing mode is 4.7×10^3.

When the localization length [52] $l \propto (\kappa nkR_0)^2$ becomes of the order of nkR_0, the escape from the resonator is no longer strongly suppressed by dynamical localization, and the system no longer supports high-Q whispering-gallery modes – which sets an upper bound for the roughness for an optical microdisk resonator

$$\kappa \ll 1/\sqrt{nkR_0} \tag{3.21}$$

Note that in the semiclassical regime ($kR_0 \gg 1$) this criterion is much less stringent than the perturbative border (3.3).

In conclusion, we have studied the effect of boundary roughness on the lasing modes in semiconductor microdisks. Despite classically chaotic ray dynamics, our experiments show lasing with decent threshold. We have demonstrated that the lasing modes in our devices originate from dynamical Anderson localization. Our results demonstrate that the microdisk resonators based on DL modes have a significant fabrication tolerance advantage over their "regular" counterparts.

CHAPTER 4

SEMICONDUCTOR ICRO-STADIUM LASERS

4.1 Open chaotic microcavities

Microlasers are essential components of integrated photonic circuits. To reduce power consumption, low lasing threshold is desired, which can be realized with microcavities of high quality factor Q. Among the various types of semiconductor microlasers that have been developed over the past two decades, microdisk lasers have the highest quality factors. This is because light is confined in circular dielectric disks by total internal reflection, and the only escape channel for light is evanescent tunneling whose rate is extremely small. The major drawback of microdisk lasers is undirectional (isotropic) output. To overcome this problem, deformation of the disk shape from circle was proposed [51]. Directional laser output was observed in asymmetric resonant cavities of quadrupolar deformation [67, 68]. Another type of deformed cavity is Bunimovich's stadium which consists of two half circles connected by two straight segments. Different from a quadrupolar billiard, ray mechanics in a stadium billiard exhibits "full chaos", i.e., there exist no stable periodic orbits (Fig. 4.1). However, a dense set of unstable periodic orbits (UPOs) are still embedded in the chaotic orbits. Although the UPOs are found with zero probability in the classical dynamics, in wave mechanics they manifest themselves in the eigenstates of the system. There exist extra and unexpected concentrations, so-called *scars*, of eigenstate density near UPOs [69]. Lasing has been realized in both scar modes and chaotic modes of dielectric stadium with certain aspect ratio [70,71]. Highly directional output of laser emission was predicted [72] and confirmed in polymer stadiums [73]. However, it is not known how the lasing modes would change when the aspect ratio of the stadium is varied gradually. When optical gain is not high and uniformly distributed across the cavity, the lasing modes are typically the cavity modes of high quality factor Q. Thus it is important to find out what the high-quality modes are in the stadium cavities, and how their Q values depend on the cavity shape.

From the fundamental physics point of view, a two-dimensional (2D) stadium billiard is a well-known model for classical and quantum chaos. There have been detailed studies of the eigenmodes in closed stadium billiards, e.g., a microwave cavity where ray cannot escape [54,69,74–78]. Even in the studies of conductance (transmission) through an open stadium billiard, only a few leads are attached to the stadium boundary through which ray can escape [79]. A dielectric stadium is very different in the sense that its entire boundary is open so that refractive escape and tunneling escape of light could happen at any point on the boundary. In terms of wave mechanics, the eigen-energies of a dielectric stadium cavity are complex numbers whose imaginary parts reflect the lifetimes of the eigen-modes. It is not clear whether the eigen-modes of a dielectric stadium can have long lifetime, thus low lasing threshold. And if so what the physical mechanism for the formation of long-lived modes is.

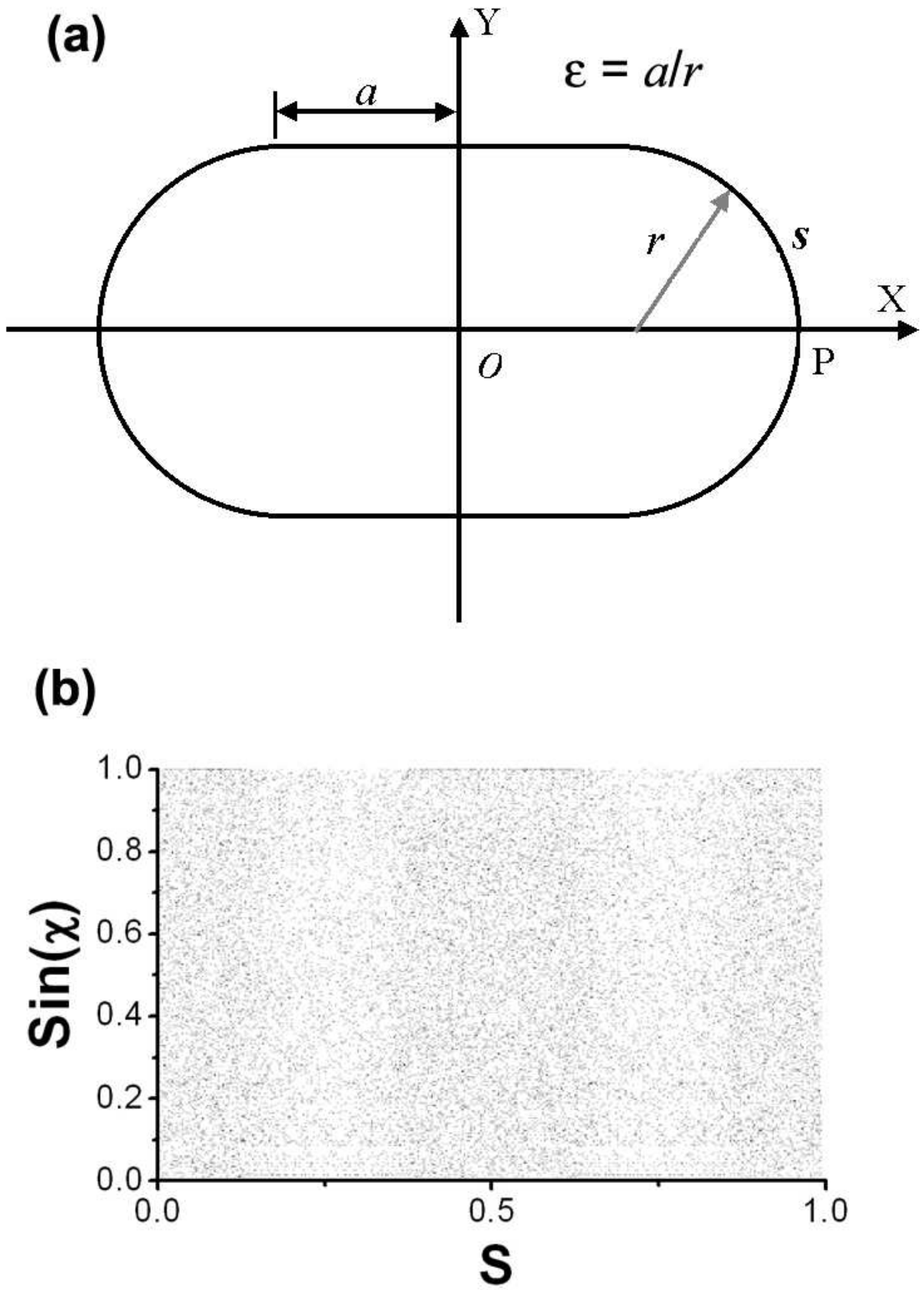

Figure 4.1: (a) Structure of a stadium billiard. The deformation of the stadium is defined as $\epsilon = a/r$. (b) Poincaré SOS of a stadium with $\epsilon = 1.0$.

In this Chapter, we show our numerical simulations of high-Q modes in dielectric stadiums [80], followed by our experimental studies of semiconductor microstadium lasers [81]. We find for stadium with large deformations, high-Q modes are usually scar modes consists of several UPOs. The interference of partial waves propagating along the different orbits may minimize light leakage at certain deformation. Thus by tailoring the stadium shape, we are able to achieve optimum light confinement in a dielectric microstadium and thus a low lasing threshold.

4.2 Numerical simulations of small stadiums

We calculated numerically the high-quality modes in 2D dielectric stadium cavities. The radius of the half circles is r, and the length of the straight segments is $2a$ (Fig. 4.1 (a)). The area of the stadium is fixed while its shape is varied. We define the deformation $\epsilon \equiv a/r$. In our simulation, ϵ ranges from 0.1 to 1.6. The nonintegrable nature of the problem precludes analytical results, thus we resorted to numerical computation in the analysis of eigenmodes in a dielectric stadium surrounded by vacuum. The refractive index of the dielectric $n = 3$. Using the finite-difference time-domain (FDTD) method [82], we solved the Maxwell's equations for the electromagnetic field both inside and outside the cavity. The vacuum outside the cavity is terminated by a uniaxial perfectly matched layer (UPML) that absorbs light escaping from the dielectric stadium into the vacuum. We identify and characterize all high-Q modes in the spectral range of 600 - 1200 nm in two-step calculations. First, a short optical pulse of broad bandwidth is launched across the cavity to excite all resonant modes in the (vacuum) wavelength range of 600 - 1200 nm. Photons in the low-Q modes quickly leak out of the cavity. Long after the excitation pulse is gone, photons that still stay inside the cavity must be in one of the high-Q modes. The Fourier transform of the intracavity electromagnetic field exhibits narrow spectral peaks that correspond to these long-lived modes. The linewidth of each mode reflects its Q value. Next, we repeated the FDTD calculation with quasi-continuous wave excitation at the frequency of a high-Q mode. Since only one high-Q mode is excited, the steady-state distribution of the electromagnetic field exhibits the spatial profile of this mode.

To find out the classical ray trajectories that the high-Q modes correspond to, we obtained the quantum Poincaré sections of their wavefunctions. We calculated the Husimi phase space projection of a mode from its electric field at the stadium boundary. The coordinates of the Husimi map are s and $\sin\chi$. s is the length along the boundary of the stadium from point P (see the inset of Fig. 4.1), normalized to the perimeter of the stadium. $\sin\chi \equiv k_{\|}/k$, where $k_{\|}$ is the k vector in the direction tangent to the stadium boundary, $k = 2\pi n/\lambda$, λ is the wavelength in vacuum.

We have considered both transverse electric (TE) and transverse magnetic (TM) polarizations, and obtained similar results in our calculation. The data presented in this section are for the TM polarizations. Starting with a perfect circle, we gradually increased the deformation ϵ while keeping the area of the stadium at 3.3 μm^2. In the range of ϵ from 0.1 to 1.6, we identified four classes of high-Q modes in the (vacuum)

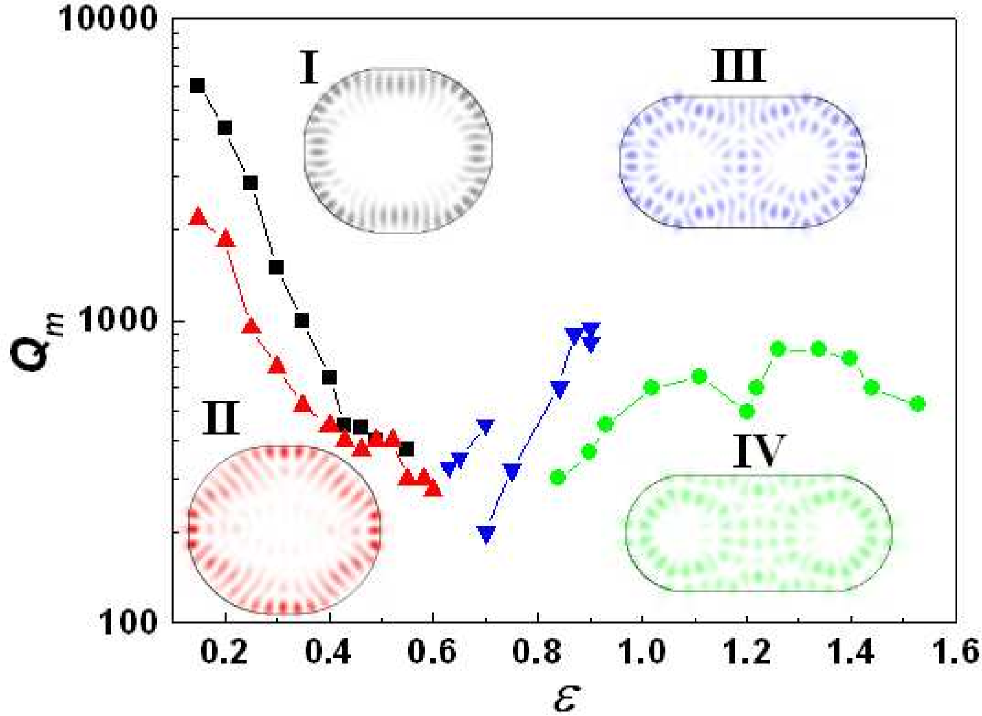

Figure 4.2: Maximum quality factor Q_m of class I, II, III and IV modes, represented by squares, up-triangles, down-triangles, and circles, as a function of deformation ϵ. Insets are the spatial intensity distributions of typical modes of each class.

wavelength range of 600 - 1200 nm. Figure 4.2 shows their maximum quality factor Q_m as a function of ϵ. Within each class, the highest-Q modes at different ϵ may not be the same mode. As ϵ increases, Q_m first decreases quickly, reaches a minimum at $\epsilon \sim 0.6$, then starts increasing before reaching a plateau at large ϵ. Hence, $\epsilon \sim 0.6$ seems to be a turning point, across which the spatial profiles of the high-Q modes also change significantly. Based on these phenomena, we divided the deformation into two regimes. In the regime of small deformation ($\epsilon \lesssim 0.6$), Q_m decreases monotonically as ϵ increases. As will be shown in the next section, the high-Q modes in this regime, labeled as class I and class II, have field maxima only near the stadium boundary. In the regime of large deformation ($\epsilon \gtrsim 0.6$), Q_m first increases with ϵ, then remains nearly constant with small oscillations after ϵ exceeds 0.9. The high-Q modes in this regime, labeled as class III and class IV, exhibit very different spatial profiles from those at small deformation. As will be shown in section V, they have field maxima not only close to the boundary, but also near the center of the stadium. Therefore, across the boundary ($\epsilon \sim 0.6$) of the above two regimes, the characteristic of the high-Q modes changes dramatically, in other words, different types of eigenmodes take over as the high-Q modes. In the following a systematic study of the high-Q modes in the two regimes of deformation is presented.

4.2.1 high-Q modes in the regime of small deformation

We used the short pulse excitation to find all the high-Q modes in the (vacuum) wavelength range of 600 - 1200 nm for $\epsilon \lesssim 0.6$. Figure 4.3 is the spectrum of electromagnetic

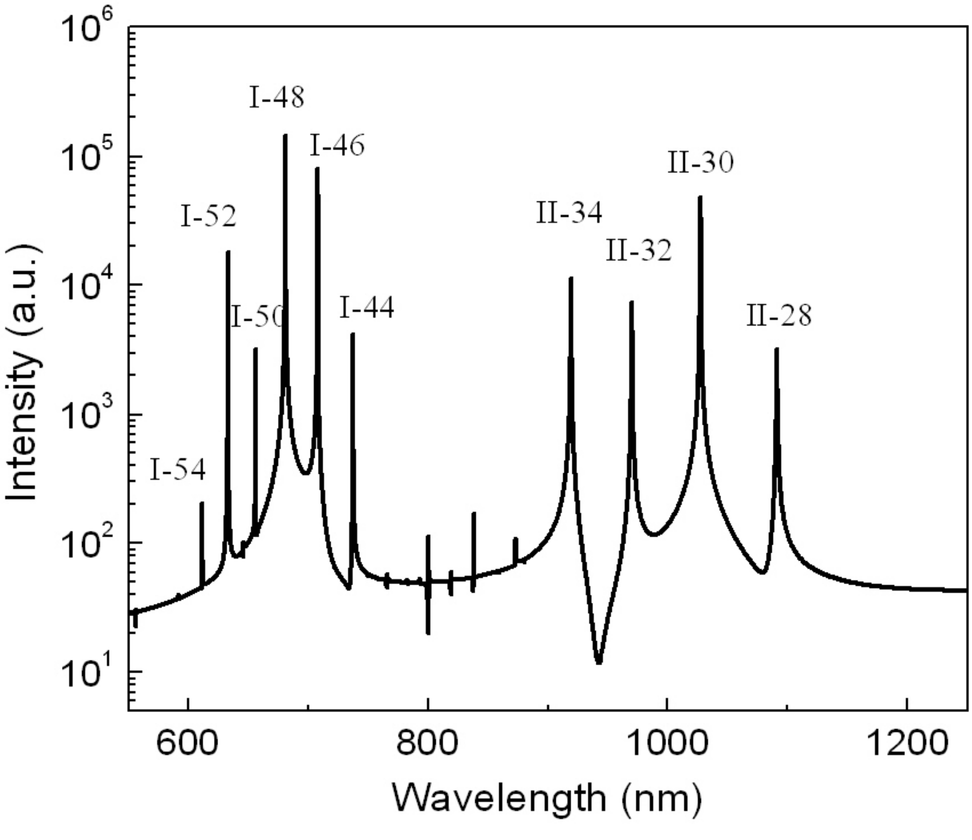

Figure 4.3: Spectra of electromagnetic field inside the dielectric stadium long after the short excitation pulse is gone. The deformation is $\epsilon = 0.15$

field inside the stadium of $\epsilon = 0.15$ long after the short excitation pulse is gone. There are two groups of high-Q modes. Within each group, the modes have similar spatial profiles. The group of class I modes is at shorter wavelength, while the group of class II modes at longer wavelength. Using the quasi-continuous wave excitation, we studied individual high-Q modes. Figure 4.4 (a) shows the spatial intensity distribution of a class I mode at $\epsilon = 0.15$. It is clear that the class I mode is not a chaotic mode, but a scar mode. To identify the classical ray trajectories that the class I modes correspond to, we calculated the quantum Poincaré sections of their wavefunctions. Figure 4.4 (b) is the Husimi phase space projection of the class I mode shown in Fig. 4.4 (a). The main features are four "pads", which correspond to the rectangle orbit as illustrated in the inset of Fig. 4.4 (b). Above the four pads, there is a "belt" which may represent long orbits that slide along the stadium boundary. Moreover, the Husimi function has zero points near the diamond orbit [marked by crosses in Fig. 4.4 (b)].

Similarly, the class II modes are also scar modes [Fig. 4.5 (a)]. As shown in Fig. 4.5 (b), the Husimi map of a class II mode consists of four "pads" that correspond to the diamond orbit and a "belt" on top of it. It also reveals four zero points of the Husimi function near the rectangle orbit [marked by dots in Fig. 4.5 (b)]. It is not clear why class I modes form a group of high-Q modes in the wavelength region around 700 nm, while the class II modes form a group of high-Q modes around $\lambda \sim 1000$ nm. We notice that within each group of high-Q modes, the frequency spacing between adjacent modes is constant. Individual modes can be labeled by the number of field maxima N along the

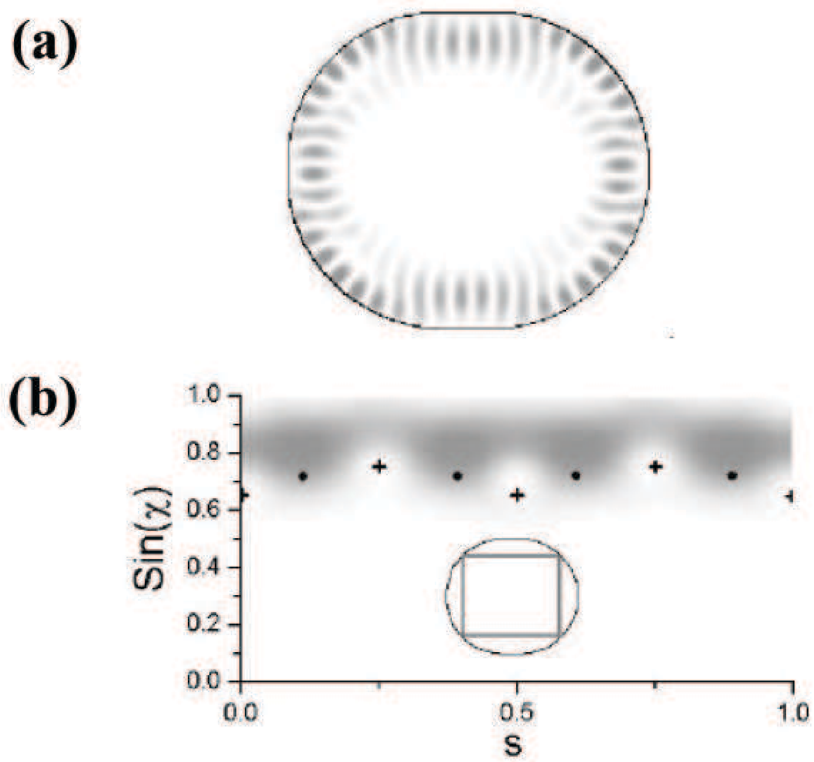

Figure 4.4: (a) Spatial intensity distribution of a class I mode in the dielectric stadium of ϵ =0.15. (b) Husimi phase space projection of the mode in (a). The black dots represent the rectangle orbit, which is shown schematically in the inset. The crosses correspond to the diamond orbit.

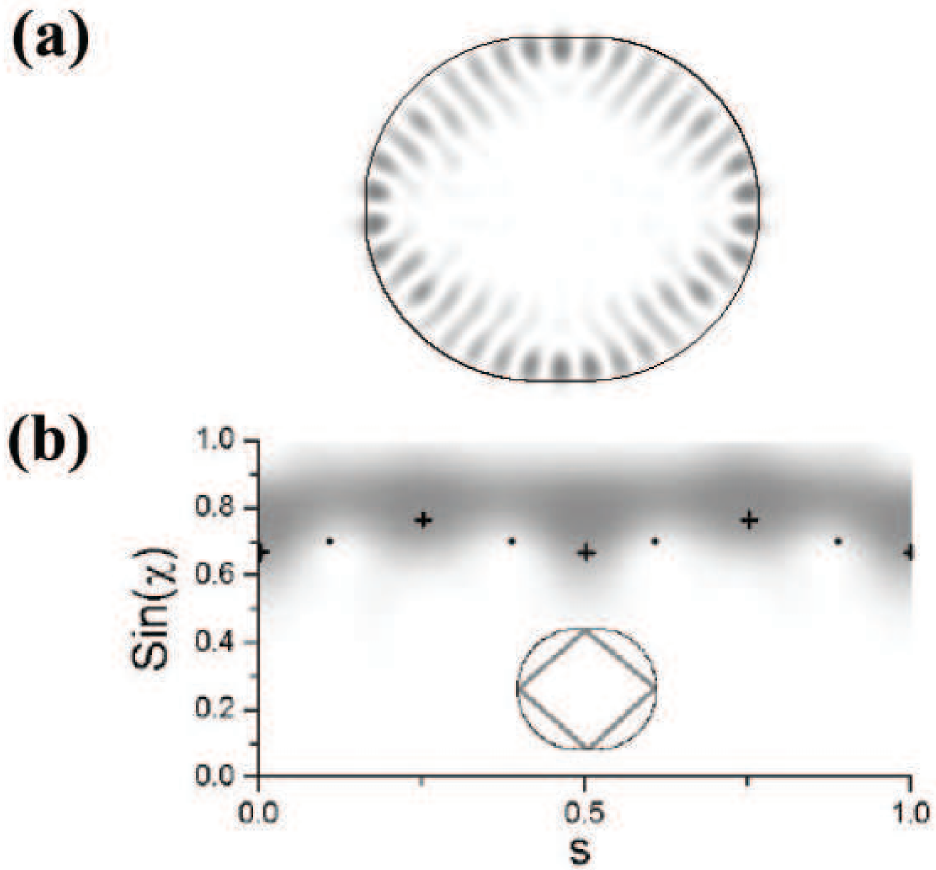

Figure 4.5: (a) Spatial intensity distribution of a class II mode in the dielectric stadium of ϵ =0.15. (b) Husimi phase space projection of the mode in (a). The crosses represent the diamond orbit, which is shown schematically in the inset. The black dots correspond to the rectangle orbit.

stadium boundary, as shown in Fig. 2(a). N is an even number due to the symmetry of the wavefunction with respective to the horizontal x-axis and the vertical y-axis. We compared the quality factor of individual modes within a group of high-Q modes. The modes located spectrally near the group center always have higher Q values than those away from the center. The small peaks around λ = 800nm in Fig. 4.3 (a) are class I or II modes with lower Q factor.

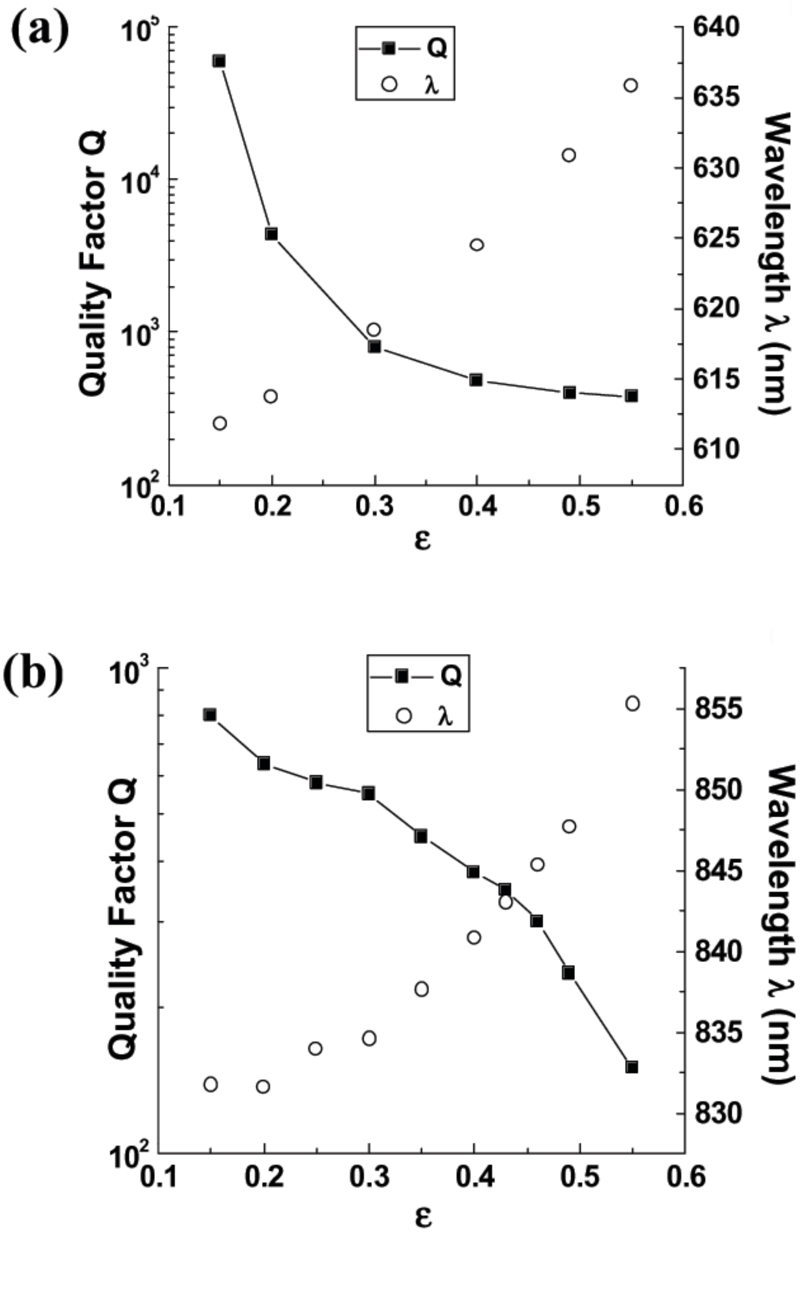

Figure 4.6: Quality factor Q (solid squares) and wavelength (open circles) of: (a) the class I mode in Fig. 4.4, and (b) the class II mode in Fig. 4.5 as a function of the deformation ϵ.

To find out how the class I (II) modes change with the deformation, we traced individual modes as we gradually varied ϵ. Figure 4.6 (a) [(b)] shows the calculation result for the class I (II) mode in Fig. 4.4 (a) [4.5 (a)]. When ϵ increases, the mode shifts to longer wavelength, and its Q value decreases. The wavelength shift is caused by an increase in the stadium perimeter with ϵ as the area of the stadium remains constant. We repeated the calculation with different class I (II) modes, and observed similar behaviors.

4.2.2 high-Q modes in the regime of large deformation

In the regime of large deformation $\epsilon \gtrsim 0.6$, we again found all the high-Q modes in the (vacuum) wavelength range of 600 - 1200 nm with the short pulse excitation. Figure 4.7 shows the spectrum in the stadium of $\epsilon = 0.84$ long after the short excitation pulse is gone. The high-Q modes are sparse compared to the case of small deformation. Based on their intensity distributions in the real space and phase space, we classified the high-Q modes into two categories, class III and class IV. Figures 4.8 (4.9) exhibits the spatial intensity distributions of two class III (IV) modes. These modes have field maxima not only close to the boundary, but also in the center of the stadium. The class III mode has a structure of "double-pentagon", and class IV "double-circle". The "double-circle" modes have been observed previously in the stadium-shaped microwave billiard and dielectric cavity [76, 83]. What is not known before is the change of their quality factor with deformation ϵ. Figure 4.8 (c) [4.9 (c)] shows how the Q values of individual class III (IV) modes vary with ϵ near $\epsilon = 1.0$. For each mode, its Q value first increases with ϵ, then

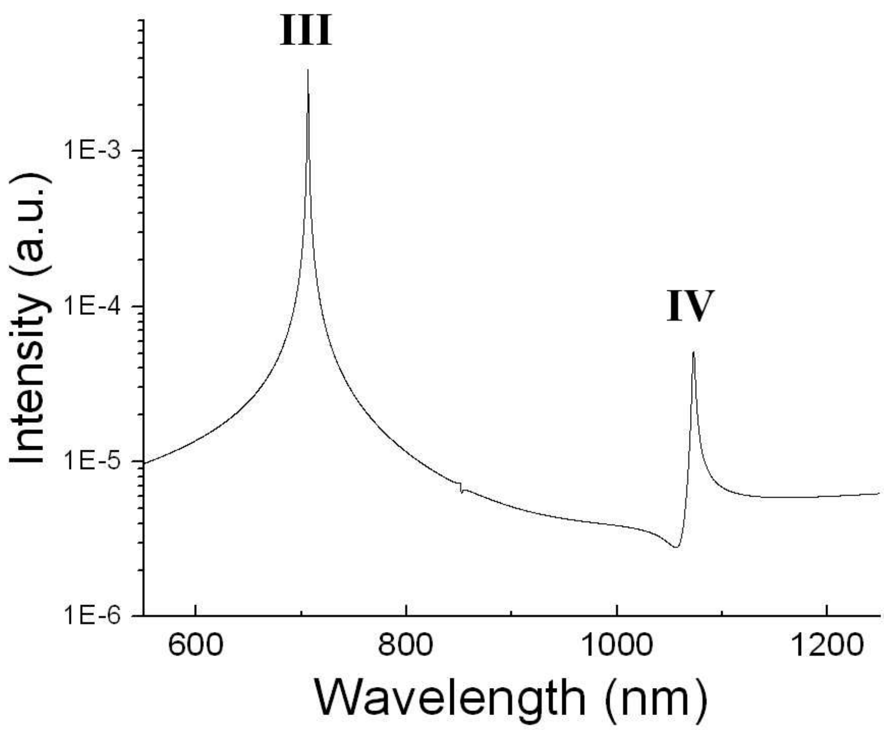

Figure 4.7: Spectra of electromagnetic field inside the dielectric stadium long after the short excitation pulse is gone. The deformation is $\epsilon = 0.84$

decreases. There exists an optimal deformation ϵ_m for each mode at which its quality factor reaches the maximum. Figure 4.8 (c) [4.9 (c)] also shows that the wavelengths of individual class III (IV) modes increase with ϵ. This behavior is similar to that of class I and class II modes.

The two modes of class III (IV), shown in Fig. 4.8 (4.9), have the same profile except that the number of field maxima is different. We label the modes in terms of the number of field maxima N along the stadium boundary. The two modes in Fig. 4.8 (a) and (b) are labeled as III-56 and III-58, and the two modes in Fig. 4.9 (a) and (b) are IV-28 and IV-30. Because the stadium has symmetries about the x and y axes, N is always an even number. The two modes in Fig. 4.8 (4.9) are adjacent modes, as their N numbers differ by 2. The higher the N, the shorter the wavelength. After the mode of order N reaches its maximum Q at certain ϵ, a further increase of ϵ sees the mode of order $N+2$ in the same class takes over as the high-Q mode. Its Q value reaches the maximum at larger deformation. Hence, within class III or class IV modes, the high-Q mode hops from the mode of lower-N consecutively to the one of higher-N as ϵ increases. Since the higher-N modes have shorter wavelength, the high-Q mode jumps to shorter wavelength. This behavior is clearly seen in Fig. 4.10 for the class IV modes when ϵ increases in small steps from 0.96 to 1.07 and N changes from 26 to 30. Individual modes shift slightly to longer wavelength as ϵ increases. Yet the high-Q mode migrates to shorter wavelength, forming a "high-Q band" with increasing ϵ. Figure 4.11 shows the optimal deformation ϵ_m and the corresponding wavelength for each class IV mode in this high-Q band. The

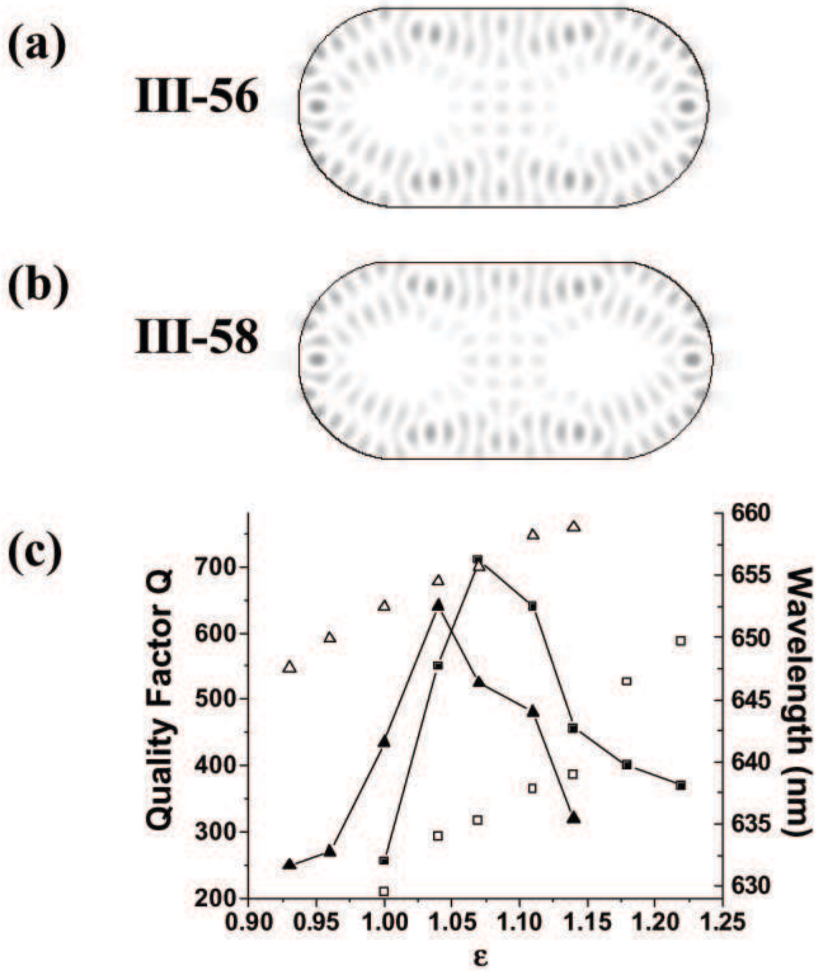

Figure 4.8: (a) and (b) are spatial intensity distributions of two adjacent class III modes of order $N = 56$ and 58 at their optimal deformations. (c) Solid squares (triangles) and open squares (triangles) represent the quality factor and wavelength of mode III-56 (III-58).

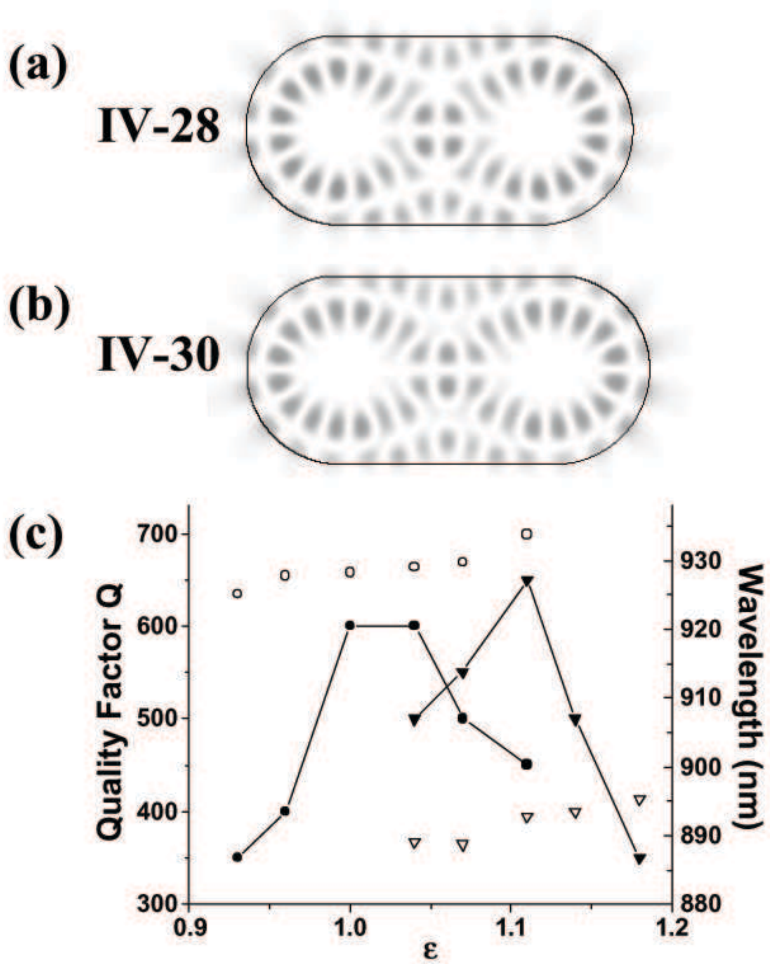

Figure 4.9: (a) and (b) are spatial intensity distributions of two adjacent class IV modes of order $N = 28$ and 30 at their optimal deformations. (c) Solid circles (triangles) and open circles (triangles) represent the quality factor and wavelength of mode IV-28 (IV-30).

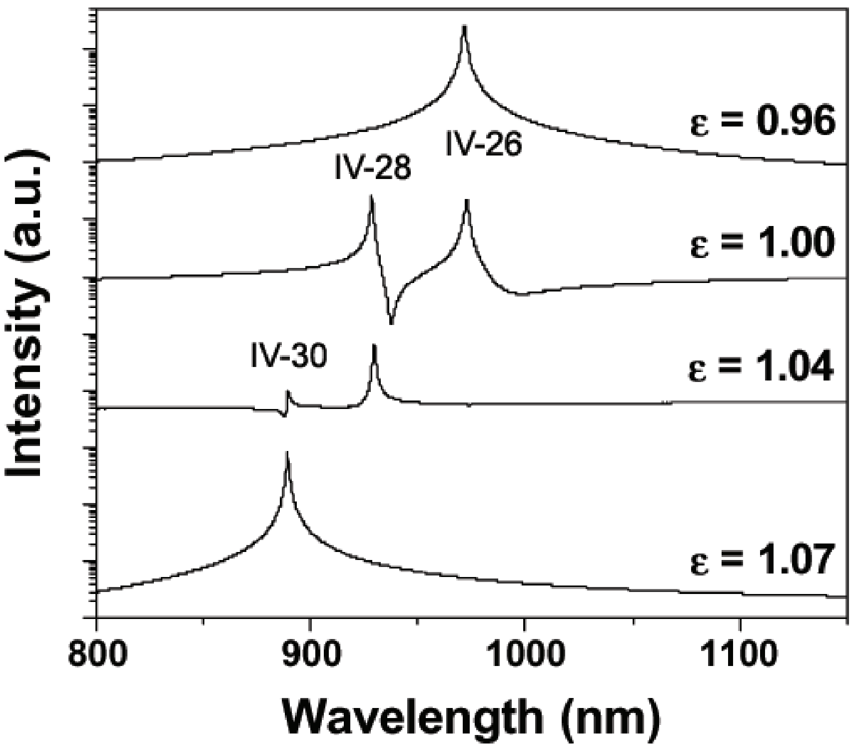

Figure 4.10: Intracavity excitation spectra long after the short excitation pulse is gone. ϵ increases in small steps from 0.96 to 1.07.

modes are antisymmetric with respective to the horizontal x-axis, while their symmetry to the vertical y-axis alternates between odd and even.

The non-monotonic change in the Q value of a high-quality mode with ϵ and the existence of an optimal deformation for maximum Q have not been reported before. To explain these phenomena, we intend to understand the mode structures and their corresponding classical ray trajectories. As an example, we consider a class IV mode, whose intensity distribution is shown in Fig. 4.12 (a). Figure 4.12 (c) is the Husimi phase space projection of this class IV mode at its optical deformation $\epsilon_m = 1.04$. It reveals that

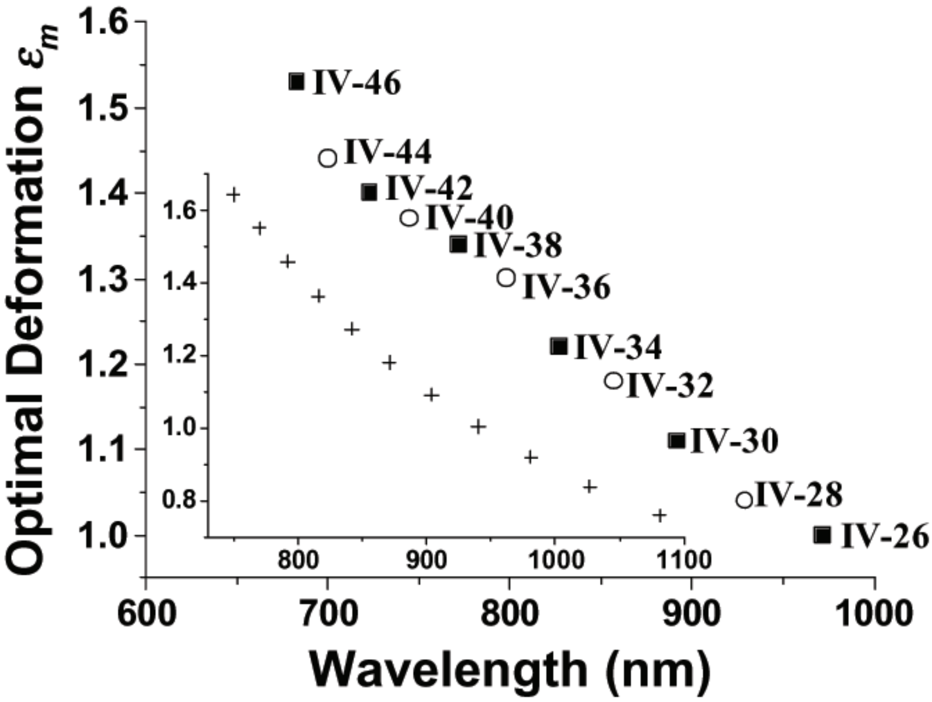

Figure 4.11: Optimal deformation ϵ_m and corresponding wavelength for each class IV mode in a high-Q band. Solid squares (open circle) represent the modes of even (odd) symmetry about the y-axis. The inset shows the semiclassical prediction of wavelengths (in unit of nm, horizontal axis) of class IV modes at various deformations (vertical axis) in dielectric stadium cavities.

the class IV mode consists mainly of two topologically distinct short periodic orbits: one is the diamond orbit [marked by black dots in Fig. 4.12 (c)], the other is the bow-tie orbit [marked by crosses in Fig. 4.12 (c)]. This result illustrates that the class IV mode is still a scar mode. Note that scarring was introduced as a term for non-uniform field patterns in systems like the stadium, because they were unexpected in the short-wavelength limit where ray physics dominated the cavity properties. In the small cavities we simulated, the wavelength was not short enough to apply the random-matrix theory, and the wave solutions exhibited regular spatial patterns. Yet in the range of nkR that we studied, most low-Q modes fill more or less uniformly the entire real space and phase space. These modes are regarded as chaotic modes. In contrast, the class IV mode, as shown in Fig. 4.12, exhibits non-uniform distribution in real space and phase space, thus it can be considered as a scar mode. Its corresponding periodic orbits are above the critical line for refractive escape ($\sin\chi = 1/3$). These orbits, which are unstable in the closed stadium, remain unstable in the open stadium owing to small light leakage and long dwell time inside the cavity. However, the measure of orbit instability, i.e., the Lypounov exponent, is changed due to the open boundary condition. Because the class IV mode is a multi-orbit scar mode, the interference of waves propagating along the constituent orbits shown in Fig. 4.12 (b) could minimize light leakage out of the cavity [84, 85]. The interference effect depends on the phases of waves traveling in different orbits. Because the phase delay varies with the orbit length which is a function of ϵ, the interference effect may be optimized at certain deformation that gives the maximum Q value.

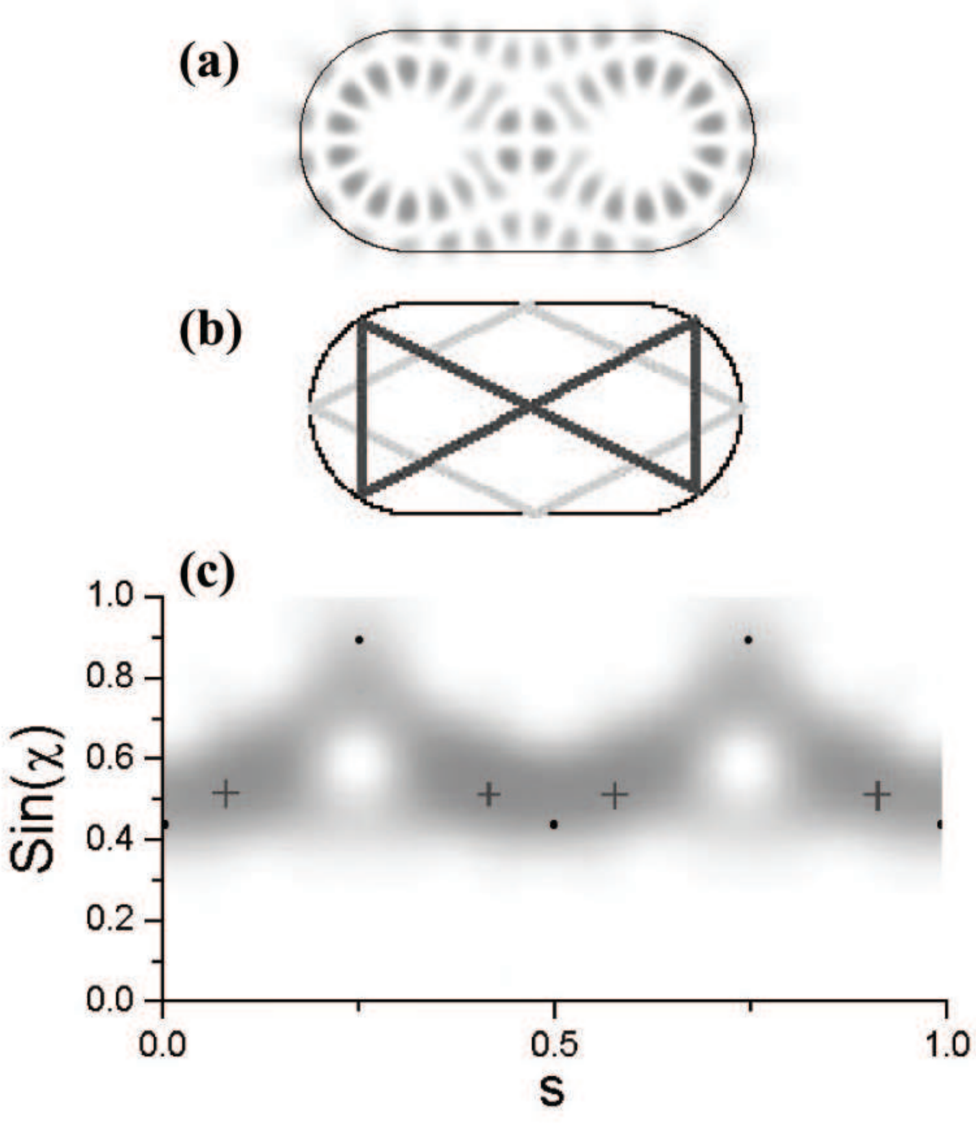

Figure 4.12: Intensity distribution in real space (a) and phase space (c) of mode IV-28 at its optimal deformation $\epsilon_m = 1.04$. (b) is a schematic of the constituent UPOs. The black dots (crosses) in (c) correspond to the diamond (bow-tie) orbit.

Next we present a possible explanation for the hopping of the high-Q modes to shorter wavelength with increasing ϵ. To find the wavelength of a multi-orbit scar mode, we applied the quantization rule to all the constituent orbits. Taking class IV modes as an example, we utilized the Bohr-Sommerfeld quantization rule for the constituent diamond and bow-tie orbits to determine the wavenumber $k = 2\pi n/\lambda$. Due to the relatively small kR values of the class IV modes in our calculation, we consider only the resonances with the lowest excitation in the transverse direction of the orbit. In other words, we only need to quantize the longitudinal motion of ray along the orbit [86]. The quantization rule for the diamond orbit is $k_d\, L_d + \sum_{i=1}^{4} \phi_i - \nu_d\, \pi/2 = 2\pi\, m_d$, where k_d is the wavenumber, L_d is the length of the diamond orbit, ϕ_i is the phase shift acquired during the i-th bounce of the orbit with the stadium boundary, ν_d is the number of conjugate points along the diamond orbit, m_d is an integer. Note that ϕ_i depends on the incident angle χ of the ray on the stadium boundary, which varies with ϵ [87]. ν_d is equal to the number of bounces with the half circles. For the diamond orbit, $\nu_d = 2$. Similarly, the quantization rule for the bow-tie orbit is $k_b\, L_b + \sum_{i=1}^{4} \varphi_i - \nu_b\, \pi/2 = 2\pi\, m_b$, where k_b is the wavenumber, L_b is the length of the bow-tie orbit, φ_i is the phase shift acquired during the i-th bounce of the orbit with the stadium boundary, ν_b is the number of conjugate points along the bow-tie orbit which is equal to 4, and m_b is an integer. If the coupling between the constituent orbits is neglected, the class IV modes exist only when the quantized wavenumbers of the two orbits coincide, i.e., $k_d = k_b$. We solved $k_d = k_b$ in the wavelength range of 600 - 1200 nm at various deformation. The inset of Fig.

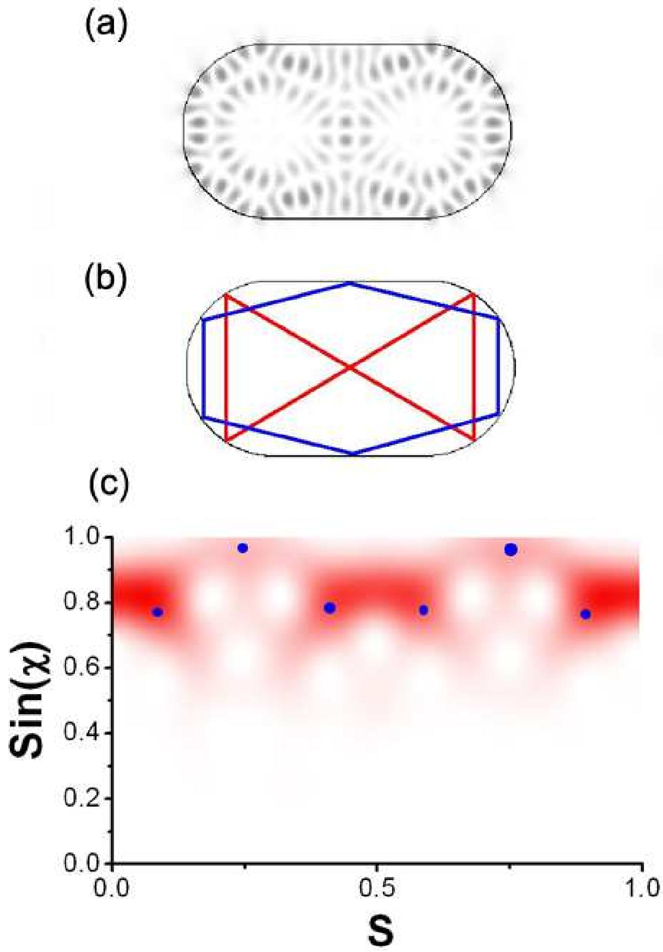

Figure 4.13: (a) Spatial intensity distribution. (b) Possible constituent UPOs (c) Husimi projection of the class III mode III-50 in Fig. 4.7.

4.11 shows the wavelength that satisfies $k_d = k_b$ as a function of ϵ. As ϵ increases, the wavelength decreases. Because the coupling between the constituent orbits is neglected, the wavelength determined by the quantization rule deviates from that obtained by the numerical simulation [88, 89]. Nevertheless, the blue shift of the class IV high-Q modes with increasing ϵ agrees qualitatively with the prediction of the semiclassical quantization rule.

The class III modes behave very much like the class IV modes. We identified the possible constituent UPOs as hexagon orbit and bow-tie orbit. Finally we studied the high-Q modes in the cross-over regime of $\epsilon \sim 0.6$. When ϵ increases and approaches the turning point of 0.6, the "belts" in Figs. 4.4 (b) and 4.5 (b) gradually disappear from class I and II modes, meanwhile additional components corresponding to non-WG-type short UPOs start emerging in the Husimi map.

For comparison, we also calculated the high-quality modes of an open integral system (dielectric elliptical cavity) and a partially chaotic system (dielectric quadrupolar cavity). The boundary of elliptical cavity is defined as $x^2/a^2 + y^2/b^2 = 1$, and deformation ϵ is defined as $\epsilon = a/b$, a is the semimajor axis and b is semiminor axis. The quadrupolar shape is defined as $r(\theta) = r_0\,[1 + \epsilon\,\cos(2\theta)]$. Typical high-$Q$ modes in both cavity show WG-like pattern with major intensity distributed around the boundary, as shown in the insets of Fig. 4.14. These modes do not exhibit non-monotonic change of their quality factors with the deformation, neither do they have optimal deformations at which their Q values are maximized. Whether the behaviors of the high-quality modes observed in the dielectric stadium cavities are unique characteristic of fully chaotic systems requires further study.

Finally we discuss the implication of our results to the design of microlasers. For many applications of microlasers, large deformation of cavity shape from circle is desired for directional output. However, the spoiling of Q factor in the deformed cavity results in an increase of the lasing threshold. Our calculation demonstrates that in the dielectric

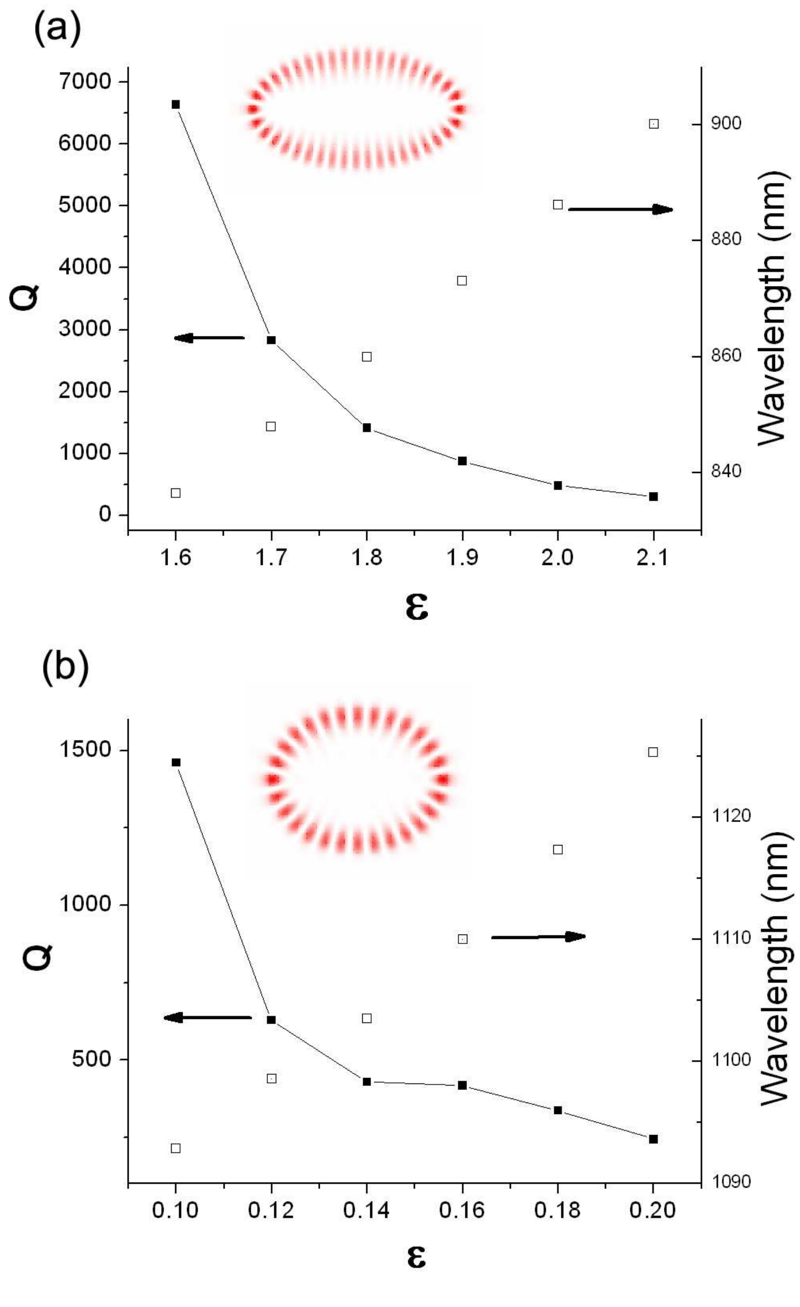

Figure 4.14: Solid squares and open squares represent the quality factor and wavelength of a typical high-Q mode in (a) elliptical cavity and (b) quadrupolar cavity as a function of deformation. Insets are the intensity distributions of corresponding modes

stadium microcavities the Q spoiling would stop after the deformation exceeds a critical value. This behavior leads to a decent lasing threshold even at large deformation. Note that our results are obtained with the calculation over a wide spectral range. The commonly used semiconductor gain media have much narrower gain spectra. Since the high-Q modes at large deformation are sparse, the chance of having a high-quality scar mode within the gain spectrum is rather low. If the high-Q scar modes do not overlap with the gain spectrum, lasing may occur in the low-Q chaotic modes located within the gain spectrum but with much higher lasing threshold. Therefore, to reach low lasing threshold, one must carefully choose the size and deformation of the stadium so that a high-Q mode lies within the gain spectrum. Because of the low density of high-quality modes at large deformation, it is easy to realize single-mode lasing, which has potential application to single-mode laser.

4.3 Experimental optimization of lasing threshold

In this section, we demonstrate experimentally that low lasing threshold can be obtained in a semiconductor microstadium by controlling its shape. Because the waveguide structure of sample we used in our experiment is not optimized for our purpose, the sizes of microstadiums are larger than simulation ones in previous section to lower lasing threshold.

The sample was grown on a GaAs substrate by molecular beam epitaxy. The layer structure consists of 500nm AlGaAs and 200nm GaAs. In the middle of the GaAs layer

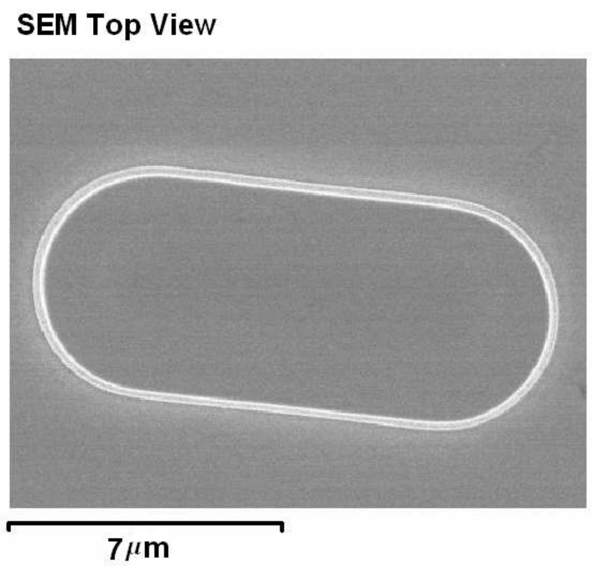

Figure 4.15: SEM image of a semiconductor microstadium cavity (top view).

there is an InAs quantum well (QW) of 0.6nm. The lower refractive index of AlGaAs layer leads to the formation of a slab waveguide in the top GaAs layer. Stadium patterns were defined by photolithography. Then wet chemical etching was followed to form cylinder structures. The major-to-minor-axis ratio of the stadiums was varied over a wide range while the stadium area remains nearly constant. Figure 4.15 shows a SEM image of a microstadium cavity.

To study their lasing properties, the stadium microcavities were cooled to 10K in a cryostat, and optically pumped by a mode-locked Ti-sapphire laser at 790nm. The optical setup is similar to the one in Chapter 3, as shown in Fig. 3.5. The pump beam was focused by an objective lens onto a single stadium. The emission was collected by the same lens, and sent to a spectrometer. As the pump power increased above threshold, certain peak corresponding to cavity resonance showed drastically increasing of peak

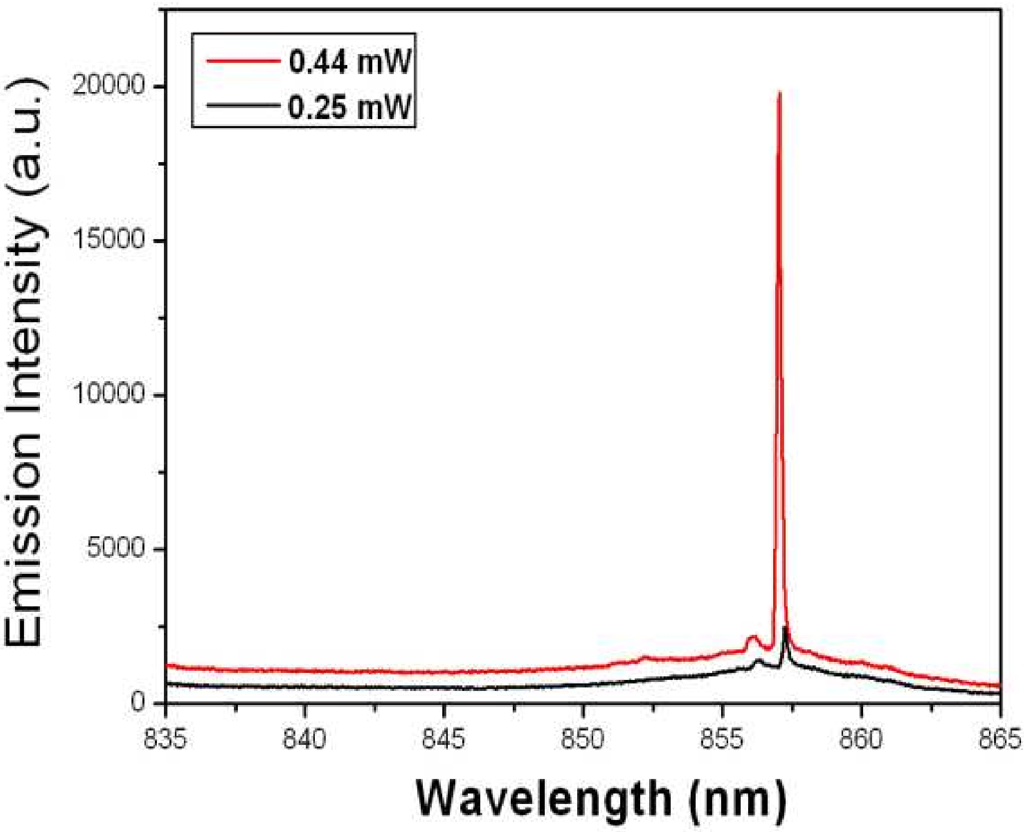

Figure 4.16: Emission spectra from a microstadium of $\epsilon \sim 1.51$ under pump power 0.44 mW (red curve) and 0.25 mW (black curve).

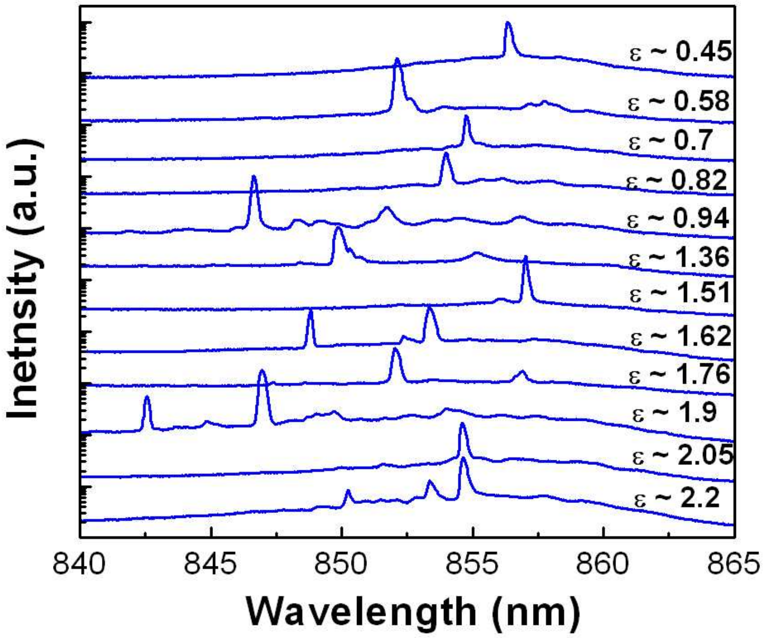

Figure 4.17: Lasing spectra from twelve GaAs stadiums with different deformations.

intensity (Fig. 4.16), accompanied with width narrowing. These phenomena confirmed lasing behavior in microstadiums.

Lasing was realized in most stadiums with ϵ ranging from 0.4 to 2.2 and area $\sim 70\mu$m^2. Figure 4.17 shows the emission spectra of twelve stadiums slightly above their lasing thresholds so that we mainly see the first lasing mode. As ϵ increases, the first lasing mode jumps back and forth within the gain spectrum of the InAs QW. It is not always located near the peak of the gain spectrum. At some deformation, e.g. $\epsilon = 0.94$, 1.9, the first lasing mode is far from the gain maximum at $\lambda \sim 857$nm. This phenomenon is not caused by lack of cavity modes near the maximum of the gain spectrum. A few small and broad peaks in the emission spectrum between 847nm and 857nm are due to cavity resonances. These resonances experiences higher gain than the lasing mode at $\lambda \approx 847$nm. The only reason they do not lase is their quality (Q) factors are low. This result indicates the lasing modes, especially the first one, must be high-Q modes. However, when the lasing mode is away from the maximum of the gain spectrum, the relatively low optical gain at the lasing frequency results in high lasing threshold. This is confirmed in Fig. 4.18, which shows the lasing threshold strongly depends on the spectral distance between the first lasing mode and the maximum of the gain spectrum. Unlike many deformed microcavities [49, 51], the lasing threshold in a microstadium does not increase monotonically with the deformation, e.g., the lasing thresholds in stadiums of $\epsilon = 0.7$ and 2.2 are nearly the same despite of their dramatically different deformations.

To investigate individual lasing modes in microstadiums, we used a narrow band pass filter of 1 nm to select one lasing mode and took its near-field image with a CCD camera. Figure 4.19 shows the measurement result of a stadium with $\epsilon = 1.51$. The solid curve is the emission spectrum when the narrow bandpass filter is tuned to the first lasing mode at $\lambda = 856.95$nm. The near-field image exhibits four bright spots on the curved part of stadium boundary. We believe these four spots represent the positions of major escape of laser light from the stadium. They can be seen from the top because of optical scattering at the boundary. However, the scattering inside the stadium is so weak that the spatial intensity distribution of lasing mode across the stadium could not be observed from the top. By tuning the bandpass filter away from cavity resonances, we took the near-field image of amplified spontaneous emission (ASE) shown as the inset

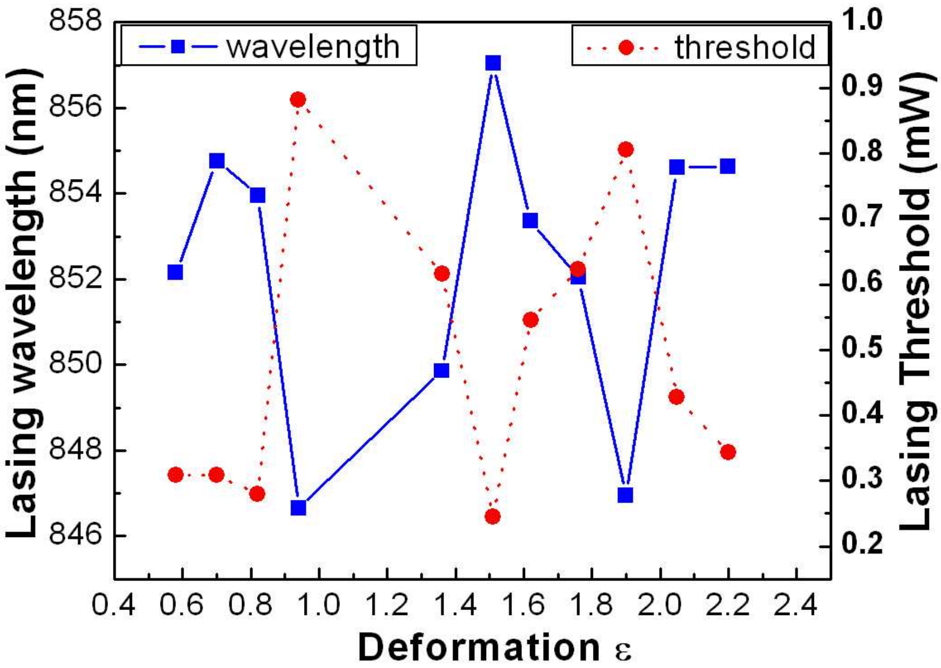

Figure 4.18: Wavelength and lasing threshold of the first lasing mode of the microstadiums in Fig. 4.17 as a function of ϵ.

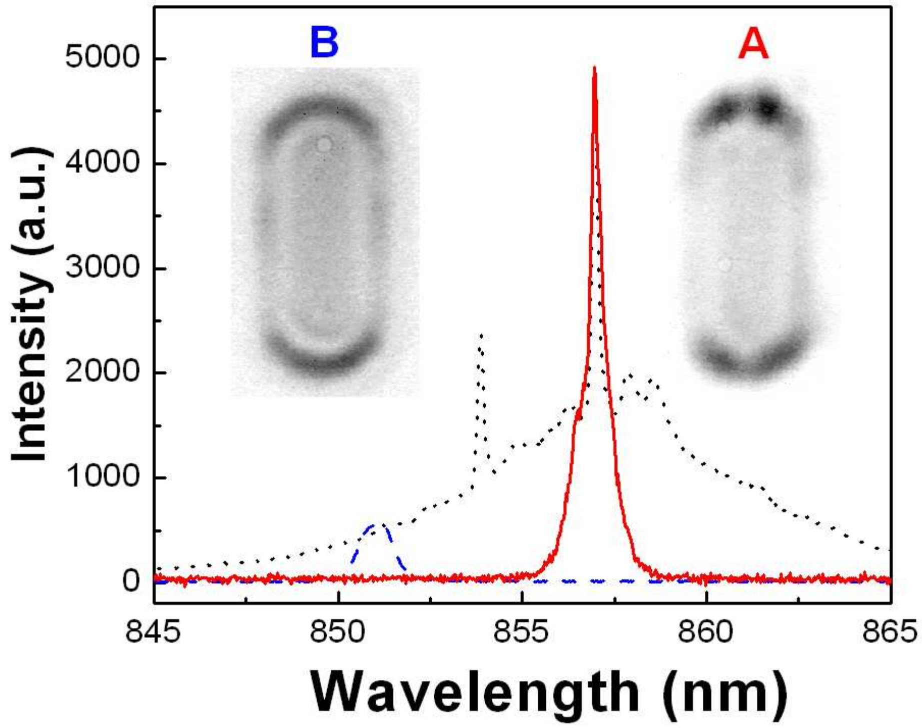

Figure 4.19: The dotted curve is the lasing spectrum from a GaAs stadium with ϵ =1.51. A bandpass filter of 1 nm bandwidth selects the first lasing mode at 856.95 nm (solid curve), and the inset A is the corresponding near-field image taken simultaneously. The dashed curve is the spectrum when the bandpass filter is tuned away from cavity resonances, the corresponding near-field image of ASE is shown in the inset B.

B of Fig. 4.19. The virtually constant intensity along the curved boundary suggests the ASE leaves the stadium mainly through the boundary of half circles instead of the straight segments. The clear difference between the near-field images of lasing mode and ASE not only confirms the bright spots in the former are from the laser emission, but also reveals the escape routes for laser emission and ASE are distinct.

To understand the experimental results, we simulated lasing in GaAs microstadiums. The polarization measurement of laser emission from the stadium side wall confirmed the lasing modes are transverse electric (TE) polarized (the electric field is parallel to the top surface of the stadium). From the calculation of TE wave guided in the GaAs layer, we obtained the effective index of refraction $n_{eff} \simeq 3.3$. The exact size and shape of the fabricated stadiums were extracted from the scanning electron microscope (SEM) images. Using the finite-difference time-domain (FDTD) method, we solved the Maxwell's equations for electromagnetic (EM) field inside and outside a two-dimensional (2D) stadium of refractive index n_{eff} together with the four-level rate equations for electronic populations in the InAs QW [19]. Light exiting the stadium into the surrounding air was absorbed by uniaxial perfectly matched layers. The external pumping rate for electronic populations was assumed uniform across the stadium, similar to the experimental situation. We gradually increased the pumping rate until one mode started lasing. Fourier transform of the EM field gave the frequency of the first lasing mode. Figure 4.20 (a) shows the intensity distribution of the first lasing mode at $\lambda = 850.7$ nm in the stadium with $\epsilon = 1.51$ and area $\simeq 70\mu\text{m}^2$. The pumping rate is slight above the lasing threshold. For comparison, we also calculated the high-Q modes in the passive stadium (without optical gain), in the way discussed in previous simulation section. By comparing the lasing mode with the resonant modes of the passive cavity, we find the first lasing mode corresponds to the highest-quality mode within the gain spectrum. As shown in Fig. 4.20 (a), the spatial profile of the first lasing mode is almost identical to the mode at $\lambda =$ 850.7nm in the passive stadium. This result illustrates the nonlinear effect on the lasing mode is insignificant when the pumping rate is not far above the lasing threshold.

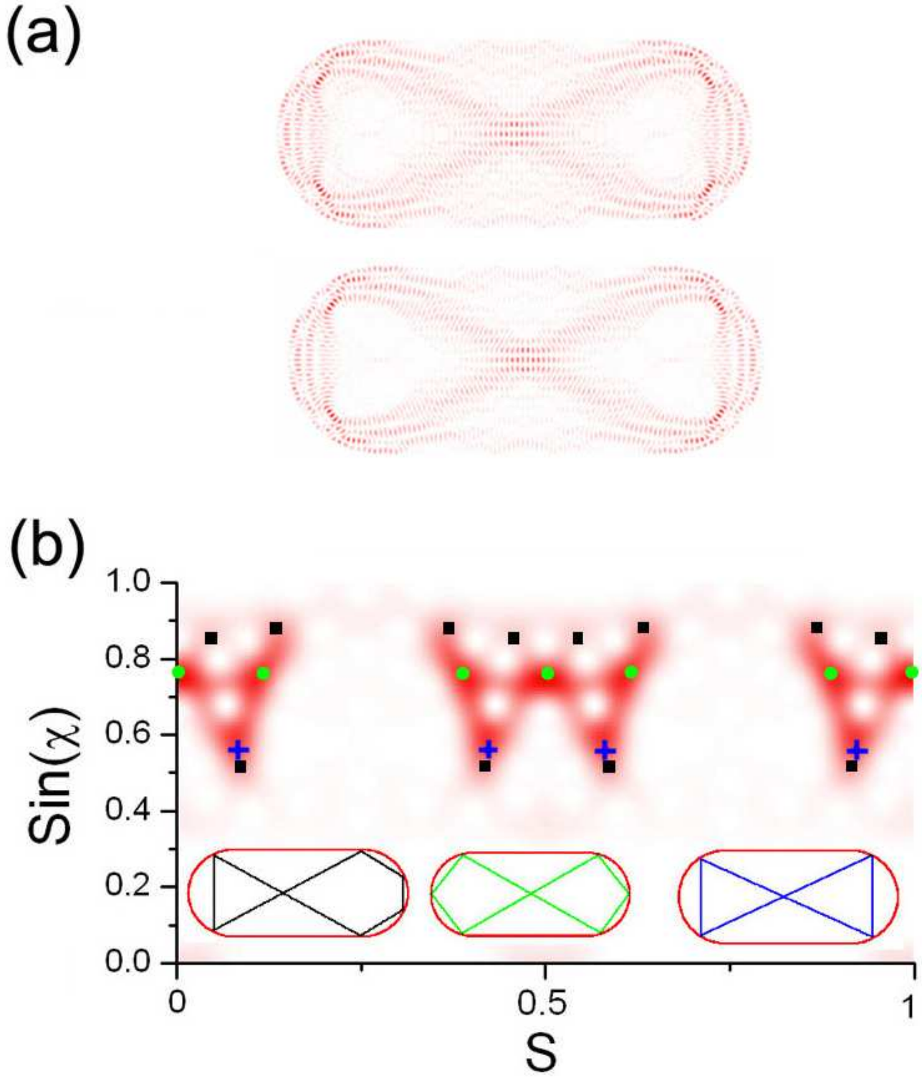

Figure 4.20: (a) Calculated intensity distribution of the first lasing mode in a stadium with $\epsilon = 1.51$ (top), and the corresponding mode in the passive stadium without gain (bottom). Both modes have the wavelength 850.7 nm. (b) Husimi phase space projection of the mode in (a). The squares, dots and crosses mark the positions of three different types of UPOs shown in the inset.

The intensity of light escaping through the stadium boundary can be approximated by the intensity just outside the boundary. From the calculated lasing mode profile, we extracted the intensity about 100nm outside the stadium boundary. To account for the finite spatial resolution in our experiment, the output intensity distribution along the stadium boundary was convoluted with the resolution function of our imaging system. The final result is shown as dashed curve in Fig. 4.21. It agrees well with the measured intensity along the stadium boundary (solid curve), especially since it reproduces the positions of four bright spots in the near-field image of the lasing mode. Since there is no other mode that has similar (low) lasing threshold and output intensity profile like the measured one, we conclude the first lasing mode observed experimentally in the stadium of $\epsilon = 1.51$ corresponds to the calculated mode at $\lambda = 850.7$nm. The slight difference (less than 1%) in wavelength is within the experimental error of determining the refractive index of GaAs and AlGaAs at low temperature. The escape of ASE from a stadium is simulated by classical ray tracing in real space, as the interference effect can be neglected due to lack of coherence in ASE. The initial distribution of 1.2*10^5 rays is uniform in real space (within the cavity) and in angular direction. Each ray is given unit amplitude initially. At each reflection from the boundary, the amplitude is reduced according to the Fresnel formula. The outgoing amplitude is recorded at the position of escape, and reflected ray is followed until its amplitude falls below 10^-4. The calculated the intensity distribution of output rays along the boundary of a stadium with $n_{eff} = 3.3$ and $\epsilon =$ 1.51 is ploted as dashed curve in Fig. 4.21 (b). The ray-tracing result agrees with the

ASE intensity distribution obtained from the near-field image [solid curve in Fig. 4.21 (b)].

To find out the classical ray trajectories that the lasing modes correspond to, we obtained the quantum Poincaré sections of their wavefunctions. Figure 4.20 (b) is the Husimi phase-space projection of the lasing mode in Fig. 4.20 (a), calculated from its electric field at the stadium boundary. It reveals the lasing mode is a scar mode, and it consists mainly of three different types of UPOs plotted in the inset of Fig. 4.20 (b). The asymmetric 6-period orbit (together with it's spatial symmetry partner) is indicated by black squares in phase space, the symmetric double-quadrilateral orbit by green circles, and bow-tie by blue crosses. Since the constituent UPOs are above the critical line for total internal reflection, the lasing mode has long lifetime. We calculated the quality factor of this mode in passive stadium as we varied the deformation ϵ around 1.51, as shown in Fig. 4.22. Its Q value first increases then decreases as ϵ increases, leading to a maximum at $\epsilon = 1.515$. Such variation of quality factor is attributed to interference of waves propagating along the constituent UPOs [80,90]. The interference effect depends on the relative phase of waves traveling in different orbits. The phase delay along each orbit changes with the orbit length as ϵ varies. At some particular deformation, constructive interference may minimize light leakage out of the cavity, thus maximizing the quality factor. Since the actual deformation $\epsilon = 1.51$ is nearly identical (within 0.3%) to the optimum deformation ($\epsilon = 1.515$), the mode is almost at the maximum of its quality factor. Furthermore, its frequency is close to the peak of the gain spectrum. Thus the

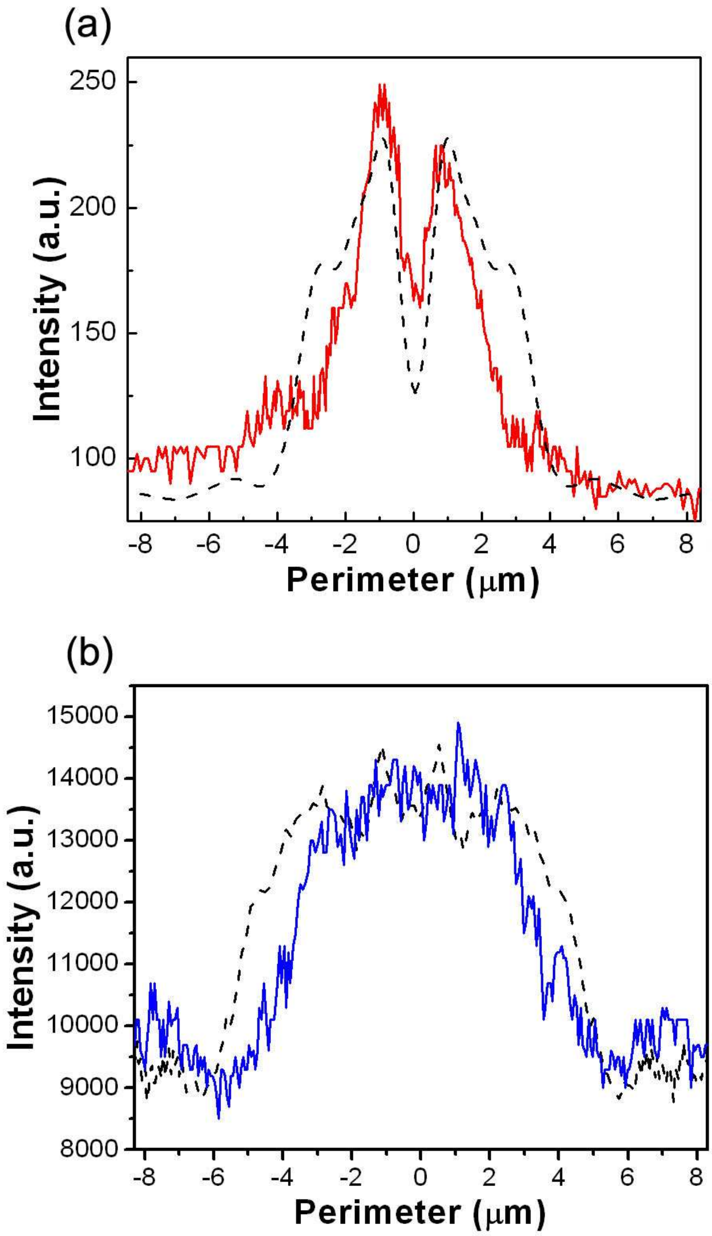

Figure 4.21: Output intensity of laser emission (a) and ASE (b) along the boundary of a GaAs stadium with $\epsilon = 1.51$ and area $\simeq 70\mu\text{m}^2$. The range of the horizontal coordinate is half of the stadium boundary, from the center of one straight segment to the other. The solid curves are the experimental results extracted from the near-field images of the lasing mode and ASE in the insets of Fig. 4.19. The dashed curves are the numerical simulation results obtained with the FDTD method (a) and real-space ray tracing (b).

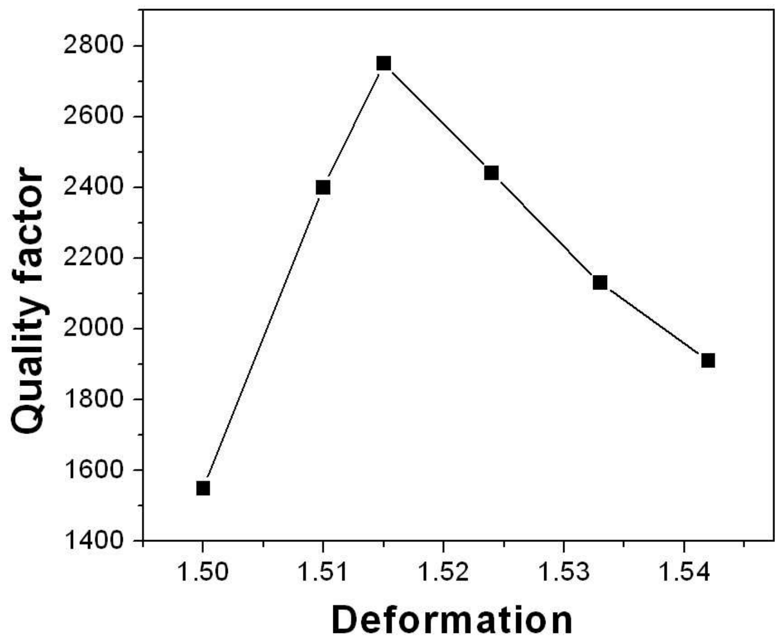

Figure 4.22: Q-factor of the mode in Fig. 4.20 (a) as a function of ϵ.

lasing threshold is minimized, as shown in Fig. 4.18.

Contrary to the low threshold microlaser at $\epsilon \sim 1.51$, the microlaser of deformation $\epsilon \sim 1.9$ experience much higher lasing threshold for the cavity resonance far away from maximum gain region. Red curve in Fig. 4.23 shows the emission spectrum when a narrow band pass filter was tuned to the lasing wavelength at 841.72nm. Inset A is the corresponding near field image which shows six bright spots on the boundary of curved ends. While the near field image of ASE emission (inset B) shows almost uniform intensity distribution along the curved ends. Our numerical simulation identified the lasing mode as shown in Fig. 4.24. The intensity distribution 100nm outside the boundary of this mode, which is convoluted with spacial resolution of image system, shows good

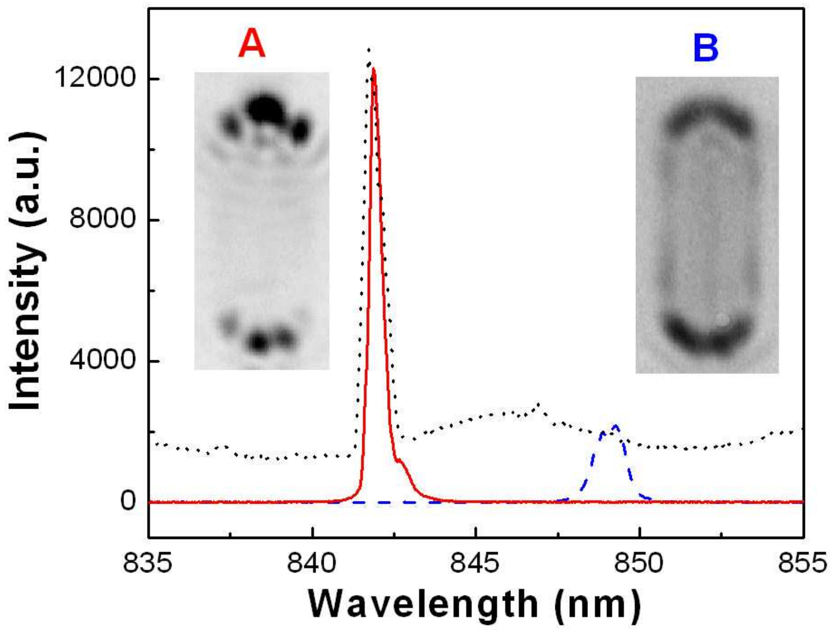

Figure 4.23: The dotted curve is the lasing spectrum from a GaAs stadium with $\epsilon = 1.9$. A bandpass filter of 1 nm bandwidth selects the first lasing mode at 841.72 nm (solid curve), and the inset A is the corresponding near-field image taken simultaneously. The dashed curve is the spectrum when the bandpass filter is tuned away from cavity resonances, the corresponding near-field image of ASE is shown in the inset B.

coincidence with the experimental result (Fig. 4.25 (a)). This confirm our conclusion. Similarly, the boundary intensity distribution of ASE image well reproduce ray-tracing result, as shown in Fig. 4.25 (b).

To study the classical ray correspondance, we investigated in the Husimi distribution of the lasing mode in Fig. 4.24 (a). It clearly indicates a scar mainly consisting two UPOs, as shown in Fig. 4.24 (b). The "fish" orbit is indicated by black squares in phase space, and double-quadrilateral orbit by blue circle. Since the constituent UPOs are above the critical line for total internal reflection, the lasing mode may has long lifetime. Yet the lasing threshold is among the highest, due to the poor gain coupling efficiency.

We simulated lasing in fabricated microstadiums with various deformations. By comparing the simulation results with the experimental data, we find the first lasing modes always correspond to high-quality scar modes of the passive cavities. This is because the gain spectrum of the InAs QW is broad enough to cover some of these modes. Note that not all the scar modes have high quality or long lifetime. Nevertheless the chaotic modes always have short lifetime, because their relatively uniform distributions in the phase space facilitate the refractive escape of light from the stadium. If the gain spectrum is too narrow to contain any high-Q scar modes, lasing may occur in low-Q chaotic modes lying within the gain spectrum [71] but with much higher threshold.

One unique property of microstadium lasers is that the Q-spoiling is effectively stopped at large deformation [80]. High-Q modes exist at large ϵ, due to nonmonotonic change of quality factors of some multi-orbit scar modes with deformation. Indeed

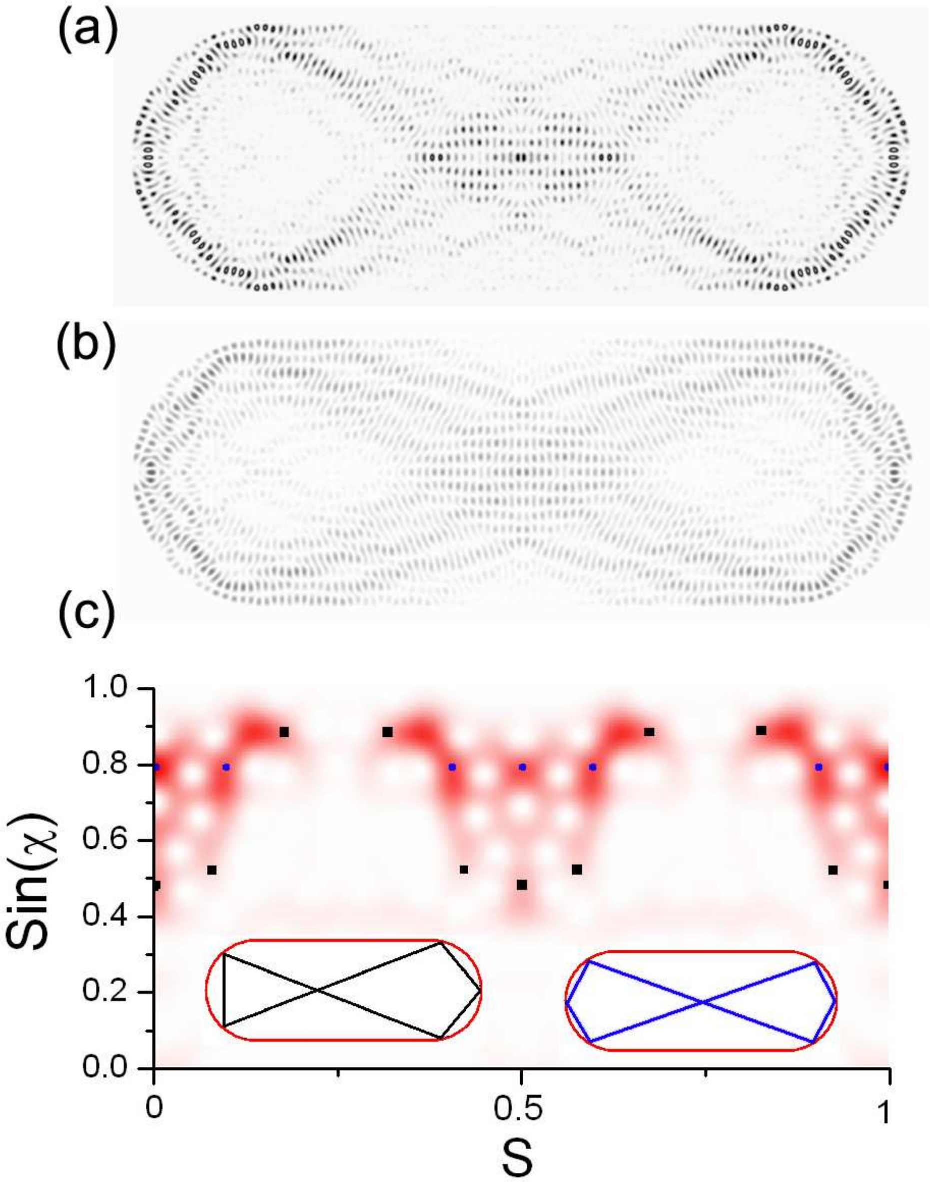

Figure 4.24: (a) Calculated intensity distribution of the first lasing mode in a stadium with $\epsilon = 1.9$, and (b) the corresponding mode in the passive stadium without gain. (c) Husimi phase space projection of the mode in (a). The squares, and dots mark the positions of two different types of UPOs shown in the inset.

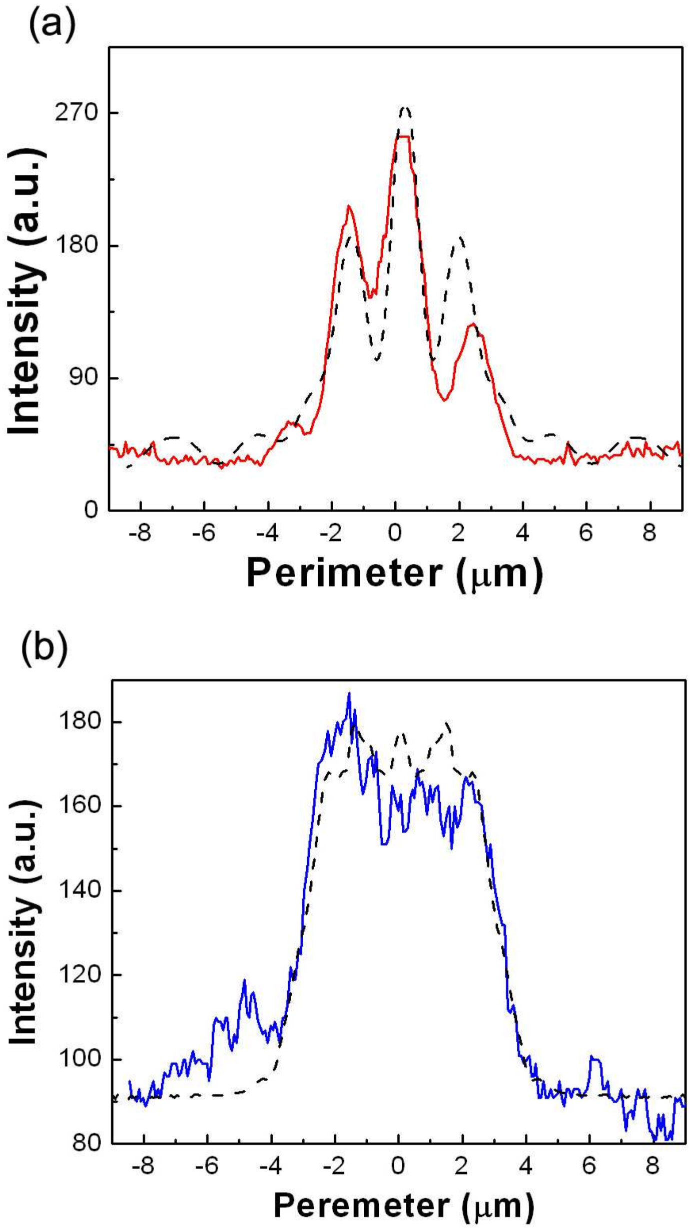

Figure 4.25: Output intensity of laser emission (a) and ASE (b) along the boundary of a GaAs stadium with $\epsilon = 1.9$. The solid curves are the experimental results extracted from the near-field images of the lasing mode and ASE in the insets of Fig. 4.23. The dashed curves are the numerical simulation results obtained with the FDTD method (a) and real-space ray tracing (b).

we observed different types of high-Q scar modes consisting of several UPOs at various deformations in our simulation. This observation is supported by our experiment result that the lasing threshold at large deformation $\epsilon = 2.2$ is nearly the same as that at small deformation $\epsilon = 0.7$. Since the lasing wavelengths in these two stadiums of same area are nearly the same, the spectral overlap of the first lasing modes with the gain spectrum is almost identical. Therefore, the almost same lasing threshold implies the quality factor of the first lasing mode in the stadium with $\epsilon = 2.2$ is nearly identical to that with $\epsilon = 0.7$. The effective stop of Q spoiling does not exist in the elliptical cavity (an integral system) or the quadrupolar cavity (a partially chaotic system) [49, 51]. Those systems exhibit continuous Q spoiling with increasing deformation when the cavity area is fixed [80]. Thus a global increase of lasing threshold is expected when the major-to-minor-axis ratio of dielectric ellipse or quadrupole increases.

In summary, we demonstrated experimentally that lasing in a semiconductor microstadium can be optimized by controlling its shape. By tuning the stadium shape to the optimum deformation, we not only optimize light confinement in the stadium but also extract the maximum gain by aligning the mode frequency to the peak of the gain spectrum. The simultaneous realization of the lowest cavity loss and the highest optical gain leads to minimum lasing threshold of a microstadium laser. As the dielectric microstadium represents a completely open fully chaotic cavity, this work opens the door to control chaotic microcavity lasers by tailoring its shape.

CHAPTER 5

APPLICATIONS

Semiconductor microdisks based on whispering gallery modes usually have very high cavity quality. And their small size and fabrication process compatible standard semiconductor technics make the microdisks one of the ideal devices for integrated optoelectronics. Blow we demonstrate the applications of microdisk: UV microdisk lasers on silicon substrate [91], and utilizing such lasers as chemical sensor [103].

5.1 Hybrid UV microdisk laser on a silicon substrate

As optoelectronics becomes increasingly important for information and communication technologies, there is a need to develop optoelectronic devices that can be integrated with standard silicon microelectronics [92]. Over the past decade, there has been much progress in developing silicon-based optoelectronic devices such as waveguides, tunable optical filters, add/drop switches, optical modulators, CMOS photodetectors, photonic crystals, and microelectromechanical systems. In addition to these passive devices, active optical devices such as lasers and light emitting diodes (LEDs) are also important components of integrated photonic circuits. Despite recent development of efficient silicon LEDs [93–95] and report of optical gain in silicon nanocrystals [96], a silicon-based laser has not yet been realized. We take a different approach in fabricating silicon-based laser: instead of extracting optical gain from silicon, we grow other gain materials on top of silicon substrates. Usually the lattice mismatch between the silicon substrate and the grown material reduces the optical quality of the gain material. However, we showed a few years ago that the zinc oxide (ZnO) thin films non-epitaxially grown on amorphous fused silica exhibit high optical gain [97]. Following this result, we made ultraviolet (UV) microdisk lasers on silicon substrates. Microdisks sustain high quality factor (Q) whispering gallery (WG) modes that are confined by total internal reflection. The high quality factor would enhance the spontaneous emission coupling efficiency and reduce the lasing threshold [99]. We fabricated the microdisks with SiO_2 instead of ZnO, because SiO_2 disks can have very high Q [62]. A very thin layer of ZnO is deposited on top of the SiO_2 disks and serves as the gain medium. As compared to the vertical cavities made of distributed Bragg reflectors, microdisks not only have higher Q, but also are much easier to fabricate. The main disadvantage of microdisk cavities is lack of directional output. However, recent studies show that deformed microdisks can provide directional output while maintaining high Q values [68, 98, 100, 101].

We fabricated the microdisks on a commercial silicon wafer which has 320 nm SiO_2 layer on the top. The wafer is spin-coated with 1.1 μm thick photoresist. Disk patterns are defined by optical lithography. The disk diameter varies from 2 μm to 20 μm. Then the pattern is transferred from the photoresist to the SiO_2 layer by reactive ion etching (RIE). The RIE etching consists of two steps. First, a gas mixture of carbon tetrafluoride (CF_4)

and hydrogen (H_2)is employed for the highly selective etching of SiO_2 over photoresist. Secondly, a short time etching with a gas mixture of CF_4 and O_2 is used to fully expose the silicon surface and facilitate the subsequent wet etching. A selective wet etching of silicon by TMAH solution is followed, and the Si pedestal is formed underneath a SiO_2 disk. Figure 5.1 is the scanning electron micrograph (SEM) of a SiO_2 microdisk on top of a Si pedestal. The disk diameter is 10 μm. We can see that the disk periphery is very smooth. The edge of SiO_2 disk is uniformly undercut by the selective wet etching. The top of the Si pedestal is shown as the dark circle in the middle of the SiO_2 disk in the top view of SEM. Its diameter is 10 μm.

After the SiO_2 microdisks are formed on the Si wafer, a thin layer of ZnO is grown on top of the disks as the gain medium. The thickness of ZnO layer is about 40 nm. The ZnO film is deposited by metalorganic chemical vapor deposition (MOCVD) in a pulsed organometallic beam epitaxy (POMBE) system. The growth apparatus has been described elsewhere [102]. Diethylzinc (DEZn) is used as the zinc precursor. It is stored in a liquid bubbler and cooled down to -26°C degree during ZnO growth. Helium gas passes through the bubbler and carries DEZn vapor to reaction chamber. Oxygen is introduced into the chamber via a separated line to prevent premature reaction. The flow rates of helium carrier gas and oxygen are both controlled by mass flow controller to 1 standard cubic centimeter per minute(SCCM) and 30 SCCM respectively. During ZnO film growth, the sample is immersed in a oxygen plasma excited by microwave energy with frequency at 2.45GHz. The sample is heated to 600°C by resistive heating

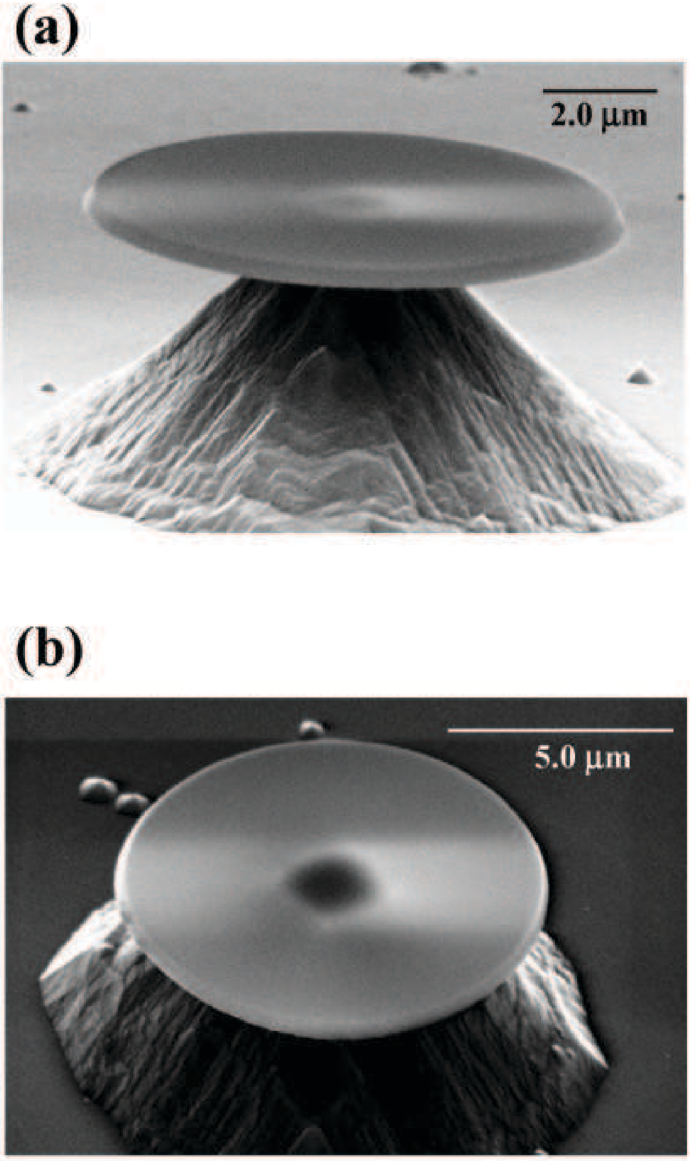

Figure 5.1: Scanning electron micrographs of a SiO_2 disk. (a) Top view, (b) side view. The disk diameter is 10 μm.

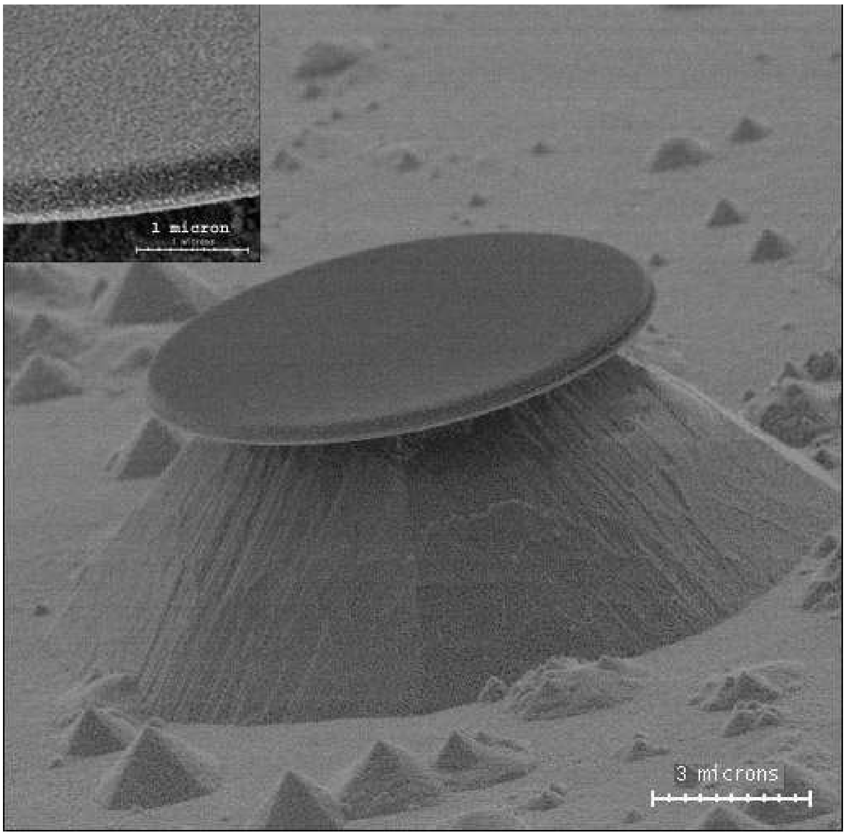

Figure 5.2: Scanning electron micrograph of a 10 μm disk after the deposition of ZnO film. The inset is a close-up view.

of sample holder. Figure 5.2 is the SEM of the microdisk structure after ZnO deposition. A close-up view in the inset shows that the disk surface is uniformly covered by the ZnO nanocrystals whose size is $\sim$ 30 nm.

The hybrid ZnO/SiO_2 microdisk is optically pumped by the third harmonics (λ = 355 nm) of a mode-locked Nd:YAG laser (10 Hz repetition rate, 20 ps pulse width). A microscope objective lens is used to focus the pump beam onto a single disk. Some emission from the WG modes is scattered into the normal direction and collected by the same objective lens. The emission spectrum is measured by a 0.5 meter spectrometer with a liquid nitrogen cooled CCD array detector. The sample is at the room temperature.

Figure 5.3 shows the spectrum of emission from a 10 μm disk. The peaks correspond to the cavity modes. Some peaks have much higher intensity and narrower width than the others. Figure 5.4 is a plot of the spectrally integrated intensity of a peak versus the pump power. We can see that the emission intensity increases dramatically above a pumping threshold, and eventually saturates. The spectral width of an emission peak is plotted as a function of pump power in Fig. 5.5. The linewidth is decreased from 0.36 nm to 0.17 nm as the pump power increases. These data clearly illustrate lasing in the hybrid microdisk cavities.

The commercial silicon wafer is not designed for microdisk structure. The oxide layer thickness is not optimized for single guided mode operation. In fact the disk layer, which consists of 320 nm SiO_2 and 40 nm ZnO, supports three transverse electric modes (TE0, TE1, TE2) and three transverse magnetic modes (TM0, TM1, TM2). For the TE modes, the electric field is parallel to the disk plane; while for the TM modes, the electric field is perpendicular to the disk plane. To identify the lasing modes, we calculate the effective index of refraction n_{eff} for the guided modes at the ZnO emission wavelength. n_{eff} = 1.63, 1.36, 1.06 for TE0, TE1, TE2 modes, and n_{eff}=1.44, 1.24, 1.01 for TM0, TM1, TM2 modes. From the effective index of refraction, we find the frequencies of WG modes in a microdisk. The radial variation of the mode field is given by the Mth order Bessel function $J_M(2\pi n_{eff} r/\lambda_m)$, where r is the radial coordinate, and m is the azimuthal number. We assume the field is zero at the disk boundary, i.e., $J_M(2\pi n_{eff} R/\lambda_m) =$

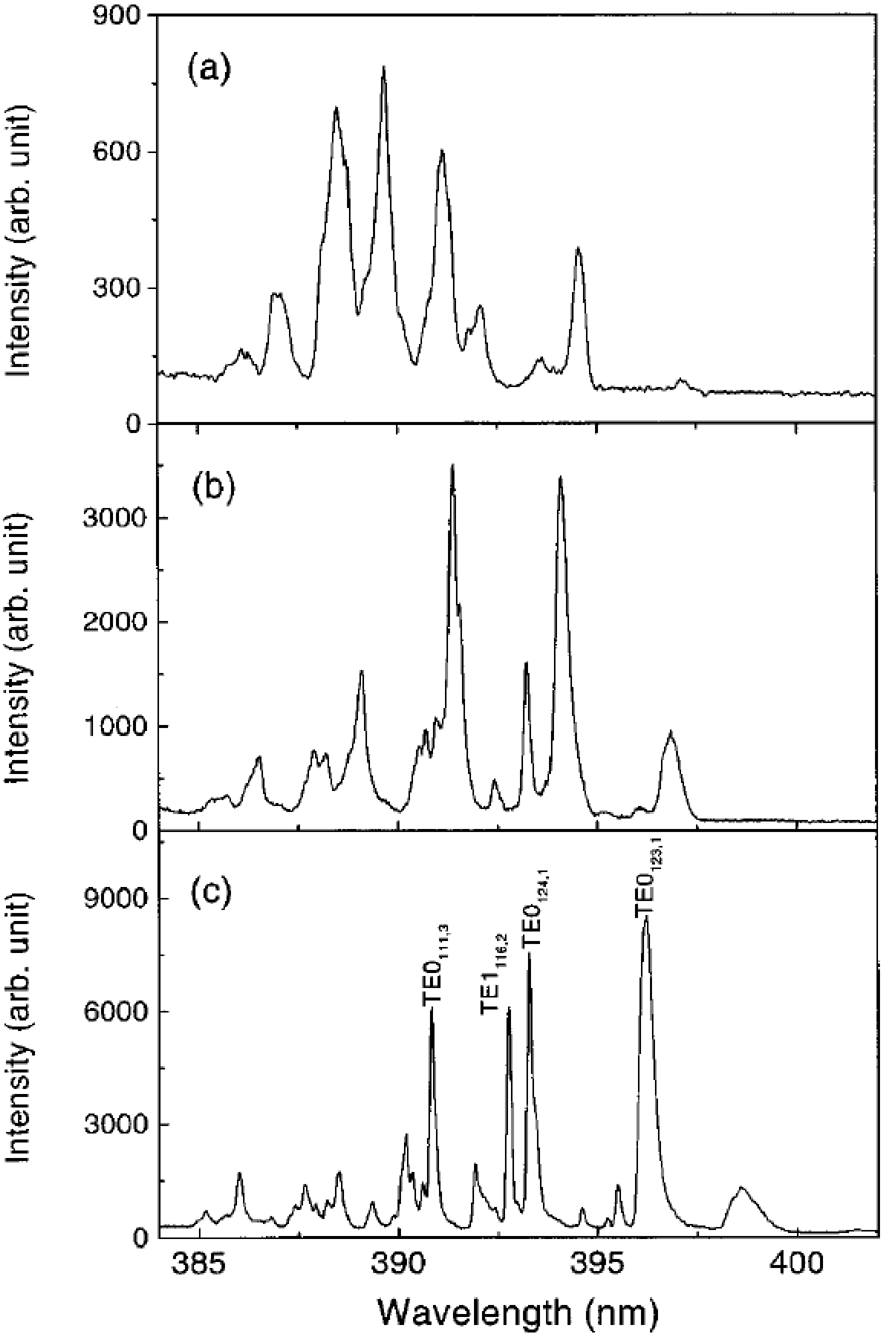

Figure 5.3: Spectrum of emission from a 10 μm disk. The incident pump pulse energy is (a)0.42 nJ, (b)0.95 nJ, and (c)1.8nJ.

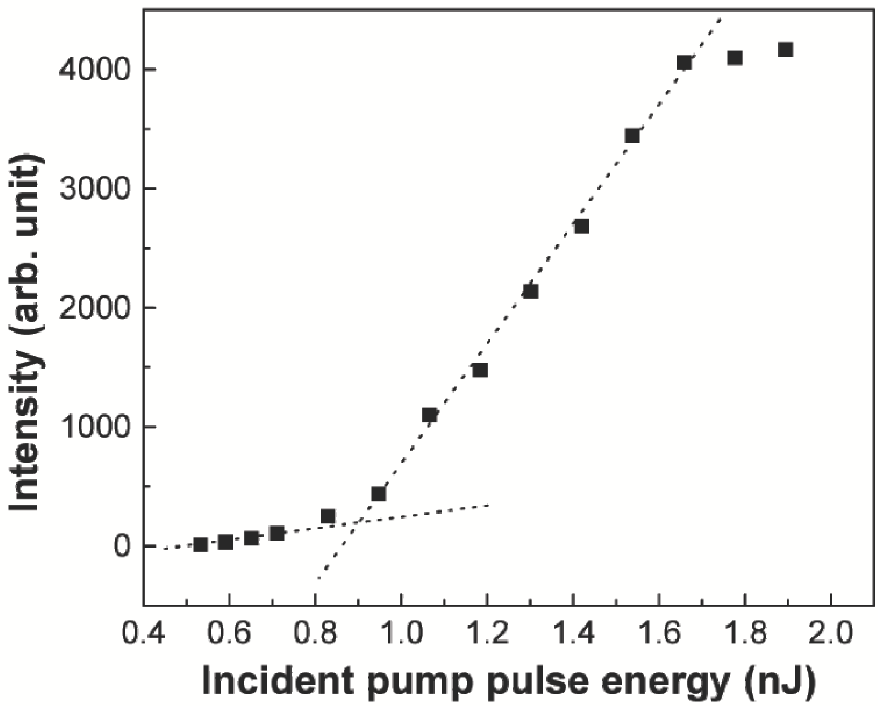

Figure 5.4: Spectrally-integrated emission intensity of a WG mode as a function of incident pump pulse energy.

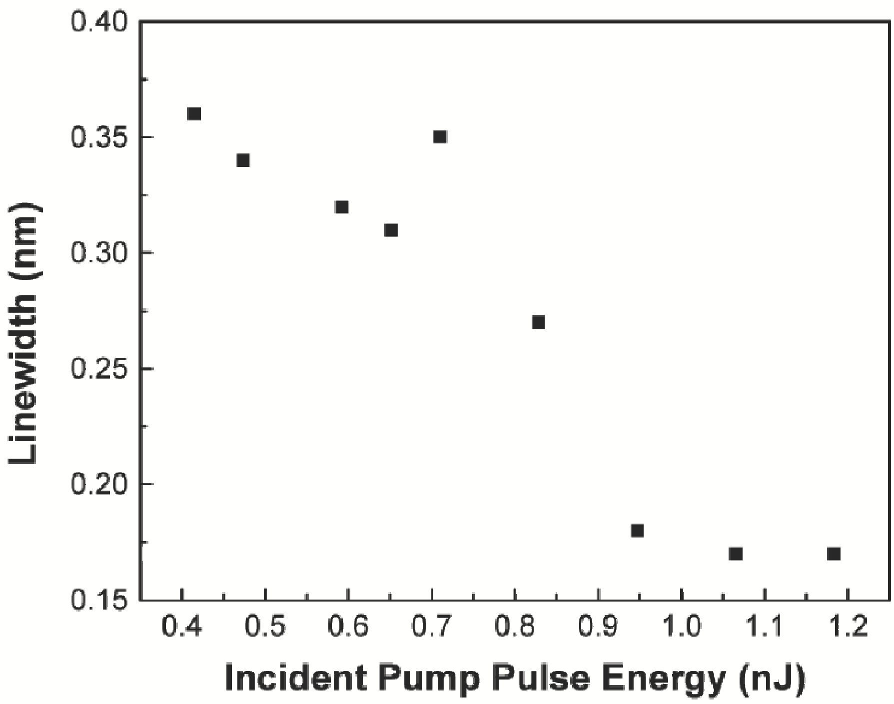

Figure 5.5: The full width at half maximum of a WG mode versus the incident pump pulse energy.

0, where R is the disk radius. By solving for the zero points of J_M , we obtain the wavelength $\lambda_{m,n}$ of the WG modes. n represents the order of the zero points for J_M, and it is called the radial number. Thus a WG mode is labeled as $\mathrm{TEX}_{m,n}$ or $\mathrm{TMX}_{m,n}$, where X is the order of the guided mode. For our disks, X can be 0, 1, or 2. In a 10 μm disk, there are many WG modes within the ZnO gain spectrum. The frequency spacing between some WG modes is so small that the modes cannot be resolved. Instead they appear to be one relatively broad peak. Although there exist six guided modes, the lasing modes are mainly the fundamental transverse electric mode TE0 (Fig. 5.3). To explain this phenomenon, we plot the spatial profiles of the six guided modes in Fig. 5.6. The TE0 mode has the largest spatial overlap with the ZnO layer (gain medium). Hence, it experiences the highest gain. We also notice the lasing modes have small radial number n. This is because the WG mode with smaller n has larger effective radius. Its wavefunction has less extension to the disk center, thus the scattering los caused by the pedestal is minimized.

Although we have realized lasing in the hybrid ZnO/SiO_2 microdisks, the pump intensity required to reach the lasing threshold is quite high. The high lasing threshold result from several factors. (i) Most incident pump light is not absorbed by the thin ZnO layer. (ii) Higher-order guided modes compete for gain. (iii) Impurities in the SiO_2 layer absorb laser emission. (iv) ZnO nanocrystals induce scattering loss. Therefore, we believe the lasing threshold can be significantly reduced by decreasing the SiO_2 layer thickness to suppress the higher-order guided modes, using pure SiO_2 to eliminate absorption, and

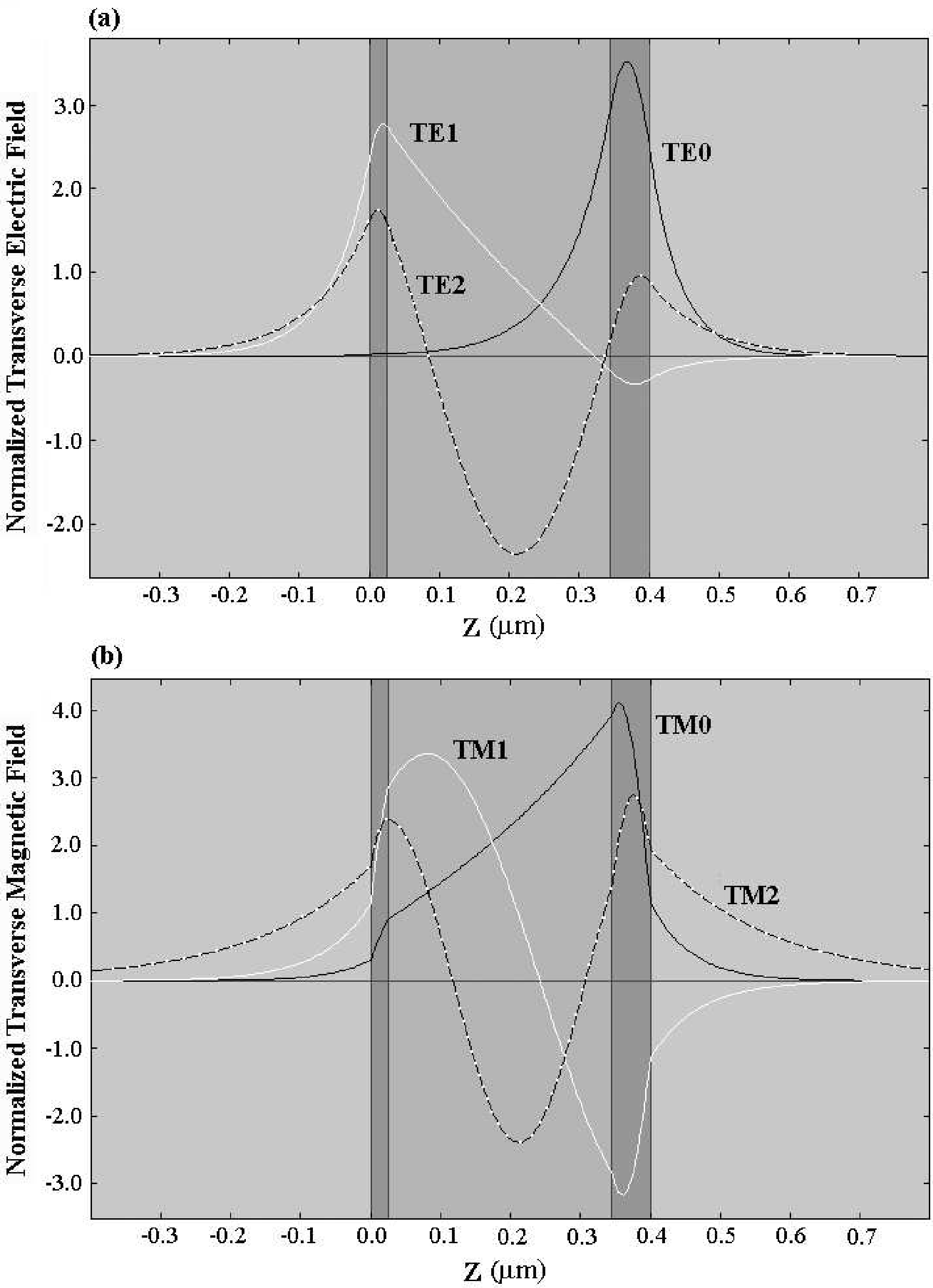

Figure 5.6: Calculated spatial profile of the waveguide modes for (a) TE0, TE1, TE2 modes, and (b) TM0, TM1, TM2 modes. The layers (with different colors) from left to right along x-axis are air, ZnO, SiO_2, ZnO, and air.

reducing the size of ZnO nanocrystals to minimize the scattering loss.

5.2 Application of microdisk lasers to chemical sensing

Over the past few years, several techniques have been developed for the construction of chemical sensors based upon photonic devices. Among them, sensors based on microdisk or microsphere resonators have demonstrated superior sensitivity due to very high quality factors of the resonances. [104–111]. This high refractive index sensitivity is essential when contemplating the detection of a single or a few molecules [107, 109]. Microdisks and microspheres sustain whispering gallery (WG) modes that are confined by total internal reflection at the boundary. The large quality factor of WG modes results in very high intracavity light intensity and extremely narrow resonant width [106]. To this point, two mechanisms have been proposed and realized for microdisk/microsphere sensor applications. The first type of microdisk/microsphere sensor relies upon the buildup of pump light intensity inside the cavity to enhance the fluorescence of molecules near the cavity surface [105, 110]. The second variety measures the spectral shift of cavity modes or decrease of transmission, due to refractive index change of the cavity or an increase of optical absorption accompanying target localization. [104, 107, 109]. Owing to the extremely narrow linewidths displayed by WG modes, tiny spectral shifts, and thus a small number of molecules can be detected [108]. However, in these demonstrations, the detection of spectral shift requires a laser source whose frequency can be continuously tuned. Moreover, the efficient evanescent coupling of light into and out of WG modes requires precise optical alignment, which is difficult to realize and maintain in a real-world sensing application. To overcome the above limitations, we utilized microdisk lasers to sense the presence of volatile organic compounds (VOCs). In particular, we detected the shift of lasing frequency when chemical molecules are adsorbed to the disk surface. As compared to passive cavities, the narrowing of WG modes by stimulated emission leads to a further improvement of sensitivity.

Recently, we fabricated ultraviolet microdisk lasers on silicon substrates as described in previous section. Silicon dioxide (SiO_2) microdisks were fabricated on a commercial silicon wafer by a combination of photolithographic, reactive ion etching and wet etching methods. Subsequently a thin layer of nanocrystalline zinc oxide (ZnO) was grown over the SiO_2 disks by metalorganic chemical vapor deposition. ZnO is a wide bandgap semiconductor, and it served as a gain medium under optical pumping. Scanning electron microscopy revealed that the SiO_2 disk surface was uniformly covered by ZnO nanoparticles with an average size of 30 nm. Lasing oscillation in the whispering gallery modes was realized at room temperature. Since adsorption of organic molecules onto metal oxide surfaces is largely due to non-specific van der Waals interactions, we chose to examine the adsorption of toluene and nitrobenzene onto the microdisk surfaces. The observed sensitivity to these two molecules demonstrated the feasibility of ZnO/SiO_2 microdisk laser-based sensing scheme.

Beginning with toluene, we introduced the volatile phase analyte into a home made sample cell permitting simultaneous optical interrogation. The cell, constructed from aluminum, had a TorrSeal adhered quartz window and two chromed luer lock ports to facilitate vapor delivery. Both of the analytes were initially prepared as saturated vapors in organic impermeable Tedlar bags (Pollution Measurement Corporation, Oak Park, IL). Subsequent vapor dilution, with N_2 gas, and delivery was performed using a Model 1010 Precision Gas Diluter (Custom Sensor Solutions, Naperville, IL). ZnO/SiO_2 microdisk lasers were optically pumped by a frequency tripled mode-locked Nd:YAG laser ($\lambda = 355$ nm 10 Hz repetition rate, 20 ps pulse width). A microscope objective lens (10×) was used to focus the pump beam onto a single disk. A portion of the emission from the WG modes was scattered in the normal direction and collected by the same objective lens. Lasing spectra were then taken by a 0.5 meter spectrometer with a liquid nitrogen cooled charge-coupled-device array detector.

Keeping the pump intensity above the lasing threshold, lasing spectra were measured upon exposure to toluene vapor. Figure 5.7 shows the spectra of laser emission from a 10 μm diameter microdisk at the incident pump pulse energy of 15 nJ. The SiO_2 layer is 320 nm thick, and the ZnO layer is $\sim$ 55 nm thick. As shown in Fig. 5.7, lasing was observed in several WG modes. As the saturated toluene vapor, in N_2, flew into the sample cell, molecules were adsorbed onto the microdisk surface. The adsorbtion led to an increase of the effective index of refraction of the disk, thus the WG modes were shifted to longer wavelengths. After equilibrium was established between the vapor phase and surface-bound toluene molecules, the lasing wavelength did not shift further. Upon flushing with pure N_2 gas, the lasing modes returned to their initial wavelengths.

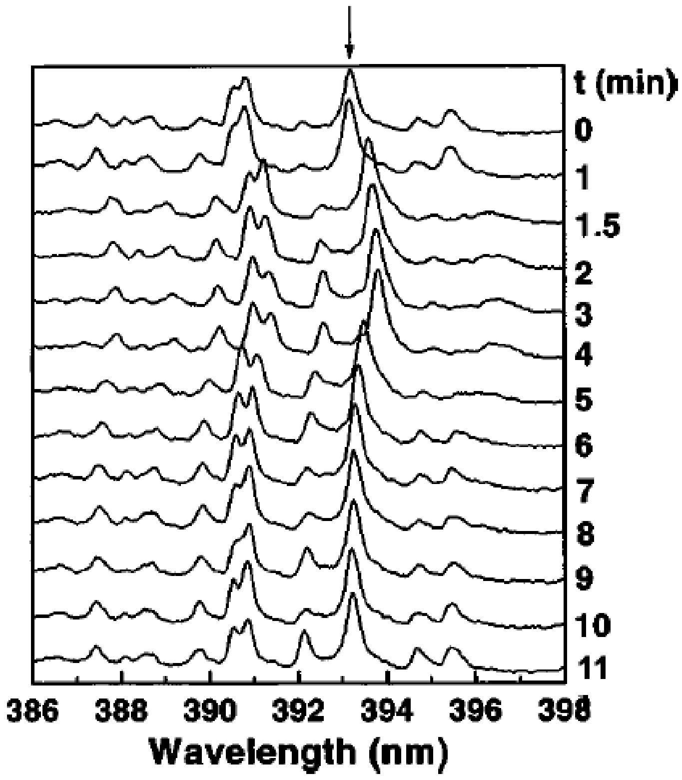

Figure 5.7: Temporal evolution of emission spectra of a microdisk laser upon exposure to saturated toluene vapor in N_2. The disk diameter is about 10 μm. The incident pump pulse energy is fixed at 15 nJ. At t = 1 min, saturated vapor is introduced into the sample cell. At t = 4 min, the vapor is switched to pure N_2. The time interval is shown in units of minutes.

To test the detection range and linearity of the sensor, we then exposed the microdisk laser to varying concentrations of toluene vapor. As the concentration was increased, in terms of percentage of saturated toluene vapor, the lasing wavelength shifts monotonically to longer wavelengths. Figure 5.8 demonstrated this by plotting the lasing wavelength shift as a function of the percentage of saturated toluene vapor exposed to the microdisk laser. Finally, we investigated the temporal response characteristics of the sensing scheme. Shown in Figure 5.9 are the responses of a microdisk laser to both 50% and 100% saturated toluene vapor in N_2. Both experiments validated the reversibility of the sensor response and showed a response time on the order of half a minute. While still very respectable, the relatively slow response is not a product of the sensing media or approach, rather an artifact caused by the vapor delivery system employed. Specifically, the dilutor pump has a relatively large mixing chamber and the Bev-A-Line IV tubing used to deliver the vapor has an small, but significant affinity for these organic molecules. The result of this is that equilibrium must be reached not only at the disk surface, but also along the entirety of the tubing length causing the artificially slow response.

Figure 5.10 shows an extension of microdisk laser sensor to the detection of nitrobenzene vapor. The experimental exposure procedure, identical to that for toluene, again results in an observed red-shift of the WG lasing modes, with a maximum shift of 0.62 nm in response to 50% saturated nitrobenzene vapor. But it takes much longer time for the spectrum back to the original position when flushed with pure N_2 gas. This is because the nitrobenzene molecules stick firm to the surface of the system. Notably, the ZnO/SiO_2

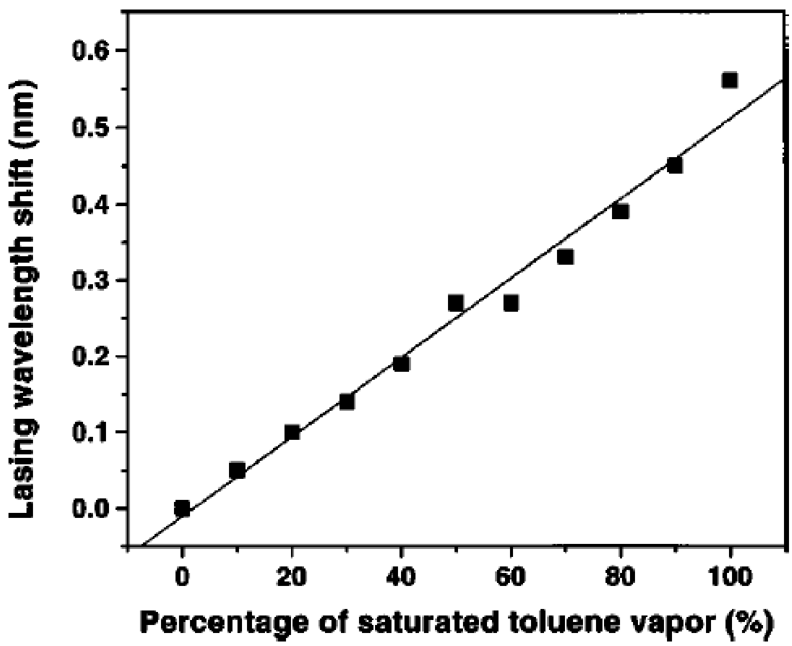

Figure 5.8: Wavelength shift of the lasing mode (marked by the arrow in Fig. 5.7) as a function of increasing percentages of saturated toluene vapor. The straight line represents a linear fit.

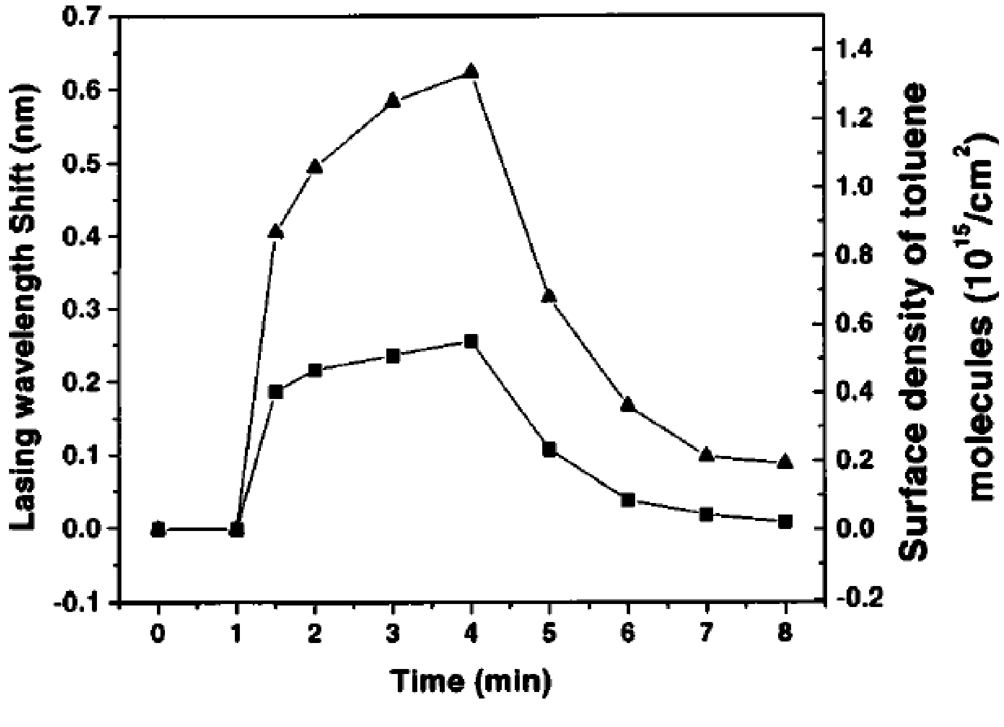

Figure 5.9: Wavelength shift of the lasing mode (marked by the arrow in Fig. 5.7) versus time. The toluene concentrations are 50% saturated vapor in N_2 (squares) and 100% (triangles). The surface density of toluene molecules, calculated from the wavelength shift, is also presented on a second y-axis.

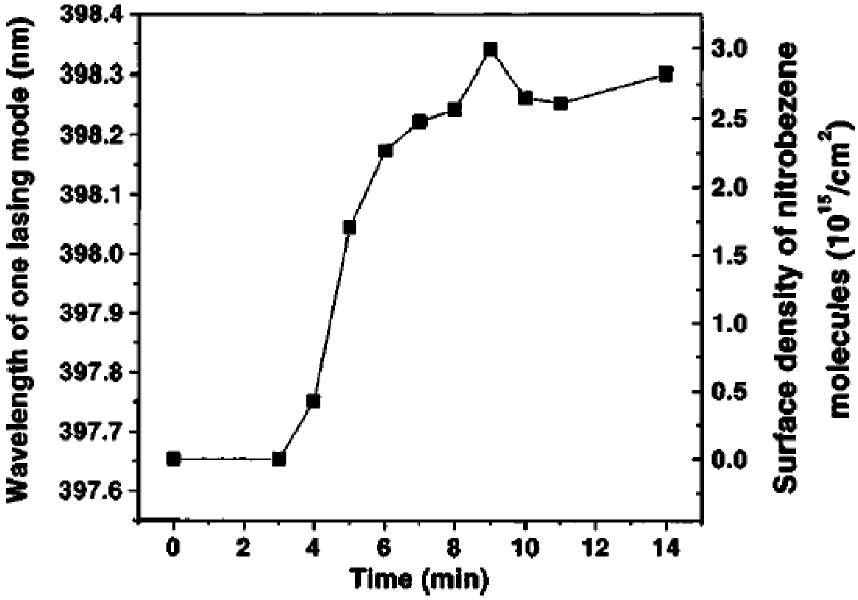

Figure 5.10: Temporal change of the wavelength of a lasing mode and the corresponding surface density of nitrobenzene molecules upon exposure to 50% saturated nitrobenzene vapor in N_2

microdisk laser appears to be much more sensitive to nitrobenzene than toluene. In fact a concentration of nitrobenzene 300 times lower than that for toluene induces an equal shift in lasing frequency. We preliminarily attribute this to redox interactions between the n-type ZnO and the nitro group of the target molecule [114].

From the shift of lasing frequency, we can infer the amount of organic molecules adsorbed to the microdisk laser. The ZnO/SiO_2 disk layer supports three transverse electric modes (TE0, TE1, TE2) and three transverse magnetic modes (TM0, TM1, TM2). For the TE modes, the electric field is parallel to the disk plane; while for the TM modes, the electric field is perpendicular to the disk plane. From the guided mode profile normal to the disk plane, we calculate the effective index of refraction n_{eff} for the guided modes at the ZnO emission frequency. In the absence of any organic molecules, n_{eff} = 1.68, 1.38, 1.09 for TE0, TE1, TE2 modes, and n_{eff}=1.47, 1.28, 1.02 for TM0, TM1, TM2 modes. From the effective index of refraction, we can calculate the frequencies of WG modes in the microdisk. The radial variation of the electric field for a WG mode is given by the mth order Bessel function $J_m(2\pi n_{eff}\, r/\lambda)$, where r is the radial coordinate, and m is the azimuthal number. The boundary condition can be approximated by assuming that the field goes to zero at the disk edge: $J_m(2\pi n_{eff} R/\lambda) = 0$, where R is the disk radius. By solving for the zero points of J_m , we obtain the wavelength $\lambda_{m,n}$ of the WG modes. n represents the order of the zero points of J_m, and it is called the radial number. Thus a WG mode is labeled as TE$X_{m,n}$ or TM$X_{m,n}$, where X is the order of the guided mode. For our disks, X can be 0, 1, or 2. In a 10 μm disk, there are many WG modes within the ZnO gain spectrum. The frequency spacing between some WG modes is so small that the modes cannot be resolved. Instead they appear to be one relatively broad peak. Although there are six guided modes, the observed lasing modes arise mostly from the fundamental transverse electric mode TE0, because it has the largest spatial overlap with the ZnO layer (gain medium).

In the cylindrical coordinates, the electric field distribution of the TE$X_{m,n}$ mode can be expressed as:

$$\mathbf{E}(r, \theta, z) = J_m(frac2\pi n_{eff} r\lambda)\, e^{im\theta}\, f_X(z)\, \mathbf{e}_r\, , \tag{5.1}$$

where $\mathbf{e}_r$ is the unit vector along the radial (r) direction and $f_X(z)$ represents the TE mode profile in the vertical (z) direction. When organic molecules are absorbed onto the disk surface, they are polarized by the cavity electric field. The induced dipole moment of a single molecule is represented by $\mathbf{p}_m = \alpha\,\mathbf{E}$, where α is the molecular polarizability. The induced dipole causes a shift of the cavity photon energy $h\,\delta\nu = -\mathbf{p}_m \cdot \mathbf{E}/2 = -\alpha\,|E|^2/2$, according to Refs. [112, 113]. When many molecules are adsorbed randomly but uniformly onto the disk surface, we sum over their contributions to the frequency shift: $h\,\delta\nu = -(1/2)\alpha\,\sigma \int |E(r,\theta,z=d)|^2 r\,dr\,d\theta$, where σ is the surface density of molecules. Thus, the fractional frequency shift is

$$\frac{\delta\nu}{\nu} = \frac{-\alpha\,\sigma \int |E(r,\theta,z=d)|^2\,r\,dr\,d\theta}{2\int \epsilon_s(z)|E(r,\theta,z)|^2\,r\,dr\,d\theta\,dz} = \frac{-\alpha\sigma|f_X(d)|^2}{2\int \epsilon_s(z)|f_X(z)|^2 dz}\,, \tag{5.2}$$

where $\epsilon_s(z)$ represents the material permittivity along the z direction. Using Eq.(2), we calculated the surface density of adsorbed molecules from the frequency shift of the WG modes, plotted in Figs. 5.9 and 5.10 for toluene and nitrobenzene, respectively.

In conclusion, we have demonstrated that ZnO/SiO_2 microdisk lasers can be used as chemical sensors. When molecules from the vapor phase are adsorbed onto the disk surface, the lasing modes are red-shifted due to an increase in the effective refractive index of the microdisk. From the shift, we calculate the spatial density of molecules on the microdisk. The drastically different sensitivity of the ZnO/SiO_2 microdisk laser to toluene and nitrobenzene demonstrates the potential of chemically selective sensing by utilizing differential adsorption or implementing an additional partition layer. Compared to the passive microdisk/microsphere sensors, it is advantageous that the microdisk laser-based sensors do not require tunable laser source, rather the pump laser frequency can remain fixed and detuned from any cavity resonance. Moreover, electrically-pumped microdisk lasers have already been demonstrated [115], and their application to this sensor motif will further empower our approach by eliminating the need for optical pumping all together.

CHAPTER 6

CONCLUSIONS AND FUTURE PROSPECTS

Circular structures have very high symmetry. The optical modes in a dielectric microdisk are whispering gallery modes with regular patterns and high quality factors. Introducing deformation on the boundary will destroy the symmetry, and may even drive the classical ray dynamics into chaos. As a result, the quality factors of high-Q optical modes also get spoiled. This work presented here covers the studies of physics in semiconductor microdisks and deformed microdisk lasers, namely spontaneous emission rates of quantum dots embedded in microdisks, dynamical localization of a lasing mode in microdisk with rough boundary, and high-Q modes in microstadium lasers.

We have fabricated InAs quantum dots microdisks, and studied the spontaneous emission rates for the embedded quantum dots in the time-resolved photoluminescence experiment. A quantum dot ideally coupled with high-Q whispering gallery mode has very large enhancement of its spontaneous emission rate, characterized by Purcell factor. Yet inhomogeneous broadening of the quantum dot energy levels and random spatial distribution of the quantum dots in a microdisk lead to a broad distribution of the spontaneous emission rates. Using a non-negative least norm algorithm, we extracted the distribution of spontaneous emission rates from the temporal decay of emission intensity. The maximum spontaneous emission enhancement factor exceeded 10.

We have studied the lasing action from a dynamically localized mode in a microdisk resonator with rough boundary. Although substantial boundary roughness and surface defects in our devices imply strong light scattering and destroy the regular whispering gallery modes, the destructive interference of the scattered light leads to the dynamical Anderson localization in the angular momentum phase space of the system. While most of the angular momentum components are above critical value corresponding to critical angle, it forms a high-Q mode different from regular whispering gallery mode. Using direct optical imaging of the lasing mode and theoretical calculations, we showed that the lasing modes in our devices had dynamical localization origin.

We have presented a numerical study of the high-quality modes in two-dimensional dielectric stadium microcavities. Although the classical ray mechanics is fully chaotic in a stadium billiard, all of the high-quality modes show strong "scar" around unstable periodic orbits. When the deformation (ratio of the length of the straight segments over the diameter of the half circles) is small, the high-quality modes correspond to whispering-gallery-type trajectories, and their quality factors decrease monotonically with increasing deformation. At large deformation, each high-quality mode is associated with multiple unstable periodic orbits. Its quality factor changes non-monotonically with the deformation, and there exists an optimal deformation for each mode at which its quality factor reaches a local maximum. This unusual behavior is attributed to the interference of waves propagating along different constituent orbits that could minimize light leakage out of the cavity. We also demonstrated experimentally that lasing in a semiconductor microstadium can be optimized by controlling its shape. Under spatially uniform optical pumping, the first lasing mode in a GaAs microstadium with large major-to-minor-axis ratio usually corresponds to a high-quality scar mode consisting of several unstable periodic orbits. Interference of waves propagating along the constituent orbits may minimize light leakage at particular major-to-minor-axis ratio. By making stadium of the optimum shape, we were able to maximize the mode quality factor and align the mode frequency to the peak of the gain spectrum, thus minimizing the lasing threshold.

In the application aspect, we have fabricated ultraviolet microdisk lasers on a silicon substrate. A thin layer of zinc oxide was grown on top of the silica microdisks and serves as the gain medium. Under optical pumping, lasing occurred in the whispering gallery modes of the hybrid microdisks at room temperature. Above the lasing threshold, a drastic increase of emission intensity was accompanied by a decrease of the spectral width of the lasing modes. We have also utilized such hybrid microdisk lasers to sense volatile organic compounds, such as toluene and nitrobenzene. Nonspecific adsorption of these organic molecules onto the microdisk surface causes an increase in the disk refractive index, ultimately resulting in a red-shift of the observed lasing wavelengths. The monitoring of these shifts provides the sensing modality. Microdisk lasers were found to respond rapidly and reversibly to the investigated chemicals demonstrating, in principal, the chemical and biological sensing capabilities of such devices.

Finally, we would like to point out some interesting research works that could be done in the future:

Approaching to single quantum dot emitter Single quantum dot coupled to whispering gallery mode in a microdisk provides a way for high efficiency single photon source, which already shows broad application futures such as secure quantum cryptography and linear optical quantum computing [116]. One of the major problem is still the spacial and spectral overlapping of the QD with WGM. We find out some way to control the position of quantum dots during the growth [117], which is the first step to approach the final goal. And the spectral overlapping may be possibly controlled by tuning some experimental conditions such as temperature.

Directional output from semiconductor microstadium lasers Achieving directional output is one of the goal to study deformed cavities. Lasing output from polymer microstadiums has been studies [72,73], which shows the output mainly follows the unstable manifold of classical ray dynamics. Semiconductor microstadium, on the other hand, has much larger index of refractivity. Light may experience longer path before finally escapes from the cavity. Thus wave effects, such as interference may show up and possibly give different far-field pattern from classical prediction.

We hope our work can provide some guidance for future studies on optical microcavities and quantum chaos.

REFERENCES

[1] K. Iga, *IEEE J. of Selected Topics in Quan. Elec.* **6**, 1201 (2000)

[2] S. Noda, M. Yokoyama, M. Imada, A. Chutina, and M. Mochizuki, *Science* **293**, 5532 (2001)

[3] S. L. McCall, A. F. J. Levi, R. E. Slusher, S. J. Pearton, and R. A. Logan, *Appl. Phys. Lett.* **60**, 289 (1992).

[4] M. K. Chin, D. Y. chu, and S. T. Ho, *J. Appl. Phys.* **75**, 3302 (1994)

[5] W. S. Rayleigh, *Scientific Papers* **5**, 617 (1912)

[6] P. Maksym and T. Chakraborty, *Phys. Rev. Lett.* **65**, 108 (1990)

[7] *Springer Tracts in Modern Physics*, Volumne 219. (Springer Berlin/Heidelberg, 2006)

[8] K. Kash, *J. Lumin.* **46**, 69 (1990)

[9] J. Y. Marzin, J. M. Gérard, A. Izraël, D. Barrier, and G. Bastard, *Phys. Rev. Lett.* **73**, 716 (1994)

[10] M. V. Berry, *Eur. J. Phys.* **2**, 91 (1981)

[11] L. A. Bunimovich, *Commun. Math. Phys.* **130**, 599 (1990)

[12] Ofer Biham and Mark Kvale, *Phys. Rev. A* **46**, 6334 (1992)

[13] Bruno Eckhardt and Dieter Wintgen, *J. Phys. A: Math. Gen.* **24**, 4335 (1991)

[14] Edward Ott, *Chaos in dynamical systems*, 2nd ed. (Cambridge University Press, Cambridge, 2002)

[15] Bruno Crespi, Gabriel Perez, and Shau-Jin Chang, *Phys. Rev. E* **47**, 986 (1993)

[16] M. Hentschel, H. Schomerus, and R. Schubert, *Europhys. Lett.* **62**, 636 (2003)

[17] K. S. Yee, *IEEE Trans. Antennas and Propagation* **14**, 302 (1966)

[18] J. P. Berenger, *J. Computational Phys.* **114**, 185 (1994)

[19] A.S. Nagra and R.A. York, IEEE Trans. Antennas Propagat. **46**, 334 (1998).

[20] E. Burstein and C. Weisbuch, Confined Electrons and Photons: New Physics and Applications, NATO ASI Series (Plenum, New York, 1995), vol. B340.

[21] J. G. Rarity and C. Weisbuch, Microcavities and Photonic Bandgaps: Physics and Applications, NATO ASI Series (Kluwer, Dordrecht, 1996), vol. E324.

[22] E. M. Purcell, *Phys. Rev.* **69**, 681 (1946).

[23] P. Goy, J. M. Raimond, M. Gross, and S. Haroche, *Phys. Rev. Lett.* **50**, 1903 (1983).

[24] G. Gabrielse, and H. Dehmelt, *Phys. Rev. Lett.* **55**, 67 (1985).

[25] R. G. Hulet, E. S. Hilfer, and D. Kleppner, *Phys. Rev. Lett.* **55**, 2137 (1985).

[26] D. J. Heinzen, J. J. Childs, J. E. Thomas, and M. S. Feld, *Phys. Rev. Lett.* **58**, 1320 (1987).

[27] J. M. Gerard, B. Sermage, B. Gayral, B. Legrand, E. Costard, and V. Thierry-Mieg, *Phys. Rev. Lett.* **81**, 1110 (1998).

[28] L. A. Graham, D. L. Huffaker, Q. Deng, and D. G. Deppe, *Phys. Lett.* **72**, 1670 (1998).

[29] L. A. Graham, D. L. Huffaker, and D. G. Deppe, *Appl. Phys. Lett.* **74**, 2408 (1999).

[30] C. Santori, M. Pelton, G. S. Solomon, Y. Dale, and Y. Yamamoto, *Phys. Rev. Lett.* **86**, 1502 (2001).

[31] M. Bayer, T. L. Reinecke, F. Weidner, A. Larionov, A. McDonald, and A. Forcel, *Phys. Rev. Lett.* **86**, 3168 (2001).

[32] G. S. Solomon, M. Pelton, and Y. Yamamoto, *Phys. Rev. Lett.* **86**, 3903 (2001).

[33] C. Becher, A. Kiraz, P. Michler, A. Imamoglu, W. V. Schoenfeld, P. M. Petroff, L. Zhang, and E. Hu, *Phys. Rev. B* **63**, R121312 (2001).

[34] P. Michler, A. Kiraz, C. Becher, W. V. Schoenfeld, P. M. Petroff, L. Zhang, E. Hu, and A. Imamoglu, *Science* **290**, 2282 (2000).

[35] B. Gayral, J. M. Gerard, B. Bsermage, A. Lemaitre, and C. Dupuis, *Appl. Phys. Lett* **78**, 2828 (2001).

[36] A. Kiraz, P. Michler, C. Becher, G. Gayral, A. Imamoglu, L. Zhang, E. Hu, W. V. Schoenfeld, and P. M. Petroll, *Appl. Phys. Lett* **78**, 3932 (2001).

[37] W. Fang, J. Y. Xu, A. Yamilov, and H. Cao, *Opt. Lett.* **27**, 948 (2002)

[38] B. Gayral, J. M. Gerard, A. Lemaitre, C. Dupuis, L. Manin, and J. L. Pelouard, *Appl. Phys. Lett.* **75**, 1908 (1999).

[39] H. Cao, J. Y. Xu, W. H. Xiang, Y. Ma, S.-H. Chang, S. T. Ho, and G. S. Solomon, *Appl. Phys. Lett.* **76**, 3519 (2000).

[40] J. M. Gerard, and B. Gayral, *J. Light. Tech.* **17**, 2089 (1999).

[41] D. M. Gakamsky, A. A. Goldin, E. P. Petrov, and A. N. Rubinov, *Biophys. Chem.* **44**, 47 (1992).

[42] A. A. Goldin, *Opt. Spektrosk.* (USSR) **71**, 485 (1991)

[43] E. P. Petrov, V. N. Bogomolov, I. I. Kalosha, and S. V. Gaponenko, *Acta. Phys. Pol. A* **94**, 761 (1998)

[44] S.X. Qian, J. Snow, H.M. Tzeng & R.K. Chang, *Science* **231**, 486 (1986).

[45] K. Djordjev, S.Choi, S.Choi, and P.Dapkus, *IEEE Photonics Tech. Lett* **14**, 331 (2002).

[46] B. Corbett, J. Justice, L. Considint, S. Walsh, W.M. Kelly, *IEEE Photonics Tech. Lett* **8**, 855 (1996).

[47] T. Kipp, L. Rolf, C. Schuller, D. Endler, Ch. Heyn, and D. Heitmann, *Phys. Rev. B* **63**, 195304 (2001).

[48] J. U. Nöckel, A. D. Stone, G. Chen, H. Grossman and R. K. Chang, *Opt. Lett.* **21**, 1609 (1996).

[49] E. E. Narimanov, G. Hackenbroich, P. Jacquod, and A. D. Stone, "Semiclassical theory of the emission properties of wave-chaotic resonant cavities," *Phys. Rev. Lett.* **83**, 4991 (1999).

[50] It can be shown that in $2D$ the small wavelength approximation to the solutions of Maxwell equations is essentially equivalent to the standard semiclassical limit of Shrödinger Equation.

[51] J. U. Nöckel, A. D. Stone, *Nature* **385**, 45 (1997)

[52] K.M. Frahm and D.L. Shepelyansky, *Phys. Rev. Lett* **78**, 1440 (1997).

[53] M. Berry, *J. Phys. A* **10**, 2083 (1977).

[54] M. Gutzwiller, *Chaos in Classical and Quantum Mechanics* (Springer-Verlag, New York, 1990).

[55] G. Casati, B. V. Chirikov, J. Ford, and F. M. Izrailev, in *Stochastic Behavior in Classical and Quantum Hamiltonian Systems*, Lecture Notes in Physics Vol. **93** (Springer, Berlin, 1979), p. 334.

[56] S. Fishman, D. R. Grempel, and R. E. Prange, *Phys. Rev. Lett* **49**, 509 (1982).

[57] J. Ringor, P. Szriftgiser, J. C. Carreau, D. Delande, *Phys. Rev. Lett* **85**, 2741 (2000).

[58] V.A. Podolskiy, E.E. Narimanov, W. Fang, and H. Cao, *Proceedings of Nat. Acad. of Sci.* **101**, 10498 (2004).

[59] w. Fang, H. Cao, V. A. Podolskiy, and E. E. Narimanov, *Optcs Express* **13**, 5641 (2005).

[60] L. Sirko, Sz. Bauch, Y. Hlushchuk, P.M. Koch, R. Blümel, M. Barth, U. Kuhl, and H.-J. Stöckmann, *Phys. Lett. A* **266**, 331 (2000).

[61] O.A. Starykh, P.R.J. Jacquod, E.E. Narimanov, and A.D. Stone, *Phys. Rev. E* **62**, 2078 (2000).

[62] D. K. Armani, T. J. Kippenberg, S. M. Spillane, and K. J. Vahala, *Nature* **421**, 925 (2003).

[63] G. Casati, I.Guarneri, and D. Shepelyansky, *Phys. Rev. A* **36**, 3501 (1987).

[64] F. Haake *Quantum Signatures of Chaos* Springer NY (2000).

[65] E. Doron, U. Smilansky, *Phys. Rev. Lett.* **68**, 1255 (1992).

[66] H.E. Tureci, H.G.L. Schwefel, P. Jacquod, A.D. Stone, ArXiv: physics/0308016 (2003)

[67] S.C. Chang, J.U. Nockel, R.K. Chang, and A.D. Stone, *J. Opt. Soc. Am. B* **17**, 1828 (2000).

[68] C. Gmachl, F. Capasso, E.E. Narimanov, J.U. Nockel, A.D. Stone, J. Faist, D.L. Sivco, and A.Y. Cho, *Science* **280**, 1556 (1998).

[69] E.J. Heller, *Phys. Rev. Lett.* **53**, 1515 (1984).

[70] T. Harayama, T. Fukushima, P. Davis, P.O. Vaccaro, T. Miyasaka, T. Nishimura, and T. Aida, *Phys. Rev. E* **67**, 015207(R) (2003).

[71] T. Harayama, P. Davis, and K.S. Ikeda, *Phys. Rev. Lett.* **90**, 063901 (2003).

[72] H.G.L. Schwefel *et al.*, *J. Opt. Soc. Am. B* **21**, 923 (2004).

[73] M. Lebental *et al.*, *Appl. Phys. Lett* **88**, 031108 (2006).

[74] S.W. McDonald and A.N. Kaufman, *Phys. Rev. A* **37**, 3067 (1988).

[75] S. Tomsovic and E.J. Heller, *Phys. Rev. Lett.* **67**, 664 (1991).

[76] J. Stein and H.-J. Stockmann, *Phys. Rev. Lett.* **68**, 2867 (1992).

[77] F. Borgonovi, G. Casati, and B. Li, *Phys. Rev. Lett.* **77**, 4744 (1996).

[78] G. Casati and T. Prosen, *Phys. Rev. E* **59**, R2516 (1999).

[79] R.G. Nazmitdinov, K.N. Pichugin, I. Rotter, and P. Seba, *Phys. Rev. B* **66**, 085322 (2002).

[80] W. Fang, A. Yamilov, and H. Cao, *Phys. Rev. A* **72**, 023815 (2005).

[81] W. Fang, G. S. Solomon, and H. Cao, ArXiv: physics/0607233 (2006)

[82] A. Taflove, and S. C. Hagness, *Computational Electrodynamics: The Finite-Difference Time-Domain Method*, 2nd ed. (Artech House Publishers, Boston, 2000)

[83] S.-Y. Lee, M.S. Kurdoglyan, S. Rim, and C.-M. Kim, *Phys. Rev. A* **70**, 023809 (2004).

[84] T. Fukushima, *J. Lightwave Technol.* **18**, 2208 (2000).

[85] T. Fukushima, T. Harayama, P. Davis, P.O. Vaccaro, T. Nishimura, and T. Aida, *Opt. Lett.* **28**, 408 (2003).

[86] E.G. Vergini and G.G. Carlo, *J. Phys. A: Math Gen.* **33**, 4717 (2000).

[87] H.E. Tureci, H.G.L. Schwefel, and A.D. Stone, *Opt. Express* **10**, 752 (2002).

[88] E.G. Vergini and G.G. Carlo, *J. Phys. A: Math Gen.* **34**, 4525 (2001).

[89] G.G. Carlo, E.G. Vergini, and P. Lustemberg, *J. Phys. A: Math Gen.* **35**, 7965 (2002).

[90] T. Fukushima, *J. Lightwave Technol.* **18**, 2208 (2000); T. Fukushima, T. Harayama, and J. Wiersig, *Phys. Rev. A* **73**, 023816 (2006); T. Fukushima, *IEEE J. Selet. Topic Quantum Electron.* **10**, 1039 (2004).

[91] X. Liu, W. Fang, Y. Huang, S. T. Ho, H. Cao, and R. P. H. Chang, *Appl. Phys. Lett.* **84**, 2488 (2004).

[92] A. Himeno, K. Kato, and T. Miya, *IEEE J. Sel. Top. Quantum Electron.* **4**, 913 (1998).

[93] K. D. Kirschman, L. Tsybeskov, S. P. Duttagupta, and P. M. Fauchet, *Nature* **384**, 338 (1996).

[94] W. L. Ng, M. A. Loureno, R. M. Gwilliam, S. Ledain, G. Shao, and K. P. Homewood, *Nature* **410**, 192 (2001).

[95] M. A. Green, J. Zhao, A. Wang, P. J. Reece, and M. Gal, *Nature* **412**, 805 (2001).

[96] L. Pavesi, L. Dal Negro, C. Mazzoleni, G. Franz, and F. Priolo, *Nature* **408**, 440 (2000).

[97] H. Cao, Y. G. Zhao, H. C. Ong, S. T. Ho, J. Y. Dai, J. Y. Wu, and R. P. H. Chang, *Appl. Phys. Lett.* **73**, 3656 (1998).

[98] S.-B. Lee, J.-H. Lee, J.-S. Chang, H.-J. Moon, S. W. Kim, and K. An, *Phys. Rev. Lett.* **88**, 033903 (2002).

[99] T. Baba, *IEEE J. Sel. Top. Quantum Electron.* **3**, 808 (1997).

[100] S. Lacey and H. Wang, *Opt. Lett.* **26**, 1943 (2001).

[101] N. B. Rex, H. E. Tureci, H. G. L. Schwefel, R. K. Chang, and A. D. Stone, *Phys. Rev. Lett.* **88**, 094102 (2002).

[102] S. J. Duray, D. B. Buchholz, S. N. Song, D. S. Richeson, J. B. Ketterson, T. J. Marks, and R. P. H. Chang, *Appl. Phys. Lett.* **59**, 1503 (1991).

[103] W. Fang, D. B. Buchholz, R. C. Bailey, J. T. Hupp, R. P. H. Chang, and H. Cao, *Appl. Phys. Lett.* **85**, 3666 (2004)

[104] A. T. Rosenberger and J. P. Rezac, *Proc. SPIE: Laser Resonators III* **3930**, 186 (2000).

[105] S. Blair and Y. Chen, *Appl. Opt.* **40**, 570 (2001).

[106] V. S. Ilchenko and L. Maleki, *Proc. SPIE: Laser Resonators IV* **4270**, 120 (2001).

[107] R. W. Boyd and J. E. Heebner, *Appl. Opt.* **40**, 5742 (2001).

[108] E. Krioukov, D. J. W. Klunder, A. Driessen, J. Greve, and C. Otto, *Opt. Lett.* **27**, 512 (2002).

[109] F. Vollmer, D. Braun, A. Lichaber, M. Khoshsima, I. Teraoka, and S. Arnold, *Appl. Phys. Lett.* **80**, 4057 (2002).

[110] E. Krioukov, D. J. W. Klunder, A. Driessen, J. Greve, and C. Otto, *Opt. Lett.* **27**, 1504 (2002).

[111] C.-Y. Chao and L. J. Guo, *Appl. Phys. Lett.* **83**, 1527 (2002).

[112] S. Arnold, M. Khoshsima, I. Teraoka, S. Holler, and F. Vollmer, *Opt. Lett.* **28**, 272 (2003).

[113] I. Teraoka, S. Arnold, and F. Vollmer, *J. Opt. Soc. Am. B* **20**, 1937 (2003).

[114] D. Zhang, C. Li, X. Liu, S. Han, T. Tang, and C. Zhou, *Appl. Phys. Lett.* **83**, 1845 (2003).

[115] A. F. J. Levi, R. E. Slusher, S. L. McCall, T. Tanbun-Ek, D. L. Coblentz, and S. J. Pearton, *Electron. Lett.* **28**, 1010 (1992).

[116] P. Grangier, B. Sanders, and J. Vuckovic , *New J. Phys.* **6**, (2004)

[117] Z. Xie, W. Fang, H. Cao, and G. S. Solomon, *J. Crystal Growth* **278**, 342 (2005)